UNIVERSITY OF OTTAWA

Characterization and Performance Analysis of High Efficiency Solar Cells and Concentrating Photovoltaic Systems

Thesis submitted to the Faculty of Graduate and Postdoctoral Studies in partial fulfilment of the requirements for a Master's of Applied Science in Electrical and Computer Engineering.

September 2012

School of Electrical Engineering and Computer Science
University of Ottawa

The larger the island of knowledge, the longer the shoreline of wonder.

Ralph W. Sockman

ABSTRACT

As part of the SUNRISE project (Semiconductors Using Nanostructures for Record Increases in Solar-cell Efficiency), high efficiency, III-V semiconductor, quantum-dot-enhanced, triple-junction solar cells designed and manufactured by Cyrium Technologies Inc. were integrated into OPEL Solar, MK-I, Fresnel-lens-based, 550x concentrating modules carried on a dual axis tracker.

Over its first year of operation 1.8 MWh of AC electrical energy was exported to the grid. Measurements of the direct and indirect components of the insolation, as well as the spectral irradiance of light incident on the demonstrator in Ottawa, Canada are presented. The system efficiency is measured and compared to that predicted by a system model to identify loss mechanisms so that they can be minimized in future deployments.

STATEMENT OF ORIGINALITY

Except where stated otherwise, the results presented in this thesis were obtained by the author during the period of his M.Sc. research project under the supervision of Dr. Karin Hinzer. They are to the best of his knowledge original.

ACKNOWLEDGMENTS

Dr. Karin Hinzer: Thank you for your ambitious desire to give your students responsibility, the opportunity to contribute within the SUNRISE project, and the privilege of sharing my research with and learning from the world's leading PV experts at the most renowned international conferences in photovoltaics.

Dr. Henry Schriemer: Thank you for your patient guidance, and your attention to detail as I began to publish my findings and write my thesis.

Alexander Walker: Thank you for your uncompromising style of scientific debate. Thank you also for the Sentaurus simulation results (band diagrams) which were a critical addition to my explanation of the triple junction solar cell in Section 2.2.

Olivier Thériault: Thank you for enthusiastic approach to growing your understanding of physics. Thank you also for the assistance you provided with respect to EQE measurements which I have included in Section 3.1.2.2.

Frank Szadkowski: Thank you for your assistance at the SUNRISE demonstrator test site during the SUNRSIE project. Thank you specifically for your practical, "can-do" attitude.

Allan Johnson: Thank you for your work setting up the first version of the remote data acquisition system for the SUNRISE project. This work has been expanded upon and now is the backbone for data acquisition for two of the SUNLab's major projects.

Graeme Jamieson: Thank you for all your work on the SUNRISE website. Maintaining an automated data collection system is not automatic, it takes work and I appreciate the help.

Frederic Bouchard: Thank you for wading through the megabytes of data that we collected over the past year. Your analysis helped identify the most interesting measures of the demonstrator's performance.

Tina and Randy Yandt (Mom and Dad): This thank you falls terribly short. Nevertheless, thank you for your love, your ongoing support, your advice and encouragement over the past two years, and listening to me when I couldn't resist talking about physics.

PUBLICATIONS

The following presentations resulted from work performed during the completion of this thesis.

1. **M. D. Yandt,** Invited Talk on behalf of Cyrium Technologies Inc.: III-V High-Efficiency Multi-Junction Solar Cells for Concentrated Photovoltaic (CPV) Deployments, Canadian Semiconductor Science and Technology Conference, Vancouver, BC, Aug.14-17 2011, University of British Colombia

2. **M. D. Yandt** et al., “A New On-Sun Test Facility at the SUNRISE Quantum-Dot-Enhanced CPV Module Demonstration System,” in Concentrating Photovoltaics Conference (CPV-7), 2011

3. W. Walker, J. F. Wheeldon, O. Thériault, **M. D. Yandt**, and K. Hinzer, “Temperature Dependent External Quantum Efficiency Simulations And Experimental Measurement Of Lattice Matched Quantum Dot Enhanced Multi-Junction Solar Cells,” in Photovoltaic Specialists Conference (PVSC), 2011 37th IEEE

4. O. Thériault, J. F. Wheeldon, A. Walker, P. Bitar, **M. D. Yandt**, C. E. Valdivia, K. Hinzer, “Temperature-Dependent Quantum Efficiency of Quantum Dot Enhanced Multi-Junction Solar Cells,” in Concentrating Photovoltaics Conference (CPV-7), 2011

5. C. E. Valdivia, S. Chow, S. Fafard, O. Theriault, **M. D. Yandt**, J. F. Wheeldon, A. J. SpringThorpe, B. Rioux, D. McMeekin, D. Masson, B. Riel, V. Aimez, R. Ares, J. Cook, T. J. Hall, F. Shepherd, K. Hinzer, “Measurement of High Efficiency 1 cm2 AlGaInP/InGaAs/Ge Solar Cells with Embedded InAs Quantum Dots at up to1000 Suns Continuous Concentration”, in Photovoltaic Specialists Conference (PVSC), 2010 35th IEEE, pp. 001253–001258.

6. **M.D. Yandt**, A. Johnson, C. E. Valdivia, K. Hinzer, “Remote Data Acquisition System for SUNRISE Solar Concentrator System and Monitoring Technologies”, Demonstration at TEXPO 2010 & CMC Annual Symposium, 2010, Ottawa, Ontario

TABLE OF CONTENTS

LIST OF FIGURES

LIST OF TABLES

LIST OF ACRONYMS

PV	Photovoltaics
CPV	Concentrating Photovoltaics
EQE	External Quantum Efficiency
IQE	Internal Quantum Efficiency
SUNRISE Project	Semiconductors Using Nanostructures for Record Increases In Solar cell Efficiency
APECS Project	Advancing Photovoltaics for Economical Concentrator Systems
ASTM	American Society for Testing and Materials
IEC	International Electrotechnical Commission
ISO	International Organization for Standardization
AM	Air Mass
AM1.5d, AM1.5g,	Geometric Air Mass value of 1.5 for the direct and global insolation
AM0	Air Mass of extraterrestrial insolation
SMARTS2	Simple Model of the Atmospheric Radiative Transfer of Sunshine
FF	Fill Factor
TCAD	Technology Computer Aided Design
OTF	Optical Transfer Function
MPPT	Maximum Power Point Tracker
L-I-V curve	Light-Current-Voltage curve

LIST OF SYMBOLS

$N_{photons}$	Number of photons
I	Spectral irradiance
E_{ph}	Energy of a photon
EQE_{si}	External quantum efficiency of silicon
λ	Wavelength
Q	Total energy radiated from a black body
ε	Emissivity of a grey body where $\varepsilon = 1$ represents a black body
σ	Stefan-Boltzman constant
A	Surface area
T	Temperature
t	Time
E	Energy
h	Planks Constant
c	Speed of Light
k, k_B	Boltzman Constant
e	Euler's number, base of the natural logarithm
θ	Zenith angle of the sun
I_d	Diode curent
V_d	Diode voltage
I_o	Saturation current
n	Ideality factor
q	Elementary charge
I_{mp}	Current at a solar cells maximum power point
V_{mp}	Voltage at a solar cells maximum power point
I_{sc}	Short circuit current
V_{oc}	Open circuit voltage
Rs	Series resistance
Rsh	Shunt Resistance
F_{nTop}, F_{nMid}, F_{nBot}	Quasi-Fermi levels of electrons in top, middle and bottom subcells
F_{pTop}, F_{pMid}, F_{pBot}	Quasi-Fermi levels of holes in top, middle and bottom subcells
ΔF_{Top}, ΔF_{Mid}, ΔF_{Bot}	Quasi-Fermi level separation in top, middle and bottom subcells

F_n, F_p	Quasi-Fermi levels of electrons and holes
E_i	Intrinsic-Fermi levels
n	Concentration of electron
p	Concentration of holes
n_i	Intrinsic carrier concentration
η	Efficiency
P_{MP}	Power extracted from the solar cell t the maximum power point
P_L	Light power, integrated spectral irradiance
X	Concentration, Number of suns
J_{ph}	Photo current density
Tr	Transmission function
E_g	Semiconductor bandgap
α,β	Varshni Parameters
J_s	Saturation current density for a two diode solar cell model
J_r	Recombination current density for a two diode solar cell model
n_s	Saturation emission coefficient (or ideality factor of n = 1)
n_r	Recombination emission coefficient (or ideality factor of n = 2)
χ	Temperature exponent for a two diode solar cell model

1 Introduction

As the need for economically viable clean energy solutions grows it is becoming ever more apparent that photovoltaics (PV) will play a critical role. In the near term, an appropriate mix of renewable energy sources to supplement current electricity production is the most environmentally responsible and achievable response to our increasing demand for electrical power. PV is an essential part of this mix, with fundamental advantages when it comes to scaling, reaching remote populations, and minimizing environmental footprints. The challenges that remain require engineering solutions rather than physical breakthroughs and both government and industry have begun to recognize this fact.

Numerous photovoltaic alternatives have been demonstrated [1] but the high theoretical efficiency limits of concentrated photovoltaic (CPV) strategies are hard to ignore. At present, the maturity of silicon based PV solutions instills the confidence that investors need to justify large scale deployment, but other PV technologies are improving extremely quickly. The goal of this thesis is to demonstrate an understanding of the challenges faced when deploying concentrated photovoltaic (CPV) systems and to analyze the performance of one such a system.

As part of the SUNRISE project (Semiconductors Using Nanostructures for Record Increases in Solar-cell Efficiency), III-V semiconductor quantum-dot-enhanced triple-junction solar cells designed and manufactured by Cyrium Technologies Inc. have been integrated into OPEL Solar MK-I Fresnel-lens-based 550x concentrating modules carried on an OPEL Solar dual axis tracker. The process of instrumenting, modeling and analyzing the performance of the SUNRISE demonstrator is thoroughly documented in this thesis.

1.1 Thesis Overview

The rest of Chapter 1 will attempt to frame the current work in order to give it context within the photovoltaic industry. It will demonstrate the motivations of the industry and the challenges that it has faced or will face in the near future. The fundamental reasons for pursuing the solar resource, the practical and physical limits to harvesting solar energy and the economics involved in moving the industry towards grid parity are also discussed.

The basics of the concentrator photovoltaic (CPV) strategy are presented. The solar resource and the effects of the earth's atmosphere on the resource are explained. A subset of the current state-of-the-art CPV solutions is presented with references to give the reader a feel for the breadth of the industry worldwide.

1.1.1 Chapter 2 – Theory

Chapter 2 discusses the fundamentals of an equivalent circuit analysis of a solar cell and then continues on to explain the inner workings of a high efficiency triple junction solar cell. This intuitive theoretical understanding is the basis upon which the analysis in this thesis is built. When attempting to grasp the fundamentals it is important to be able to visualize the mechanics. Thus, the explanation will be presented with reference to the energy band diagrams of a generic triple junction cell.

1.1.2 Chapter 3 – Measurements, Equipment and Experimental Techniques

In Chapter 3 the instrumentation and equipment used to measure the performance of high efficiency solar cells and the SUNRISE demonstrator as a whole is described. The experimental techniques used both indoors and outdoors to collect data are presented. The findings are described and an analysis of various artifacts is given.

1.1.3 Chapter 4 – CPV System Model

Chapter 4 describes the system model that was developed to take into consideration all of the measured data that is collected and thus determine the theoretical influence of various physical effects on the system. The model uses a cell's optical and electrical characteristics measured in the laboratory, and the characteristics of the modules, tracker, incident light and climatic conditions measured outdoors to explain the performance of the demonstrator system. The goal of this exercise is to identify the system effects that limit the overall efficiency of energy harvest. These issues can thus be addressed in order to bring CPV system efficiencies closer to record cell efficiencies. The issues that require further investigation are highlighted.

1.1.4 Chapter 5 – Conclusions

A summary of the SUNRISE demonstrator system performance since it was installed in October 2010 is provided. The results gathered through modeling of the system are presented and issues that require further investigation are identified as future work.

1.2 Background: The Birth of Photovoltaics

The term photovoltaics describes any method that takes advantage of the photovoltaic effect to convert incident light directly into electricity. The photovoltaic effect, first discovered by Edmund Becquerel in 1839 [2] is the process whereby an electron absorbs the energy of an incident photon and is promoted from a semiconductor's valence band to its conduction band. The result is an electron-hole pair, the term 'hole' describing the available state in the valence band from which the electron was promoted. If a clever means of separating this electron-hole pair can be achieved then the electron and the hole can be collected at opposite ends of a device as electrical current. It turns out that this requirement is precisely satisfied by the application of a p-n junction.

In its most basic form a p-n junction is created when two types of semiconductor material, one doped with acceptor ions, and the other doped with donor ions, are allowed to exist in intimate contact with one another. At room temperature, a gradient in the concentrations of available charge carriers (electrons and holes) on either side of the material boundary results in the diffusion of carriers from one side of the boundary to the other. At equilibrium, this diffusion current is exactly equaled by an opposing drift current that occurs as a result of the charge that builds up when carriers diffuse across the boundary between the two initially charge neutral materials.

The basic theory governing the operation and electrical characteristics of a p-n junction was first published in 1949 by William Shockley [3]. Shockley published a second paper on the topic in 1950 [4] after which research and development in the microelelectronics industry surged forward in an attempt to develop and commercialize the solid state transistor. The microelectronics industry began its exponential growth in 1954 when Texas Instruments produced the first silicon based solid state transistor [5]. The industry has worked to understand and perfect the materials, processes and growth techniques necessary to build intricate solid state devices for the 50 plus years since. This rapid growth meant the development of the same technologies that are necessary to achieve state-of-the-art photovoltaic solar cells. Efforts towards photovoltaic applications however, were dwarfed by the success of the electronics industry until the early 1970's when two important pieces were added to the puzzle. First, it became clear that the technology existed, at least in theory, to build solar cells that yielded a respectable output power and second, interest in alternative energy sources grew overnight with forecasts of a worldwide energy crisis.

1.2.1 The Solar Industry: Motivation for Photovoltaics

Silicon solar cells were the first photovoltaic technology to be commercialized due to the wealth of knowledge and expertise that could be transferred directly from the microelectronics industry. As a result, with an energy crisis approaching, the 1970's saw the first substantial investments in silicon based photovoltaics. During this time numerous research facilities began investigating the potential avenues to achieve economically viable photovoltaic devices. Silicon based devices dominated the field, the only other technologies under serious study being those intended for extraterrestrial applications which were not expected to be economical for terrestrial applications in the near future. Numerous small scale deployments were made and it quickly became apparent that the reliability of the panels would have to improve if there was even a chance that the technology would be accepted.

The industry moved quickly to establish standards that would help manufacturers qualify their products. The US Department of Energy instituted the Low-Cost Solar Array Program through which the first set of module qualification tests were published in 1981 by the Jet Propulsion Laboratory [6]. Since this initial set of qualification tests known as the Block V qualification sequence, numerous other organizations have proposed and implemented more comprehensive and broadly applicable standards for reliability, safety and qualification testing [6]. The range of PV technologies, however, make standard testing procedures across the industry practically impossible to realize. Even the most current standards maintained by The International Electrotechnical Commission (IEC), the American Society for Testing and Materials (ASTM International) and the International Organization for Standardization (ISO) continue to evolve.

Early setbacks with respect to reliability did not distract business minds who understood the fundamental benefits of converting light directly into electricity using photovoltaic technology. Not only was photovoltaic technology positioned as a clean energy alternative but it also had the potential to capture a portion of the multibillion dollar energy market worldwide [6].

Between 1980 and 2000 flat panels became extremely reliable thanks to the investment manufacturers made to improve their testing and qualification practices. Unfortunately, solar energy was still viewed as an extremely expensive energy alternative. The average cost of an installed PV system over this time period declined steadily from over $10 per Watt in 1980 to less than $4 per Watt by 2000. [7] Figure 1-1 shows an experience curve which indicates the average reduction in module cost for PV installations of various technologies between 1990 and 2010.

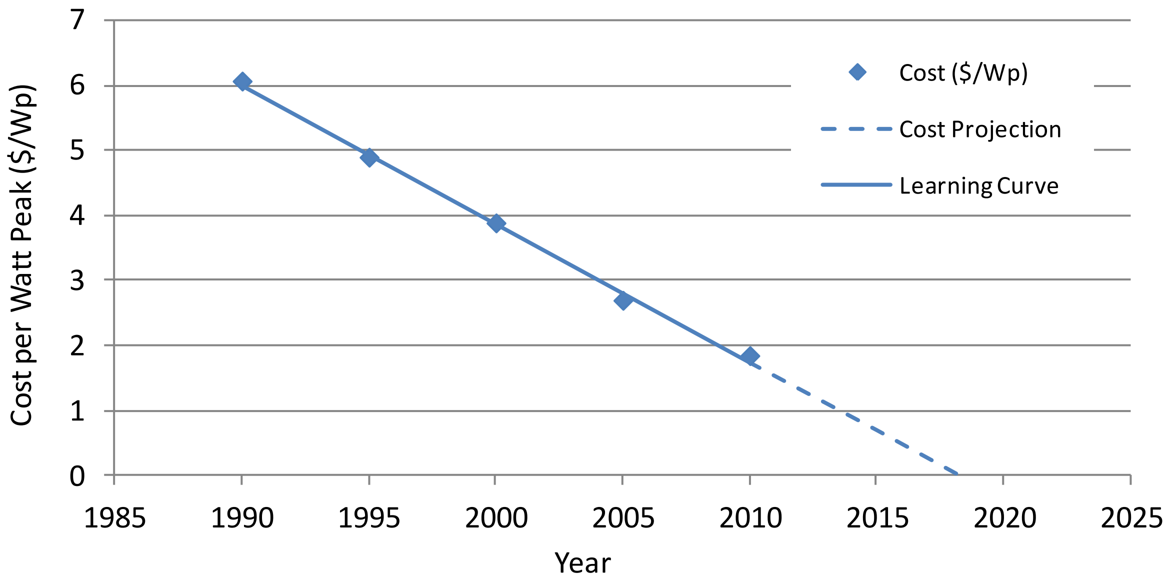

Figure 1-1: Learning curve describing the reduction in installed PV system cost between 1990 and 2010. Module costs are projected to continue decreasing in the near term while the industry is young but as the technologies mature costs will begin to asymptote. The cost of the mature silicon technology of today is not expected to fall much below $1 per watt. Cost reductions are a result of process cost reductions (economies of scale, materials, automation) and Improved cell efficiencies (cell structures, manufacturing process, materials innovation) [8]**.**

By 2005 panels were being sold with twenty year manufacturer reliability guaranties and the first large scale deployments were being announced as a result of lucrative government incentives in many countries including Germany, Spain, and the United States. Before this point various flavours of silicon flat panels captured niche markets but the high cost of materials, and relatively low system efficiencies (on the order of 15% at the turn of the millennium) prevented the cost per Watt from falling to a level that would justify investment in the absence of a subsidy. As a result, market penetration was limited [9]. Since 2005, environmentally responsible governments that want to be technology leaders in the near future, when the price of photovoltaic electricity reaches grid parity, have decided to offer such incentives.

The first incentive programs were quite successful (with a few exceptions) but the PV industry had already recognized that in order to achieve long term success the cost of modules would have to continue to decrease. It was also apparent that costs would have to fall below the lowest prices achievable with first generation PV shown in Figure 1-2 (i.e. single junction crystalline silicon PV).

This realization stemmed from the fact that single junction silicon technology had matured and was approaching its theoretical performance limit. Some reductions in the cost of module manufacturing and system deployment could still be made but new strategies needed to be developed if cell efficiency, the largest driver of overall system cost, was going to continue to increase.

Figure 1-2 shows a map of the relative position of second and third generation PV alternatives. Second generation devices include novel low cost technologies such as the many varieties of thin film PV. Third generation devices include the highest efficiency III-V based solar cells that have been produced to date. The various 2nd and 3rd generation technologies are listed with their record efficiencies in Figure 1-3. It is clear from Figure 1-2 that cell efficiency is the single largest driver of a PV system's cost-per-Watt metric [9]. This is due in part to the fact that high efficiencies can be leveraged to achieve lower costs as is the case for concentrated photovoltaic (CPV) solutions which will be discussed shortly.

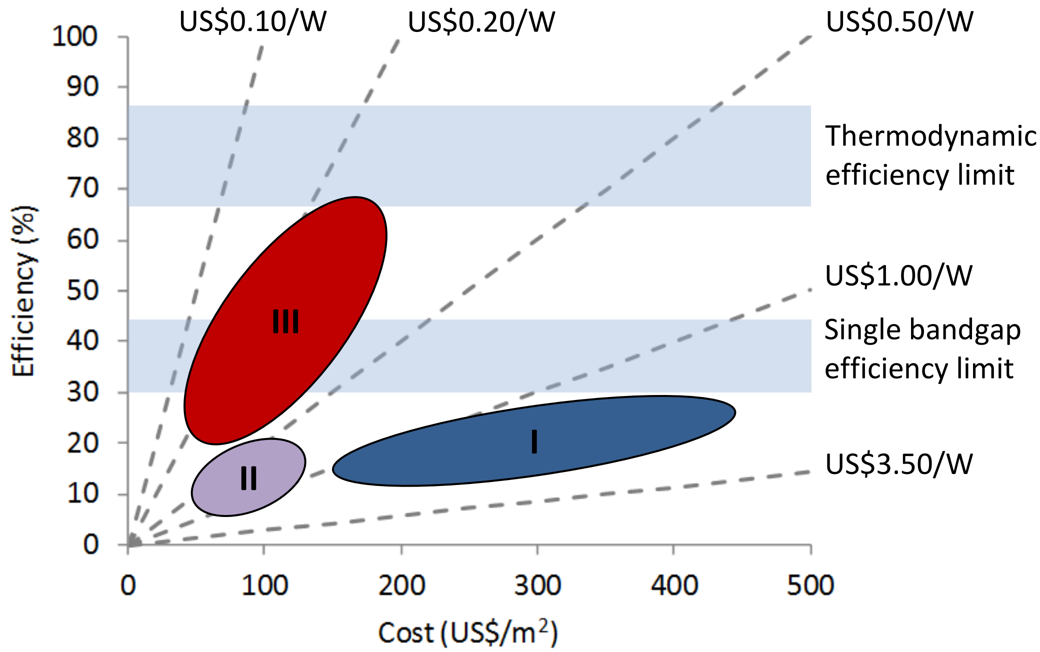

Figure 1-2: Efficiency-cost map of 1st, 2nd, and 3rd generation PV technologies labeled I, II, III respectively. The coloured ovals overlay the range of system costs that are theoretically achievable given the efficiencies exhibited by the various generations of PV technologies. Dashed lines represent the cost-per-Watt peak to install a system. The tinted areas represent theoretical limits: 30-44% representing the single bandgap limit and 67-87% representing the thermodynamic limit on cell efficiencies the ranges depending on the concentration level of incident light [10], [11]**.**

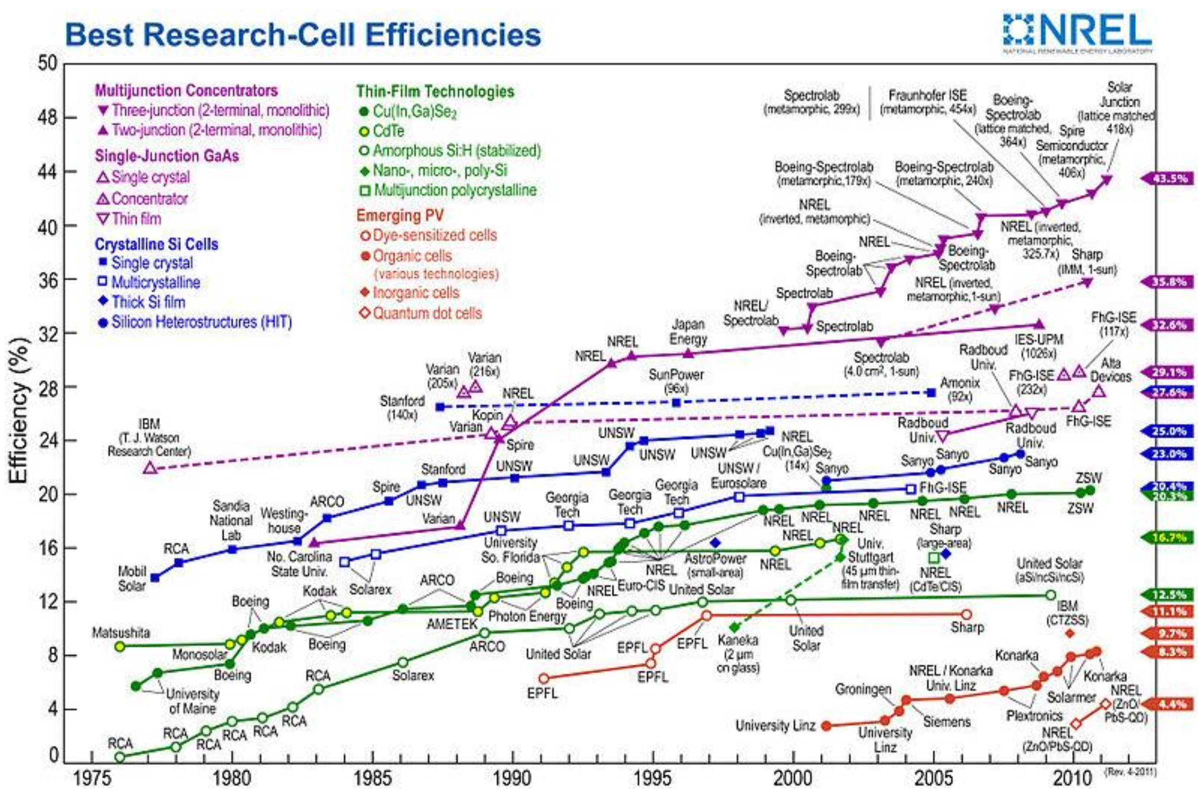

Figure 1-3: NREL's famous record of laboratory measured cell efficiencies showing multijunction concentrator cell efficiencies crossing the 30% threshold in the mid 1990's and today's efficiency record at 43.5%. [1]**.**

1.2.2 Limits of PV Performance

The reasons that a single junction cell has a relatively low theoretical efficiency limit (30-44% depending on concentration as shown in Figure 1-2) are fundamental to understanding the motivation for devices with multiple junctions, so they are presented here.

The principle is easily visualized by first looking at the subset of photons that a single junction cell harvests compared to the number and wavelength of photons in the spectrum incident on the cell. The number of photons that are absorbed, to produce electron-hole pairs that are eventually collected, is calculated by multiplying the incident photon spectrum by the external quantum efficiency of the solar cell according to:

$$N_{photons}(\lambda) = \frac{I(\lambda)}{E_{ph}(\lambda)} \cdot EQE_{si}(\lambda), \quad (1)$$

where $N_{photons}(\lambda)$ is the harvested portion of the photon flux in # of photons/s/m^2/nm, $I(\lambda)$ is the spectral irradiance of the reference spectrum in W/m^2/nm, $E_{ph}(\lambda)$ is the energy of a photon and $EQE_{si}(\lambda)$ is the external quantum efficiency (See Appendix B for a description of quantum efficiency) of a single junction silicon solar cell. This calculation is performed and plotted using the ASTM G173 reference solar spectrum (discussed further in Section 1.3.2) and the EQE of a generic silicon solar cell in Figure 1-4.

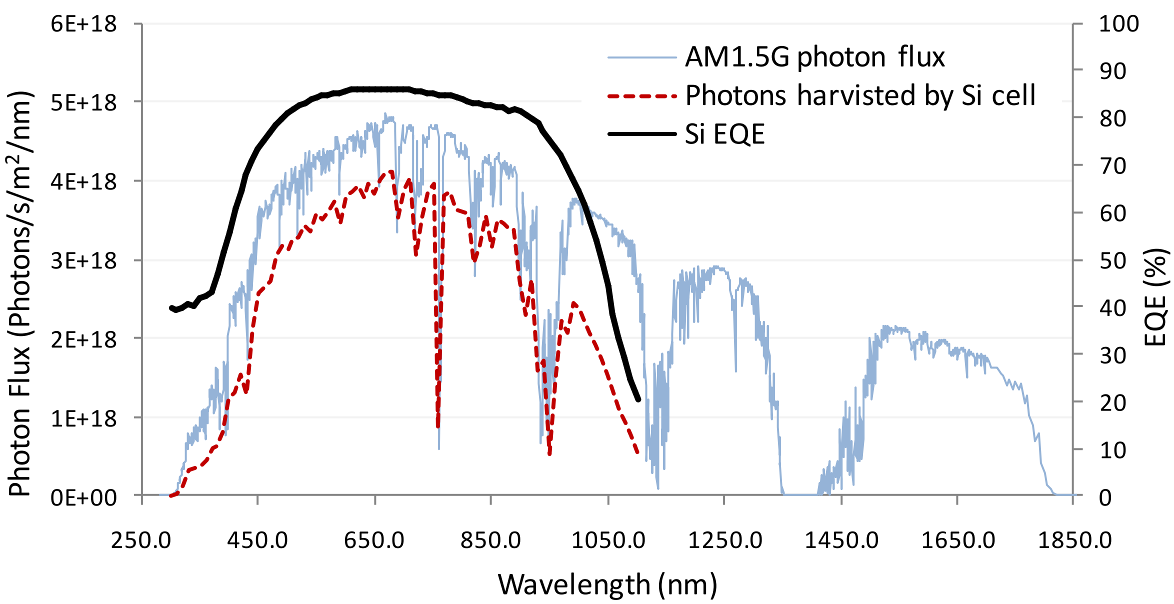

Figure 1-4: Photons collected by a single junction silicon solar cell. The fine blue line represents the photon flux of the standard spectrum. The red line represents the portion of the incident photons that have energy greater than the bandgap of Silicon that are actually harvested by the solar cell. The EQE of a generic silicon solar cell is shown by the thick black line which is plotted against the right hand axis.

The fine blue line is the incident photon flux of the standard spectrum. This represents the number of photons that are available for capture at every wavelength. The area under the red dashed curve is proportional to the current produced by a single junction silicon solar cell. Only the photons that have energies greater than the bandgap of silicon (1.12eV ~ 1100nm) are harvested. On the right hand side of the figure no photons are captured because they did not have enough energy to create an electron hole pair by promoting an electron 1.12eV from the valence band to the conduction band. Silicon is transparent to these wavelengths so any of these photons that are not reflected from the surface are simply transmitted and do not contribute to electrical power output.

The area under the photon flux (thin solid line) and above the harvested portion (dashed line) represents photons that were reflected at the surface of the solar cell or absorbed creating an electron hole pair that recombined before it could be separated and collected as current.

There is another important loss mechanism called thermalization loss that is not apparent when considering the number of incident photons but becomes very evident when looking at the power distribution of the incident spectrum as in Figure 1-5. The loss mechanisms mentioned above are illustrated in Figure 1-6.

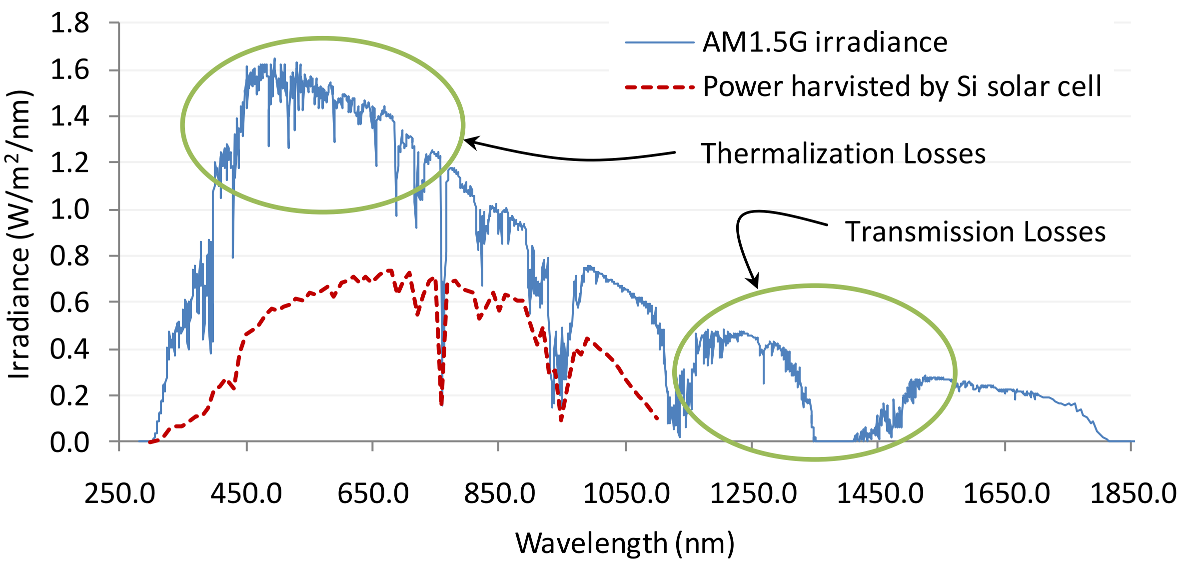

Figure 1-5: Thermalization and transmission losses in single junction solar cells. Spectral power distribution of the standard spectrum and the portion of power harvested by a silicon solar cell.

Thermalization losses include any losses of power that result from the absorption of a photon with energy greater than the bandgap of the active material. The process is depicted on a band diagram in Figure 1-6 along with the three other major loss mechanisms inherent in a pn-junction solar cell. The band diagram is a plot of energy vs. distance from one side of a junction to the other. The diagram is not to scale, nevertheless, a band diagram helps to illustrate where energy is lost as a solar cell harvests energy.

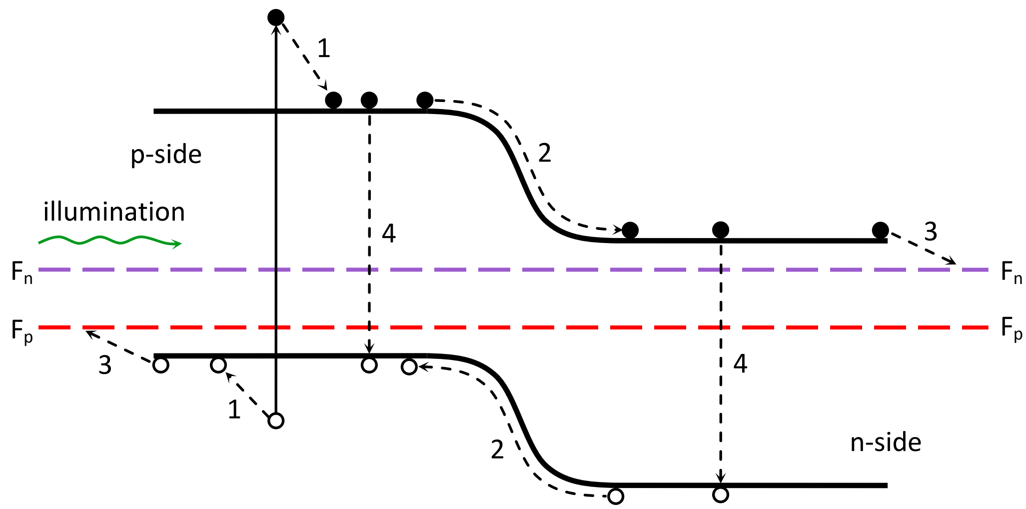

Figure 1-6: Inherent loss mechanisms in a pn-junction based solar cell. 1) Thermalisation Losses, 2) Junction Losses, 3) Contact Losses and 4) Recombination Losses

As shown in Figure 1-6 a single pn-junction solar cell cannot take full advantage of the power contained in photons with energies higher than the bandgap energy. These photons are absorbed but the excess energy is simply lost to phonons resulting in lattice vibrations. Thus the excess energy is converted into heat and not electrical power.

The question then is twofold, how does one design a solar cell that simultaneously harvests a larger portion of the solar spectrum (especially photons on the red side of the spectrum) while also taking full advantage of the energy contained in photons on the blue side of the spectrum?

The answer has been known since the 1980's when the first tandem cells were developed [1]. Tandem cells take advantage of two pn-junctions each made with a different semiconductor material and associated material bandgap. When stacked on top of each other the top junction, with a relatively high bandgap, (referred to as the top subcell) harvests all of the high energy photons and transmits any photons with energies lower than its bandgap. The transmitted photons are then collected in a similar fashion by the bottom subcell which has a much lower bandgap. In principal, if materials can be achieved that allow the ideal bandgap combination for a tandem cell to be realized then more photons are collected because the bandgap of the bottom is lower than that of silicon, and more of the energy in each photon can be captured because of the higher bandgap of the top subcell.

This same idea was extended to a triple junction cell in the late 1990's when three subcells were epitaxially grown on top of each other, electrically connected in series, and lattice matched to a germanium substrate. An example of such an architecture is given in Table 1 in Chapter 3 where the theory of triple junction cell operation is explained more thoroughly.

Around the turn of the millennium multijunction devices were expensive to manufacture and were practical only for extraterrestrial markets for which power density rather than cost was the primary design point. However, as efficiencies continued to increase it was more and more conceivable that the high efficiencies of multijunction devices could be leveraged by incorporating them into concentrator systems and that these systems might be economically viable in terrestrial applications [10]. These so called third generation devices, exposed a whole new bubble on the efficiency vs. cost map shown in Figure 1-2. At present, state of the art multijunction devices have reached 43.5% efficiency [1] under the G173 AM1.5D reference spectrum.

The value proposition in the CPV industry is straight forward. Produce a solar cell with as high an efficiency as possible and then offset the cost of its manufacture by concentrating sunlight onto only a very small cell with a large area concentrator made of a relatively inexpensive material. This achieves two desirable outcomes at once. First, the total active solar cell area required, and hence the cell cost, is drastically reduced. It is reduced 500-1000 times at typical concentration ratios of 500-1000suns. Second, increasing the intensity incident on a solar cell addresses the difficulties associated with achieving the Shockely-Queisser efficiency limit [12]. This limit will be discussed further in Chapter 3 but for now this means that the cell benefits from a fundamental increase in efficiency with increasing incident intensity.

The number and diversity of alternatives when it comes to designing concentrating systems is incredible. Despite the diversity of the available solutions all of these systems attempt to address the same list of design considerations. The main considerations common to all CPV systems are outlined in the following section.

The performance analysis of the SUNRISE demonstrator presented in chapters 3 and 4 is intended to identify how well a specific CPV system performs in the field. A keen understanding of the integrated system performance is critical if system efficiencies are going to approach cell efficiencies. Ultimately, it is the stable long term system efficiency that the industry is interested in maximizing. Only by deploying and monitoring systems and verifying the links between system performance and every step of the manufacturing process can design improvements be made. Decoupling the factors that contribute to the measured system performance is not a trivial task which is why there is incredible value in studying state-of-the-art deployments at this point in the development of the CPV industry.

1.2.3 Cost Drivers of Solar Energy: The Case for CPV

Ultimately, the rate of deployment and growth in the PV industry is determined by the levelized cost of energy (LCOE) that PV can provide. The LCOE describes the cost of energy amortized over the life of the system that produces it. It is calculated by taking the ratio of all associated system costs to the total energy produced by the system over its useful life. Equivalently, the LCOE is the ratio of the systems lifecycle cost to the systems lifetime energy production [13].

The calculation is complicated by the number of costs that need to be taken into consideration which include: modules, inverters, installation materials, trackers, labour, permitting and commissioning, land, site preparations, overhead, profit, and taxes among other costs as well as ever changing incentives such as feed in tariffs (FITs) which have become popular with governments trying to stimulate and regulate the growth of the industry [14].

Perhaps the most enlightening way to look at the LCOE is to consider it the average price of electricity required to get a net present value of zero when performing a discounted cash flow analysis [15]. This highlights the need for PV to reach grid parity which is currently predicted by some to happen around 2016 as shown in Figure 1-7 [16], [17]. While interesting visually, this chart is based on broad averages when it comes to specifying useful life of a PV system and the amount of insolation. Inputs such as the amount of sunshine or even the local cost of power from the grid that are unique to a particular location are more clearly accounted for in Figure 1-8 produced by the US Department of Energy within the Solar America Cities Program which looks as the solar resources, incentives, and price of electricity in specific market locations.

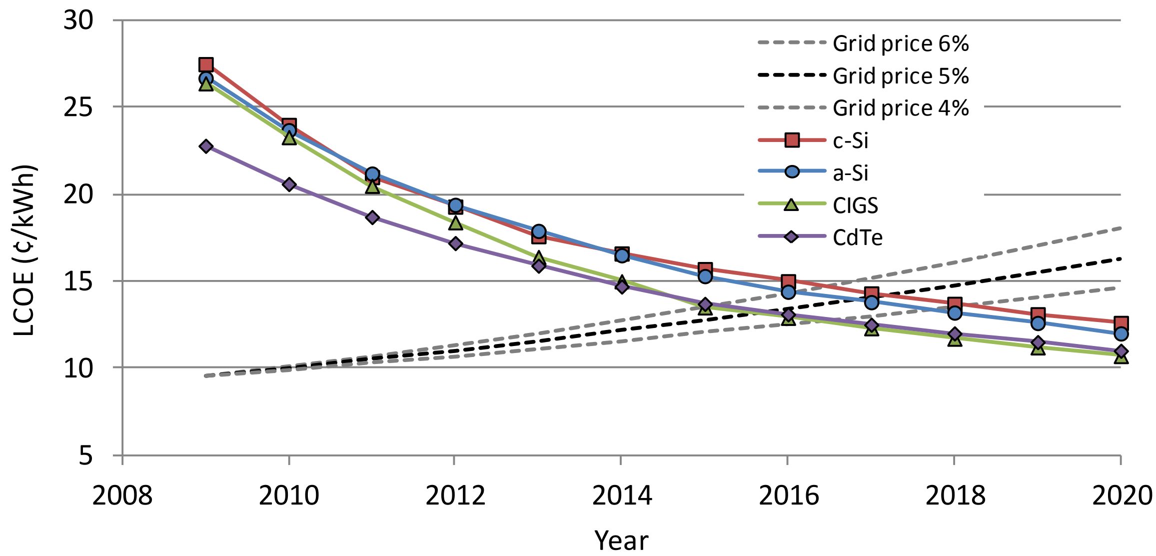

Figure 1-7: The LCOE of the most mature PV technologies on the market as of 2009 were predicted by Deutsche Bank to continue to decrease through 2020 at which point the LCOE of these technologies is expected to be lower than the average market price of electricity. The average cost of electricity from the US grid in 2009 was 9.5 cents/kWh and based on a 4-6% inflation rate costs are projected to surpass the LCOE of PV systems around year 2016. These trends are in large part due to the expected increases in demand that the energy sector will see between now and 2020 because this will simultaneously increase the grid price and increase PV deployment which will drive costs down along the industries learning curve [16], [17]**.**

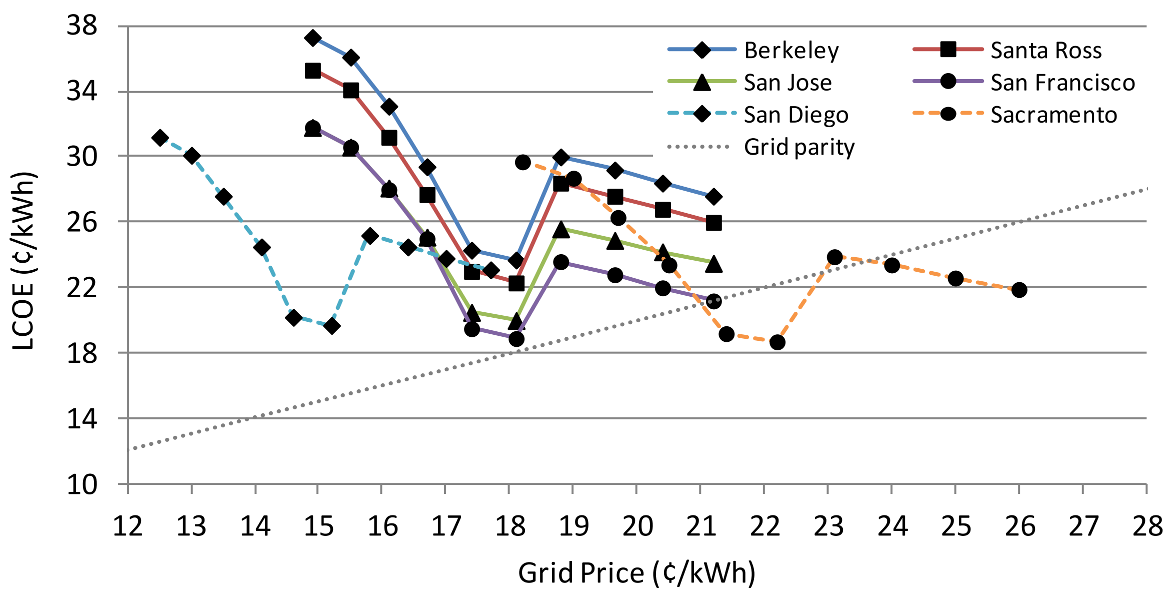

Figure 1-8: Solar America Cities Program LCOE Calculations. Each series of connected points represents the LCOE of PV and the corresponding grid cost over time for a particular US city. The upper left hand point in each series is for 2011. The lower right hand point in each series is for 2020 [16]

In Figure 1-8 the cost of electricity from the grid in Berkeley, Santa Rose, San Jose, and San Francisco are expected to be approximately equal to each other through 2020 but due to differences in the solar resource and local subsidy structure there is a significant difference in the LCOE from PV. Conversely, Sacramento, San Francisco, and San Diego all have very similar solar resources but due to other circumstances do not see the same grid cost. The dip and then sudden increase in PV cost present in all of the plots is due to the termination of US wide green energy subsidies that are scheduled to be phased out in 2016 [16].

In the near term government incentives are needed in order to stimulate the growth of the PV industry. Incentives encourage deployment which causes manufacturers to increase capacity which causes costs to be reduced. Incentives also help companies all along the PV supply chain to build the required infrastructure and gain the required expertise that is necessary if the industry is to continue following its current learning curve.

Eventually however, government incentives will no longer be feasible and the PV industry will have to stand on its own. It has been known for some time that in order to achieve grid parity without subsidy, the installation cost of PV systems must fall below $1 per Watt [18]. At this price installation of modules will achieve a LCOE that is competitive with the grid in the sunniest areas. Further reductions in cost and/or improvements in system efficiency will broaden the list of economically feasible deployment sites.

The concept of a learning curve or an experience curve is extremely helpful for visualization when trying to identify the rate of cost reductions of the industry as a whole [18]. Figure 1-9 shows the most current learning curve for the PV industry. This type of plot can tell us a great deal about the state of the PV industry. The blue and green data points show the price per Watt of PV modules for the cumulative deployment level and the year respectively. Plotted on a log-log scale the cost vs cumulative deployment is almost linear since the late 1970's and thus this trend can be projected into the future to predict the industries future progress. The decrease in PV module cost between 1976 and 2000 was largely due to the development of the ubiquitous crystalline silicon flat panel.

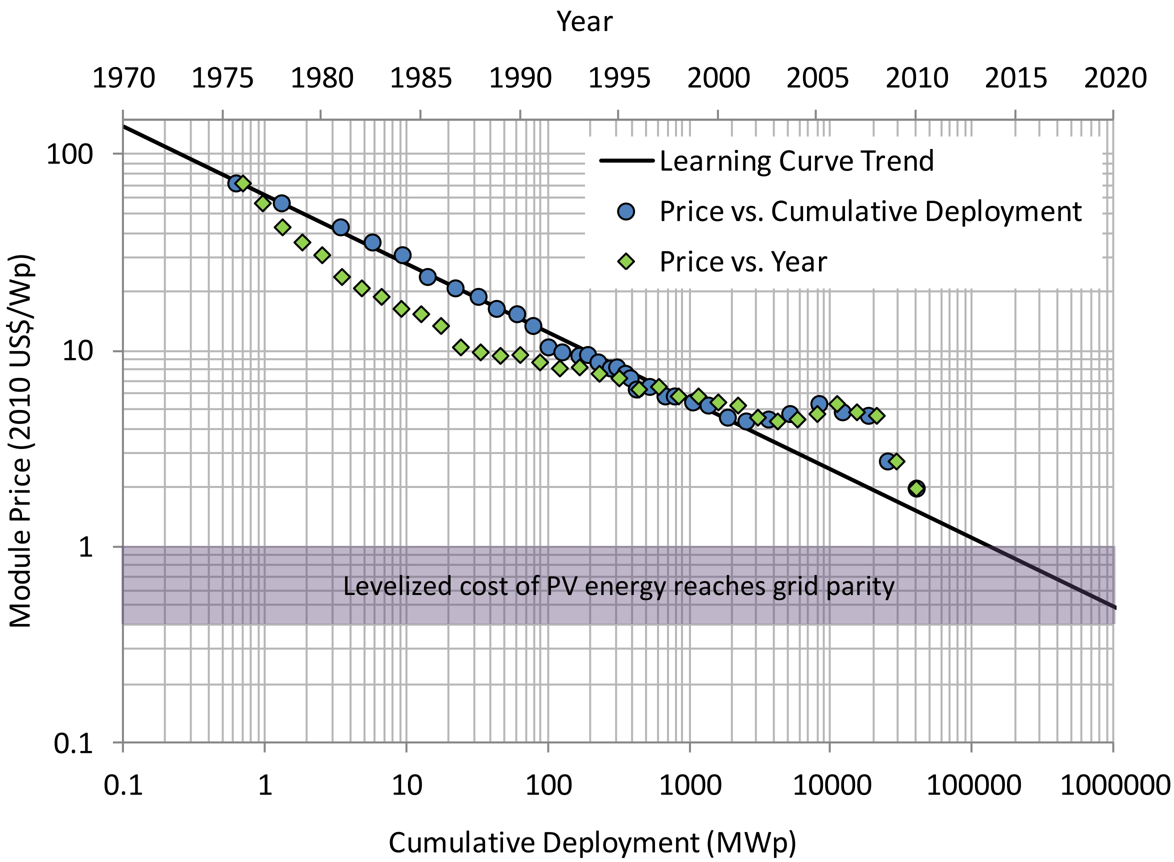

Figure 1-9: Learning curve shows the decrease in PV module cost with deployment and with the year since 1970 between 1970 and 2010 [13]**.**

An interesting artifact in this curve is the deviation from the learning curve between about 2003 and 2009 which corresponds to about 3-40GW installed capacity [19]. This deviation was largely due to the volatility of the cost of poly-silicon as a raw material which reached over $500 per kg in 2004 before new production capacity ramped up around the beginning of the 2009 recession and brought the price back down. The price is currently near $50/kg but is expected to increase slowly again toward the end of 2011 [13], [20].

The difficulty is that flat panel silicon technology has reached maturity and as such silicon module costs are not expected to fall at the same rate as they have for the past several decades. If the industry is going to continue to maintain the current annual reduction in module cost, technologies other than crystalline silicon flat panels are going to make this possible. Figure 1-10 identifies thin film and CPV technologies as the most likely PV strategies to achieve this continued reduction in system cost. This is interesting because these alternatives approach the cost problem from opposite sides. Thin films offer the potential for extremely low cost production which more than makes up for the relatively low efficiencies that these technologies exhibit. CPV systems on the other hand take advantage of relatively expensive but far more efficient solar cells and attempt to reduce system cost by concentrating light with inexpensive large area optics. Optics that are 500-1000 times larger than the PV element itself thus reduce the required active cell area and cost by 500-1000 times. Due to the relatively small amount of active material in the system the cell cost becomes a much smaller component of the balance of systems cost. It then becomes advantageous to spend a little bit more and make the highest efficiency cell possible to harvest the concentrated sunlight. Hence, CPV is considered a high cost, high efficiency alternative compared to the low cost, low efficiency thin film alternative.

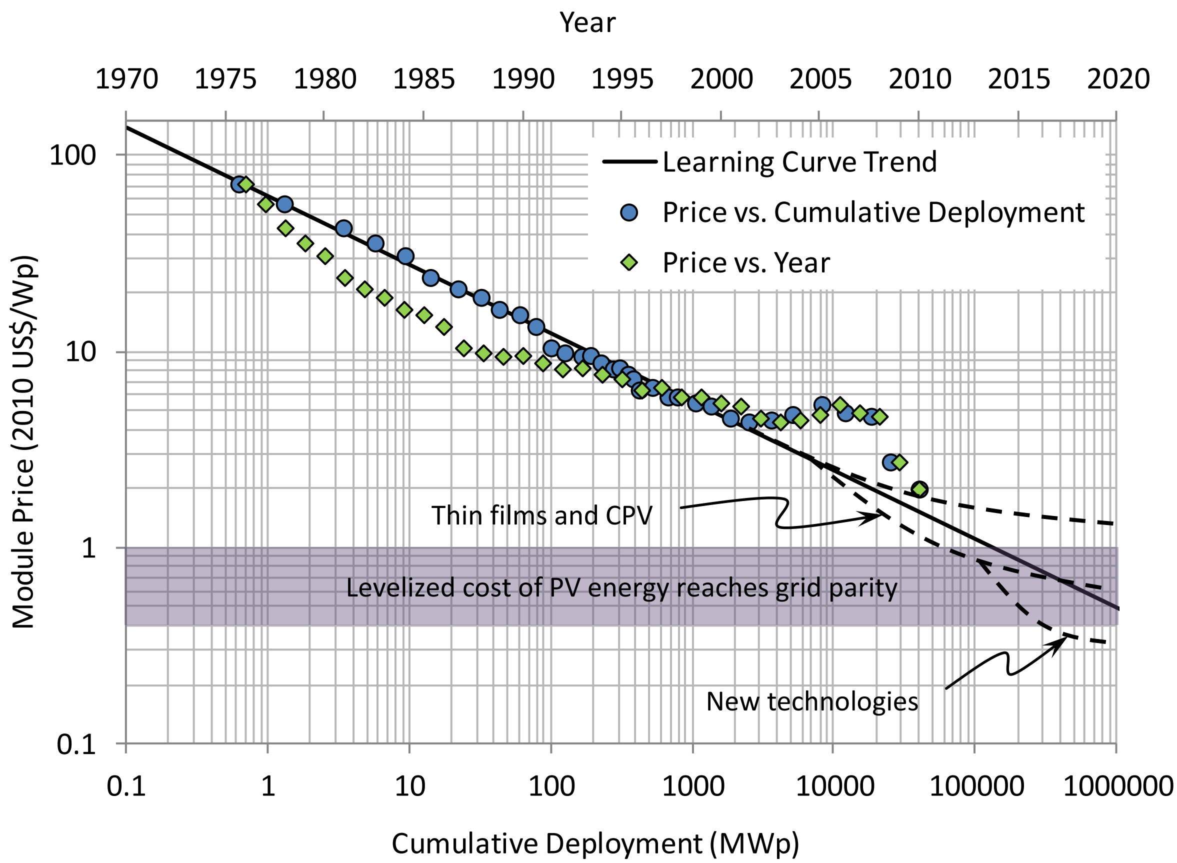

Figure 1-10: Learning curve shows the expected decreases in module cost. Unfortunately silicon technology is quite mature and is not expected to fall below $1.00 per Watt-peak (Wp). Thin films and concentrating technologies on the other hand are already beginning to push the cost curve below $1/Wp. [21]

Both CPV and thin film technologies have the potential to move up and left through the third generation bubble shown in Figure 1-2. Thin film manufacturers will attempt to achieve this by producing high efficiency cells that are similar to those currently used in CPV applications but using the same low cost deposition techniques as second generation devices. Many viable methods are currently being pursued to produce higher efficiency concentrator cells and the gap between current cell efficiencies and the theoretical limits means that there is still significant room for improvement given improved understanding of material compatibility and growth techniques. The potential for significantly higher efficiencies using the same manufacturing processes that are used currently, presents a major opportunity and is part of the motivation for the present work.

The challenge remaining in the CPV industry, which this work aims to address, is to bring system efficiency as close as possible to cell efficiency and to ensure that the more complicated system required (2d tracking, concentration, alignment, thermal management etc.) is reliable for 25 plus years. Achieving these goals will allow CPV system deployments to fully leverage the high cell efficiencies.

1.3 The CPV System: Components and Design Considerations

This section will outline the major challenges and sources of complexity when designing a CPV system. The present work (specifically results presented in Chapters 3 and 4) attempts to show how the integrated system functions as a unit. Figure 1-11 shows the optical train of the SUNRISE demonstrator. The optical components illustrated in the schematic are built into a module on the SUNRISE demonstrator. Components of a CPV system that are not shown in the schematic include: a heat sink, to which the cell receiver is bonded in order to dissipate excess heat, a solar tracker, required in order to point the modules at the sun, and an inverter which converts DC power to AC power and facilitates its export to the grid.

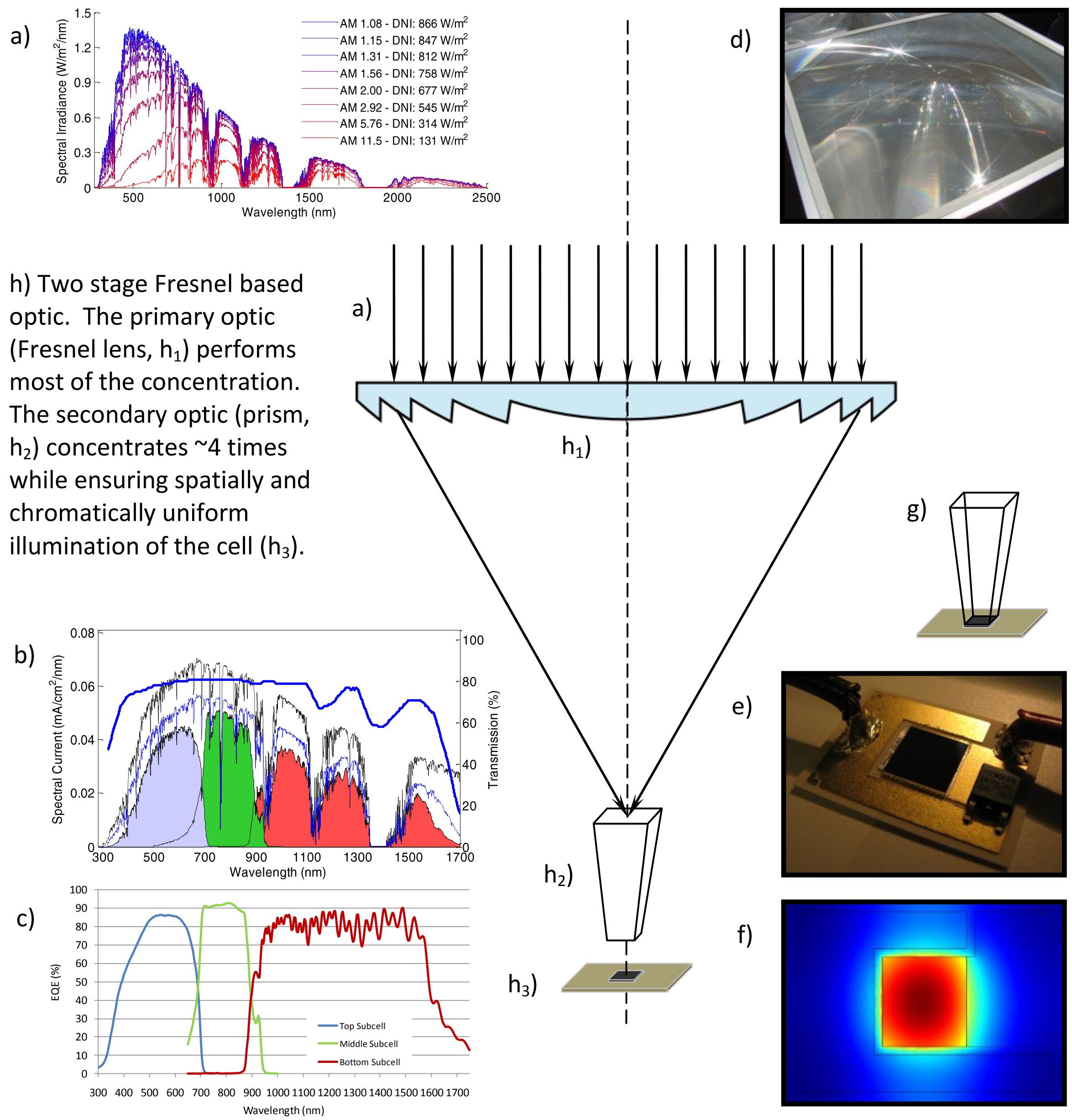

Figure 1-11: Expanded schematic of a Fresnel based concentrating system. Schematic not to scale.

The following are the various components of a CPV system that are highlighted in Figure 1-11.

a) The solar resource is an extremely important variable when evaluating any PV system. Depicted is the spectral irradiance of direct sunlight incident on the module. (see also Figure 1-13) Only the direct portion of the solar insolation (the DNI) is focused by the Fresnel lens onto the secondary optic and in turn onto the cell. Thus the spectral irradiance of the DNI precisely characterizes the solar resource that a CPV system attempts to convert into electricity. The spectral irradiance can be measured with a spectroradiometer mounted on the tracker beside the CPV modules. A pyrheliometer measured the total power of the DNI (the integral of these spectral irradiance plots) directly. A pyranometer and a shading disk measures the total power of diffuse light (that will not be harvested by a CPV system) striking the surface of the modules on a tracker.
b) Any optics placed between the sun and the solar cell will have an effect on the spectrum of the light incident on the solar cell. The difference between the spectral irradiance incident on the module and the spectral irradiance incident on the cell can be considered a wavelength dependent transfer function. In this report this is called an optical transfer function (OTF). An example of a simulated OTF is given (see also Figure 4-5) but this is only a simulated result. The measurement of the OTF of the OPEL Solar concentrating optics is recommended as future work in this report.
c) Triple junction external quantum efficiency of a Cyrium solar cell (see also Figure 3-32) The external quantum efficiency (described further in Appendix B) describes the absorption properties of the solar cell. The portion of the solar spectrum that is converted into electrical current by the solar cell is shown in b) where it can also be compared to the spectrum before and after the concentrating optics.
d) Photo of an OPEL Solar Fresnel based module. Six such optics make up one module.
e) Photo of a Cyrium solar cell on a receiver. A bypass diode and pigtails are also visible in the photograph.
f) Temperature map on the surface of the cell. This simulated result shows the importance of thermal management in a CPV system. Although the heat sink is not shown in Figure 1-11, dissipating excess heat is critical in all CPV systems.
g) The secondary optic is shown bonded to the surface of the solar cell. In a commercial system the anti reflection coating on the solar cell would be optimized for a transition from the refractive index of the prism to that of the top junction of the cell. Light focused on the top of the prism is guided by total internal reflection to the surface of the solar cell.
h) The primary optic (the Fresnel lens), the secondary optic (the prism) and the cell on its receiver are shown in an expanded schematic representation of the OPEL Solar module.

1.3.1 The Solar Spectrum: Understanding the Resource

The sun is an abundant source of energy. It is informative and interesting to look at the resource from a global perspective before zeroing in on the details so we will attempt this presently.

The sun's energy is generated via nuclear fusion in which hydrogen is converted to helium. With a core temperature of an estimated 15.7 million Kelvins and a surface temperature of ~5780K the sun can be thought of as a black body radiator and thus its energy output and spectral emission can be approximated using the Stefan-Bolzmann Law (2) and Planks Radiation Law (3) respectively.

$$Q = \varepsilon \sigma A T^4 t \tag{2}$$

$$E(\lambda, T) = \frac{2\pi h c^2}{\lambda^5}\left(\frac{1}{e^{hc/\lambda kT} - 1}\right) \tag{3}$$

Substituting the surface temperature (T) and the surface area (A) of the sun into (2) we can calculate the total power produced by the sun as shown in Table 5 of Appendix A. Based on the average distance between the earth and the sun it is then possible to calculate the irradiance incident on the earth's atmosphere, the total power of the so called AM0 spectrum. (Refer to Section 1.3.2 for a discussion of air mass values) As shown in Table 5 the AM0 spectrum has a total power of 1370W/m^2 when it strikes the earth's atmosphere if the sun is assumed to be a perfect black body at a temperature of 5780 K.

Performing another crude calculation, this means that, given the cross sectional area of the earth, the sun continuously provides approximately 1.7x10^5 TW of power to the surface of the earth. Compare this to worldwide energy consumption from all energy sources, which is on the order of 15TW [7], and we find that in just one hour the solar energy incident on the earth is greater than the worldwide energy demand over an entire year (1.7x10^5 TWh > 365dx24h/dx15TW = 1.3 x10^{5}TWh). Harvesting and storing all of this energy is unrealistic. However, if we could capture a mere 0.01% of the solar resource continuously, this would also satisfy the worldwide energy requirement. These crude calculations demonstrate the fundamental benefits of learning how to harvest the solar resource but to understand the whole story we must determine the practical potential of the resource.

It is important to remember that the sun only shines for roughly half of the day and not equally all around the world. If we take the total normally incident AM0 insolation value that we calculated earlier (1.7x10^5 TW) and divide this by the surface area of the globe we find that on average solar radiation is a relatively low density source at just 341W/m^2 as shown in Table 5. This number might be compared to the rate at which we can extract energy from other energy sources. Consider the time it takes to extract energy from sources like coal (anthracite) at and energy density of 31.4 MJ/kg, automotive gasoline at 45.8 MJ/kg, diesel at 45.3 MJ/kg, crude oil at 41.9 MJ/kg, and dry wood at 15.5 MJ/kg [22]. It is true that a significant area is required before the solar energy flux will approach the rate at which energy can be extracted from a kilogram of gasoline. The next question is simply, "Is this a problem?".

For some applications the answer is a simple "yes". The vehicles we are accustomed to, for example, require a lot of potential energy to be stored in a small space in order to be portable. A suitable fuel source must thus be relatively high density. Hydrogen and fossil fuels or even electric batteries are examples of such sources. The electricity grid from which we all draw power to turn on our lights on the other hand does not have the same fundamental requirements as a car.

It is helpful once again to make some crude calculations to gain some perspective on just how much land is required to produce photovoltaic power. Consider for a moment how much land area would be required if the mature photovoltaic technology of today (the 20% efficient silicon panel) was installed on a large enough scale to meet to meet the worlds energy requirements 20 years from now. Assume an average daily solar resource of 5.5 equivalent peak hours of sunlight (the sunniest locations on earth average more than 7 equivalent peak hours [11]) and take into consideration that demand is expected to increase over the next 20 years. It turns out that the required area equals just a fifth of the total area of the Sahara Desert in Northern Africa. It is clear while significant on a local scale, the area requirement is really not as vast as one might think [23].

The area requirement is not really the biggest issue but rather our capacity to build enough solar panels to fill that area. Yet, this has been done before. In just under a century we have paved over an incredible amount of land area. The product may be priced higher per unit area than the roads we drive on but given a few decades this infrastructure could definitely be put in place.

It is important at this point to take a much closer look at the available solar resource. That is the resource that actually reaches the surface of the earth in locations that we can potentially access it. Understandably, the atmosphere plays a major role when trying to characterizing the available solar resource. Every type of particle and molecule in the atmosphere will interact with the light that passes through it. The various constituents of air (Nitrogen, Oxygen, Argon, Carbon Dioxide) dust particles and water vapor all have an effect on the insolation.

The influence of the atmosphere on the spectral distribution of insolation is of particular importance to PV technologies that are tailored to a specific spectrum. High efficiency triple junction cells used in CPV applications including those integrated into the SUNRISE demonstrator achieve high efficiencies because they are tailored to optimally harvest a particular spectrum. Thus the higher efficiencies are at a cost of higher dependence on a stable input spectrum.

Section 1.3.2 takes a closer look at how the influence of the atmosphere on the incident solar spectrum is described.

1.3.2 Air Mass, Spectral Variation, Standard Spectra, SMARTS2

In Section 1.2.2 the limits of single junction performance were explained using the ASTM G173 AM1.5G Standard spectrum. The need for such a standard spectrum is explained presently with a discussion of the atmospheric influence on the light that reaches the earth’s surface.

If we consider the sun a black body radiator as we did in Section 0, the solar spectrum in space (the so called extraterrestrial solar spectrum) can be predicted reasonably well. This is shown in Figure 1-12 where the black line represents the extraterrestrial spectrum and the smooth blue line represents the theoretical emission from a perfect black body radiator at 5780 K.

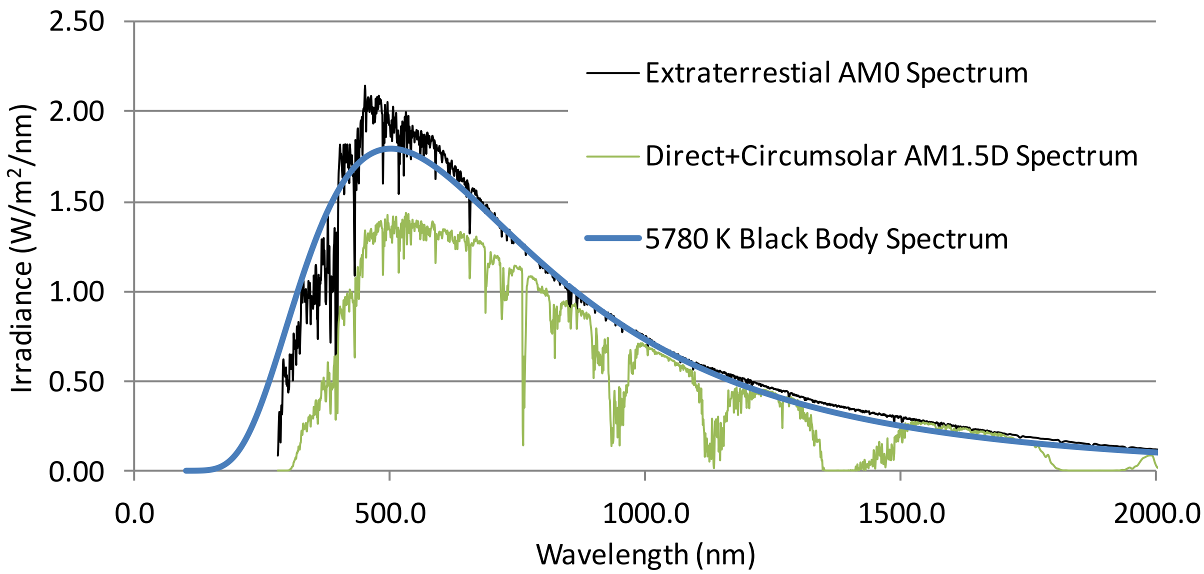

Figure 1-12: Comparison of ASTM G173 AM0 and AM1.5D spectra with a black body curve at 5780K.

For terrestrial PV applications however we must consider the influence of the atmosphere on the insolation. Despite the fact that the solar spectrum emitted from the sun is approximately the same over time, this is not what we observe on the surface of the earth. In fact, due to changes in the effective thickness of the atmosphere, there are a number of quantities that act to change the spectral distribution of the light incident on the earth's surface.

For the purposes of illustration it is convenient to first look at the air mass (AM) variation over a single day. The geometrical air mass is approximately defined as:

$$AM = \frac{1}{\cos(\theta)}, \tag{4}$$

where θ is the zenith angle or the angle between a line pointing at the sun and the normal to the earth's surface. Thus $1-\theta$ is equal to the elevation angle of the sun. At a zenith angle of zero degrees the sun is directly over head and the air mass value is 1. When the sun is on the horizon the air mass approaches infinity. This approximation of the air mass breaks down for very high AM values anyway as it assumes that the earth is flat. Regardless, for our purposes the definition above is more than sufficient.

The purpose for defining an air mass value is that it allows us to describe how much filtering the light reaching us has experienced. Since high energy photons on the blue end of the spectrum scatter with a higher probability than low energy photons when travelling through the atmosphere we see a red shift in the solar spectrum in the morning and evening when the air mass is the highest. This process is called Raleigh scattering. The effect is shown by plotting the spectral irradiance for different AM values as in Figure 1-13. These spectra were simulated using SMARTS2 which will be described later in this section.

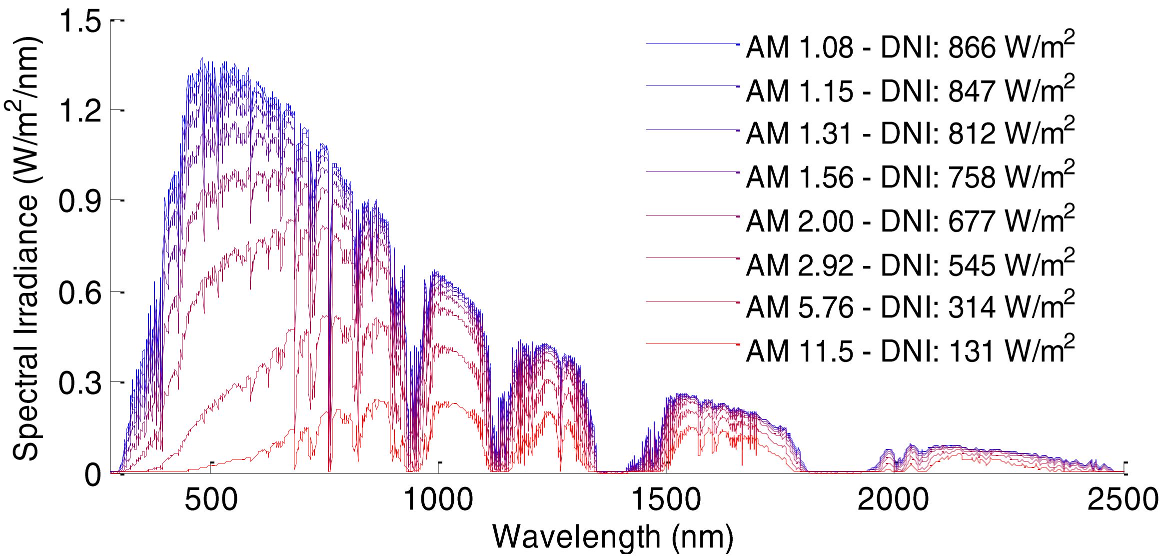

Figure 1-13: SMARTS2 simulated spectral irradiance for the range of AM values that occur on the summer solstice in Ottawa, Ontario, Canada. The AM 1.08 spectrum peaks at about 1.4 W/m^2/nm where as the AM 11.47 spectrum peaks at just over 0.2 W/m^2/nm.

The air mass thus roughly defines the solar spectrum at a given point in time in a given geographical location. With this knowledge it is thus possible to define the optimal spectrum for which to optimize a solar cell design.

In the early 1980's as the first tandem cells were developed in order to more optimally harvest the solar spectrum it became evident that some kind of a standard needed to be developed to facilitate a comparison of the state-of-the-art PV devices being developed by various teams around the world. Before this point there was not even a general consensus on the solar spectrum for which multijunction solar cells should be optimized. With the support of the industry the first standard spectra were published in 1982 by the American Society for Testing and Materials. These standard spectra were refined and revised a number of times and eventually were revised extensively upon recommendation from K. Emery, D. Myers, and S. Kurtz from NREL [24] before being republished most recently as the ASTM G-173-03 standard in 2003 [25]. The recommendation offered convincing evidence that the standard spectra should be chosen for an air mass of AM1.5 based on measurements of the cumulative annual direct-beam radiation from a number of US cities. This was based on the fact that the 50 percentile air mass occurred on average at an air mass of about 1.5 as shown in Figure 1-14.

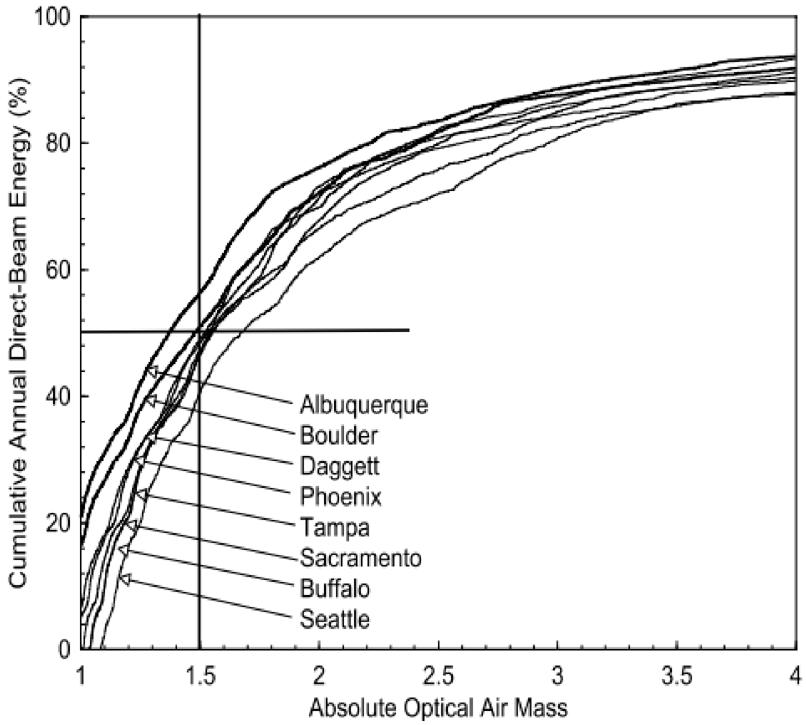

Figure 1-14: Evidence for an AM1.5 standard spectrum presented by NREL at PVSC29 in 2002. The plot shows cumulative annual direct-beam radiation for a number of US cities. The average air mass at which 50% of the radiation occurs is approximately AM1.5 [24]**.**

Within the ASTM G-173-03 standard two terrestrial solar irradiance spectra were defined. Together they define the testing standards for both the direct normal spectral irradiance and the global tilt spectral irradiance. In general the former defines the spectrum harvested by CPV systems and the later defines the spectrum harvested by flat panel systems. They are both defined on a surface of specified orientation and for a single set of atmospheric conditions that was considered a reasonable average of those measured across 48 states in the continental United States of America over a one year period [25].

The standard spectra are generated using SMARTS2 [26] and provide a single reference for measuring the performance of spectrally selective devices under various natural and artificial light sources. These standard spectra are required when measuring solar cell performance under Standard Testing Conditions which calls for a cell temperature of 25°C, 1000 W/m^2 radiant intensity and the appropriate ASTM G-173-03 standard AM1.5 spectrum.

It should be noted that while the AM1.5 spectrum is widely accepted as a standard test spectrum this does not necessarily mean that it is the best choice for which to optimize a solar cell that will be deployed with the explicit goal of converting as much energy as possible. In fact this very issue has been studied extensively [24][27].

P. Verlinden et al. have performed such measurements, shown in Figure 1-15, which show that in fact in the regions with the most direct normally incident (DNI) light, between 15 and 35 degrees latitude, the optimal air mass spectrum for which to optimize a multijunction solar cell is often lower than AM1.5. However, it is also important to remember that seasonal variations in the optimal air mass account for only 1-2% of the net system performance [27] and that there are many other factors that affect system performance more.

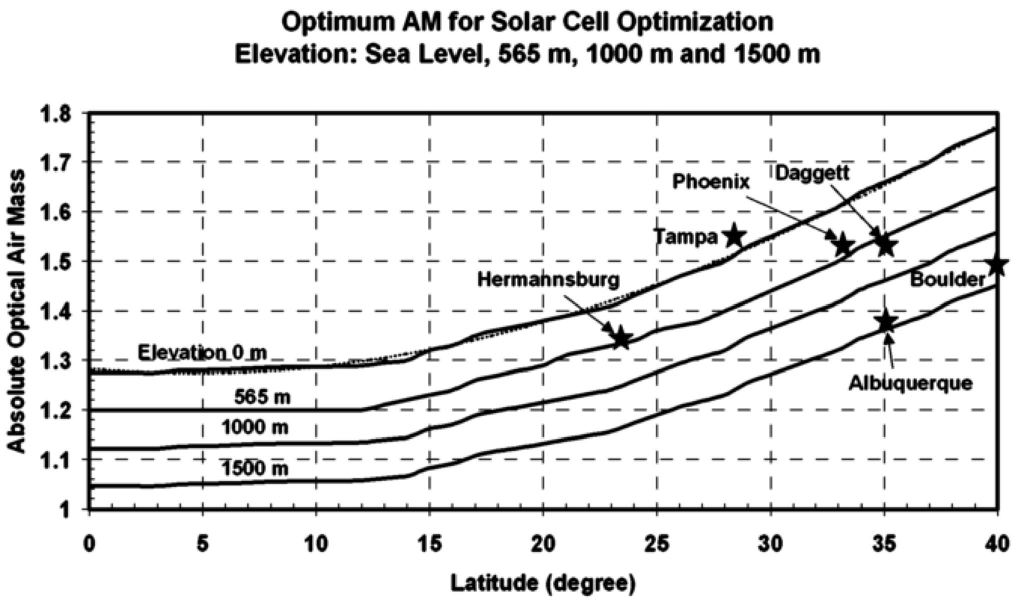

Figure 1-15: Optimum air mass versus latitude for various elevations. The bumps in the lines for each elevation are due to the addition of a weather pattern which acts to shift the optimal air mass values differently at different latitudes. Hermannsburg, Australia is compared to 5 of the US cities that were also presented in Figure 1-14. Figure prepared by Pierre Verlinden [27]**.**

It is appropriate at this point to give a brief introduction to the SMARTS2 (Simple Model of the Atmospheric Radiative Transfer of Sunshine) simulation software mentioned previously. The SMARTS2 software was developed by Christian Gueymard at the Florida Solar Energy Center and the second version was originally published in December 1995. SMARTS2 does not attempt to replace more rigorous treatments of the atmosphere's affect on sunlight. Rigorous codes such as MODTRAN are time consuming to run, take into consideration multiple atmospheric layers and rely on extremely detailed vertical profiles of atmospheric constituents. Rather, SMARTS2 aims to satisfy engineering requirements using quick and relatively simple transmittance parameterizations which has earned it universal acceptance throughout the photovoltaics industry. As mentioned above, the SMARTS software is now used to generate the ASTM G-173-03 standard spectra and is widely accepted as the standard spectral simulation software for photovoltaic applications.

Unfortunately even the success of the SMARTS2 software is limited by the accuracy of the atmospheric data that the user must gather for a particular geographical location. The input file while simple compared to more rigorous codes still requires some information about the composition of the atmosphere and due to the scarcity of such information accurate simulation results can be difficult to achieve. Thus SMARTS2 simulated spectra have been used in this work to demonstrate trends and refine the model presented in Chapter 4 but the spectral distribution of incoming light was also measured with a spectroradiometer in order to analyze the performance of the SUNRISE demonstrator.

1.3.3 Trackers, Concentrators and System Level Deployments

The number of system alternatives in the CPV industry is staggering and as such a complete review of the design solutions available [28] is not appropriate here. Nevertheless, it is illustrative to show a few of the alternatives so a select few are presented here.

At the University of Ottawa the SUNLab monitors two different tracking systems. The SUNRISE demonstrator which is the focus of this work is shown in Figure 1-16.

Figure 1-16: The SUNRISE demonstrator May 9th, 2011. The SUNRISE demonstrator holds high-efficiency quantum-dot-enhanced triple-junction solar cells designed and manufactured by Cyrium Technologies Inc. that have been integrated into OPEL Solar MK-I Fresnel-lens-based 550x concentrating modules that are pointed at the sun with an OPEL Solar dual axis tracker that is manufactured by Trackers FEiNA.

The SUNLab has also installed two demonstrators through the Advancing Photovoltaics for Economical Concentrator Systems (APECS) project. One of these trackers is shown in Figure 1-17. These demonstrator systems look quite different from the SUNRISE demonstrator. Rather than a pedestal style tracker that follows the sun like a sunflower, these trackers achieve azimuthal motion with a rotatable carousel and zenith angle adjustment via an electric piston. The optics are much different than those on the SUNRISE demonstrator as well. The Morgan Solar designed concentrating optics use light guiding techniques to concentrate light on high efficiency solar cells rather than the imaging approach achieved with Fresnel lenses on the SUNRISE demonstrator.

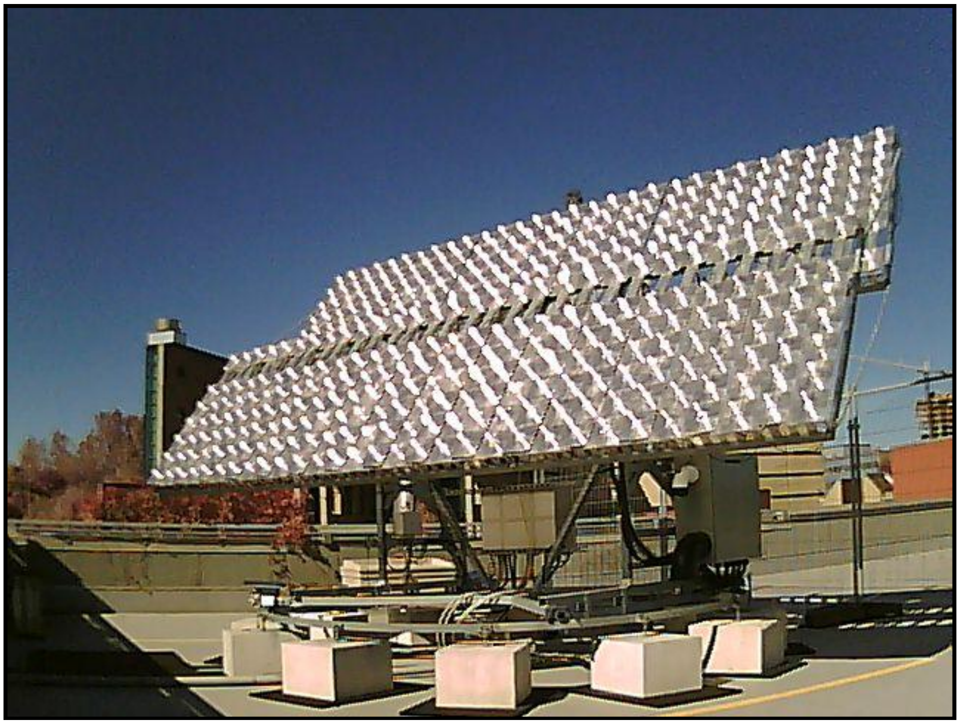

Figure 1-17: The APECS demonstrator May 9th, 2011. The APECS demonstrator holds high-efficiency triple-junction solar cells that have been integrated into Morgan Solar concentrating optics that are pointed at the sun with a Golden Sun dual axis tracker.

The two systems described thus far have used refraction and/or total internal reflection to achieve concentration. The alternative to transmission based optics is reflective optics. One demonstration of a mirror based concentrating system is that designed by Solar Systems Pty. Ltd. who have installed over 1MWp with dish concentrating systems in the Australian outback. These 130 square meter reflective dishes concentrate light onto an actively cooled high density array of high efficiency solar cells designed by Spectrolab [29]. One of these systems at the Hermannsburg Power Station is shown in Figure 1-18.

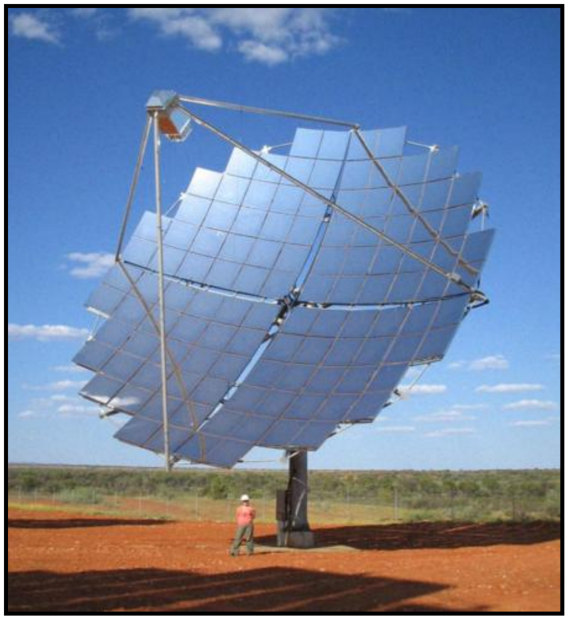

Figure 1-18: Solar Systems' 130 m^2 concentrating dish system at the Hermannsburg Power Station in the Australian outback. Insolation is reflected at 500x concentration onto a high density array of high efficiency multijunction solar cells that are actively cooled with water [29]**.**

Another example of reflective optics are those designed and manufactured by SolFocus. Figure 1-19 shows SolFocus' non-imaging, two stage reflective optics that achieve 650x concentration [30].

Figure 1-19: SolFocus two stage reflective optics. This demonstrator system was deployed in Kailua Kona at the National Energy Laboratory of Hawaii [31]**.**

Amonix has developed the highest capacity CPV system to date rated at 60kWp. The Amonix 7700 CPV solar power system is designed exclusively for utility scale applications and at 77 feet wide and 49 feet tall it is also the largest [32].

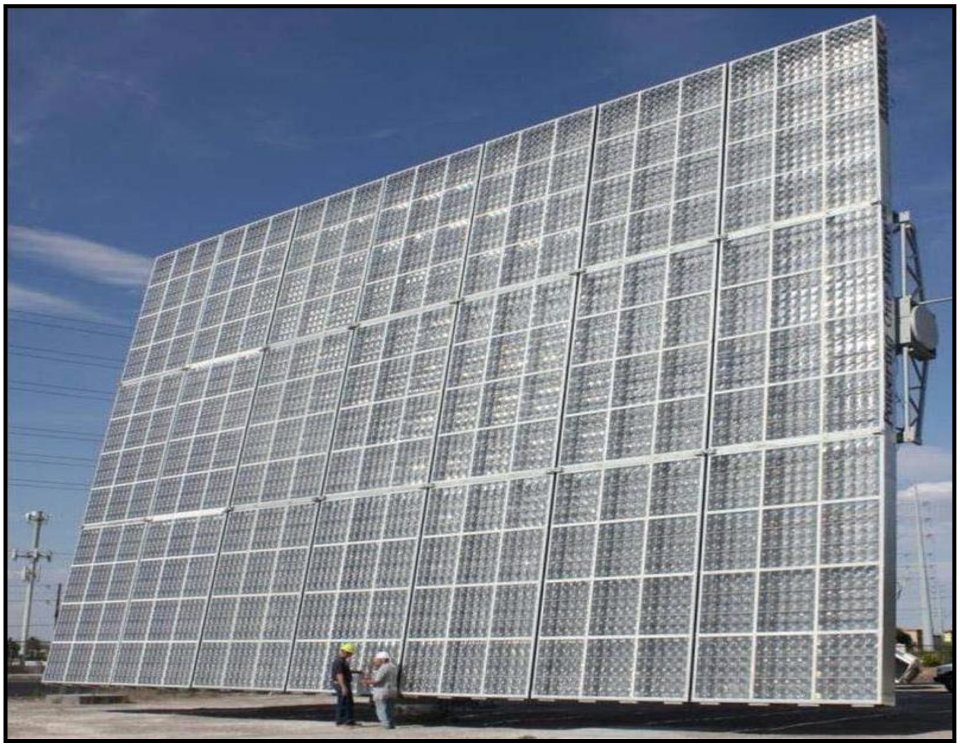

Figure 1-20: The 60kW Amonix 7700 CPV solar power system uses acrylic Fresnel lenses to concentrate at up to 500x concentration onto high efficiency triple junction cells [33] [34]**.**

Another notable CPV technology is available from Soitec. Soitec acquired Concetrix Solar in 2009 and with it the results of over 10 years of CPV development undergone at the Fraunhofer Institute in Freiburg Germany. The Concentrix technology uses a Fresnel lens to concentrate light up to 500x but with a very small lens at 4 cm by 4 cm and a very small circular metamorphic triple junction cell with a diameter on the order of 2mm. Originally the small Fresnel lens was the only concentrating optic incorporated into the Concentrix module. However, since 2008 a reflective secondary optic was added to address a number of issues [35].

The most common reasons for adding a secondary optic as a homogenizer were acknowledged, namely, to increase colour mixing and flux uniformity but these issues were not as critical for Concentrix due to their small optic. In addition Concentrix showed that it was also possible to increase the acceptance angle of their module by adding a small reflective secondary optic with a circular aperture on top of each solar cell [35]. Figure 1-21 shows modules each with 150 optics tracking the sun at a deployment in Puertollano, Spain.

Figure 1-21: A CPV power plant deployed in Puertollano, Spain by Concentrix Solar, a division of Soitech [36]**.**

Emcore is most famous in the PV community for its development of high efficiency triple junction solar cells for extraterrestrial applications. Emcore however, also leverage its expertise when it comes to high efficiency solar cell design, to build extremely competitive utility scale systems for terrestrial CPV applications. Figure 1-22 shows an example of Emcore's unique tilt and roll tracking system [37]. Emcore is also pushing the limits of concentration ratio and recognizing a movement from medium (500x) to high (1000x^{+}) concentration which offers fundamental benefits in terms of system efficiency if alignment, tracking accuracy and thermal management issues can be adequately addressed [38].

Figure 1-22: Emcore terrestrial CPV deployment with tilt and roll tracking system and silicone-on-glass lens concentrating at 1090x the intensity of the sun [37]**.**

Another unique design is that implemented by Daido Steel. Daido Steel has implemented a Japanese design in which domed Fresnel Lenses are used to minimize chromatic aberrations during concentration, increase the acceptance angle to relax tracking requirements and minimize the focal length in order to build a low profile module that is easy to transport and install. [39]

Figure 1-23: Daido Steel dome shaped Fresnel Lenses designed to minimize chromatic aberration and maintain a short focal length. Pilot plant deployed in Tokoname-city, Aichi Prefecture, Japan has been in operation since February 2009 [39]**.**

1.3.4 Thermal Management

Even at almost 45% efficiency, a triple junction solar cell must still dissipate more than 55% of incident light power as heat. An increase in cell temperature is thus unavoidable which results in changes in the behavior of the cell itself. In Section 0 we will look at the effect of increasing cell temperature on the shape of the energy band diagram and the resulting detrimental effect on cell performance but for now the thermal design considerations at the CPV system level are outlined.

In Section 1.3.3 numerous CPV systems were described which are designed to concentrate sunlight between 500 and 1000 times. At these levels of concentration thermal management is of incredible importance. The best power output temperature coefficients at the system level are on the order of 0.2 %/°C but even this adds up if passively cooled cell temperatures are at ~40°C above ambient [40]. For example, given a CPV module rated at Standard Testing Conditions (STC = 25°C) which is likely to be deployed in a climate where ambient temperatures of 40°C are not uncommon, this means the operating temperature of the solar cell could easily be 80°C. Such a cell would be operating at 55°C above the temperature at which the modules peak power was rated and would produce roughly 11% less power output than at standard testing conditions.

This 11% is quoted as an illustration only and is actually a manageable number that is taken into consideration when calculating the net present value of a CPV deployment in a particular location and climate. Nevertheless, the importance of understanding how heat is extracted from the solar cell is extremely important.

Due to the added expense of active cooling and the unpopular prospect of water usage only a very few commercial systems employ active cooling systems [29]. The remaining systems take advantage of custom heat sink designs that attempt to passively cool the cell by spreading heat to fins that are in turn cooled by the surrounding atmosphere. This strategy highlights the need for excellent thermal contact between the cell and the heatsink which must be facilitated by an electrically insulating carrier or receiver. Figure 1-24 shows an example of a receiver designed by Emcore which has performed extensive research into both the shape and material composition of its carriers in an effort to push its concentration ratio above the 1000x threshold.

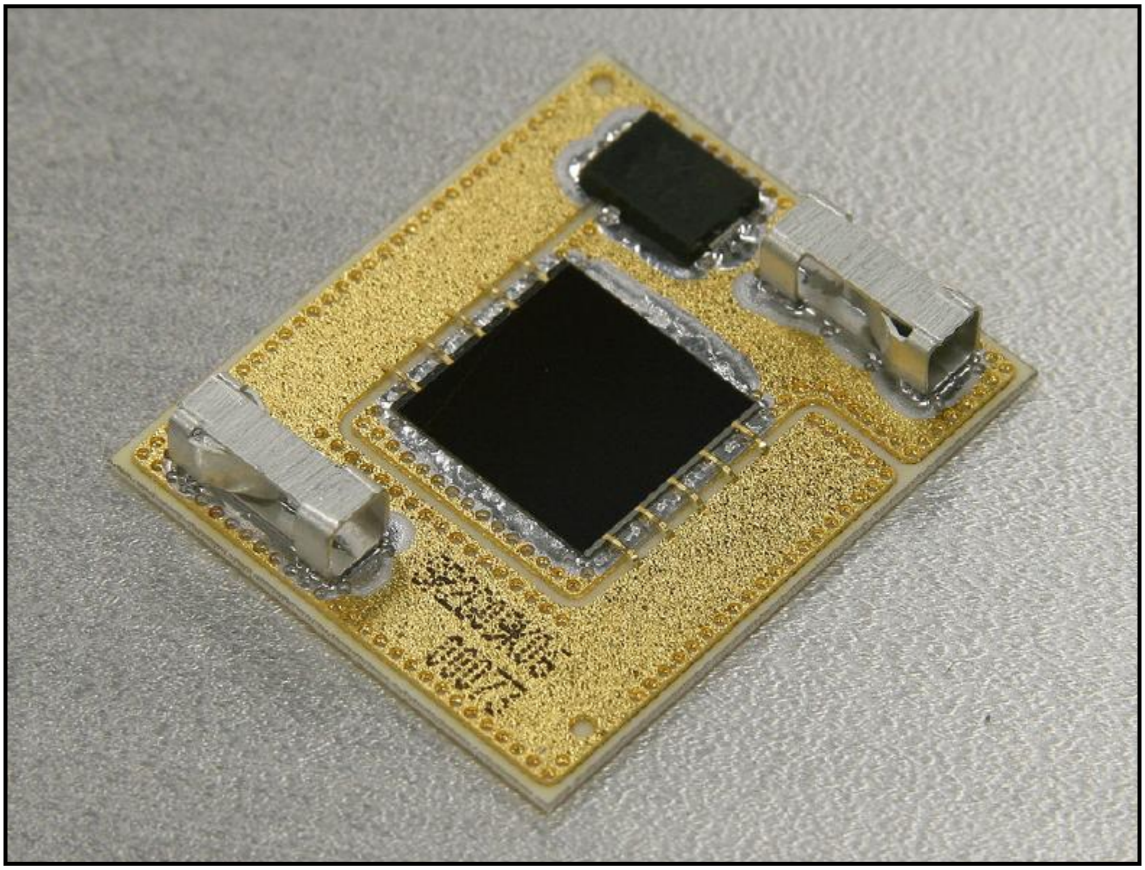

Figure 1-24: Emcores standard 1cm² receiver package including an Emcore triple junction solar cell, box connectors and a bypass diode. Receiver materials include aluminum oxide which provides sufficient stand-off voltage (>3000V) and direct bond copper which provides series resistances of less than 1mOhm sufficient for operation between 3 and 12 amps [38]**.**

The SUNLab has also performed research on carrier design in collaboration with the University of Sherbrook. [41][42] This work includes the application of metallic carriers with significantly improved thermal characteristics.

Simon Chow completed his Master's thesis on the topic in 2010 in which he analyzed the performance of chips on carrier and made recommendations as to the optimal thickness and layout of carriers much like that presented in Figure 1-24. [43]

2 Theory

This section provides the reader with the fundamental concepts required to fully appreciate the modeling and analysis presented in Chapters 3 and 4. The following concepts are described:

- The current voltage characteristic curve of a diode and a solar cell
- The single diode equivalent circuit model of a single junction solar cell
- The motivation and theoretical limits of triple junction cell performance
- The operation and corresponding band structure of a triple junction solar cell

It is extremely helpful when working with photovoltaics to have an intuitive understanding of what is going on in the device under test. Energy band diagrams are excellent tools that help us to visualize the complexities of carrier transport within devices. In this explanation we analyze simulated energy band diagrams of a generic lattice matched triple junction solar cell at equilibrium and under various bias conditions including at short circuit and at open circuit using TCAD Sentaurus optoelectronic simulation software. The effects of temperature on the energy band diagram of the solar cell are also discussed.

For more background the reader is referred to [6], [9], [44-46].

2.1 The Characteristic Current-Voltage (IV) Curve

A semiconductor based photovoltaic solar cell in its simplest form is a p-n junction with contacts on either side. It is a diode designed to allow photons to enter the device where they are absorbed, creating electron hole pairs in the process. The electrons and holes are then separated by the built in electric field present in the junction and collected as current at opposite ends of the device. This is an over simplification of a solar cell's operation but is the basis for an equivalent circuit analysis and so we start here to develop the governing equations.

The electrical characteristics of an ideal diode are governed by the equation 5,

$$I_d = I_o \left[\exp\left(\frac{qV_d}{nk_B T} \right) - 1 \right], \tag{5}$$

where I_d is the diode current, I_o is the saturation current, q is the elementary charge, V_d is the diode voltage, n is the ideality factor (n=1 is ideal diode, n>1 reflects a departure from the ideal), k_B is Boltzmann's constant and T is the temperature of the device. A schematic representation of the current-voltage (IV) curve of a diode (or a solar cell) is shown in Figure 2-1a.

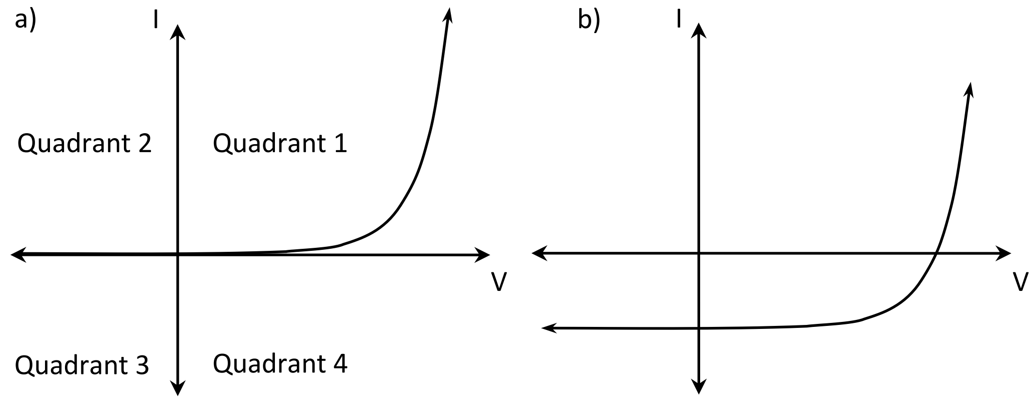

Figure 2-1: a) Schematic representation of a diode or a solar cell dark IV curve. b) IV curve when the solar cell is illuminated

When the device is illuminated as shown in Figure 2-1b, the IV curve shifts down due to the current resulting from the incident light as described at the beginning of this section. The new IV curve is a superposition of the light current produced in the cell and the original diode curve. The portion of the IV curve in the 4^{th} quadrant of the Cartesian plane in Figure 2-1b is in what is called the positive power quadrant. Operating at any point in this quadrant means that the cell is using negative power since we have a negative current at a positive voltage and electrical power consumed is equal to the current times the voltage in the same direction. This quadrant is thus the most interesting when designing solar cells and so we flip the curve as shown in Figure 2-2 to look at the power produced in the first quadrant.

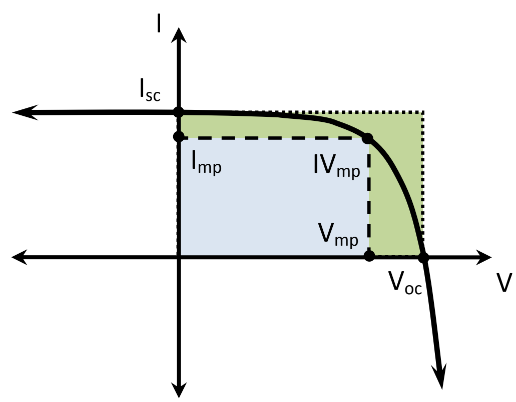

Figure 2-2: Schematic representation of a standard solar cell IV curve.

The IV curve shown in Figure 2-2 provides a lot of information about a solar cell. This is a good time to point out the various parts of the IV curve and mention certain characteristic points which will be referred to as we develop a more complete equivalent circuit model of a solar cell.

The point marked I_{sc} indicates the short circuit current of the solar cell. This is the point at which the bias voltage is set to zero volts and is the maximum light generated current the cell can produce.

The point marked V_{oc} indicates the open circuit voltage of the solar cell. This is the bias point at which no net light current is allowed to flow because, in terms of superposition, the forward biased diode current exactly equals the light generated current.

The point marked V_{mp} indicates the maximum power point on the IV curve of the solar cell.

The points marked I_{mp} and V_{mp} indicated the current and voltage at the maximum power point. The more ideal the diode behavior of the solar cell the closer I_{mp} and V_{mp} get to I_{sc} and V_{oc}. The fill factor (FF) is a ratio used to measure exactly this and is defined in equation 6,

$$FF = \frac{I_{mp}V_{mp}}{I_{sc}V_{oc}}, \tag{6}$$

as the product of I_{mp} and V_{mp} divided by the product of I_{sc} and V_{oc}. In Figure 2-2 this is the ratio of the area of the blue box with dashed lines to the area of the green box with dotted lines.

2.1.1 Equivalent Circuit Analysis

Unfortunately it is impossible to achieve ideal solar cell behavior. In reality even though materials can be grown with exceptional quality there are always recombination mechanisms and contact imperfections that must be accounted for in an equivalent circuit. These are represented by two parasitic resistances, one in series and one in parallel with an ideal diode. The equivalent circuit diagram for a solar cell is shown in Figure 2-3.

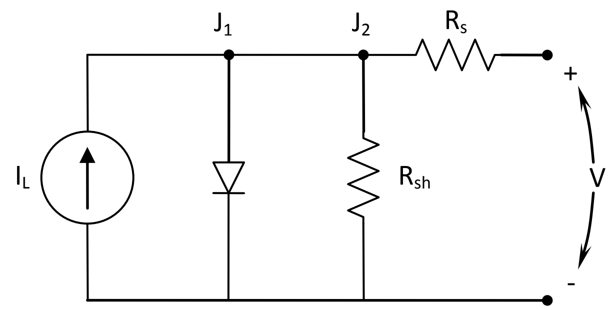

Figure 2-3: Equivalent circuit of a single junction solar cell

where I_L is the light generated current (a current source in the equivalent circuit), R_s (ideally 0 Ω) is the series resistance and R_{sh} (ideally ∞ Ω) is the shunt resistance.

Using Kirchhoff's Current Law at junctions J_1 and J_2 and Kirchhoff's Voltage Law around the three voltage loops in the circuit gives us more than enough equations to derive the characteristic single diode equivalent circuit model of a solar cell given in equation 7.

$$I = I_L - I_o\left[\exp\left(\frac{q(IR_s + V)}{nk_BT}\right) - 1\right] - \frac{IR_s + V}{R_{sh}} \tag{7}$$

2.1.2 Influence of parasitic resistances (R_s and R_{sh}) and ideality factor (n) on IV Curves

The addition of series and shunt resistances in equation 7 has a significant effect on the shape of a cells IV curve if the resistances become significant. Figure 2-4 and Figure 2-5 show the effects of series and shunt resistance respectively on the shape of the IV curve.

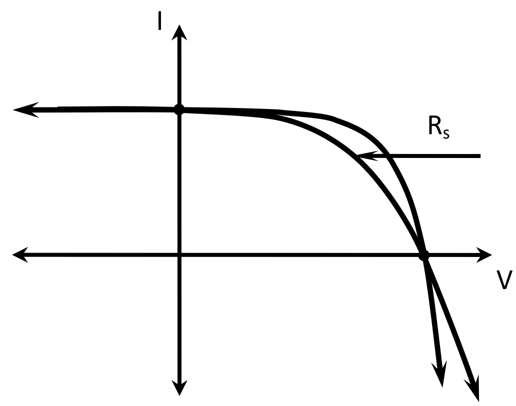

Figure 2-4: Effect of increasing series resistance on solar cell IV curve assuming that I_{sc} and V_{oc} remain the same.

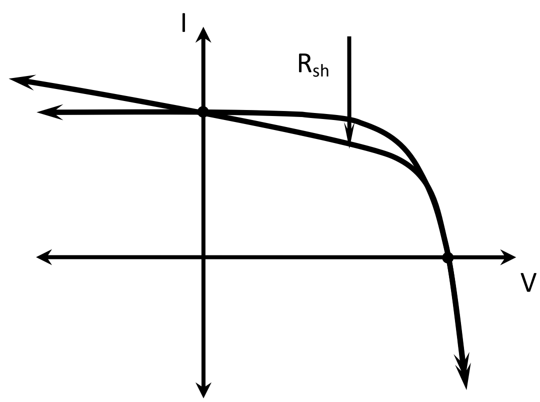

Figure 2-5: Effect of increasing shunt resistance on solar cell IV curve assuming that I_{sc} and V_{oc} remain the same.

The ideality factor is another important parameter that governs the fill factor and in turn the efficiency of a solar cell. The effect of an increasing (less ideal) ideality factor on the IV curve is shown in Figure 2-6.

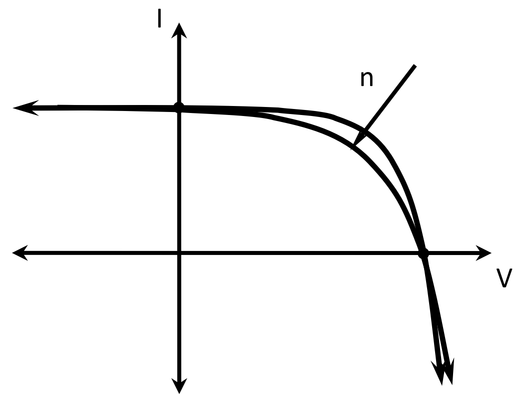

Figure 2-6: Effect of increasing ideality factor on solar cell IV curve assuming that I_{sc} and V_{oc} remain the same. The effect looks similar to that of increasing series resistance but the difference is that the curve remains an exponential rather than becoming linear for higher forward biased voltages.

2.2 The Triple Junction Cell

In this section the physics of the triple junction cell is discussed. This is thus a discussion that aims to describe what goes on once light reaches a triple junction solar cell in a CPV system. This corresponds to h_3) in Figure 1-11.

The advent of the triple junction cell meant cell efficiencies could be pushed higher than ever before towards the triple junction theoretical efficiency limit of 56% at 1000 suns [11]. This limit assumes among other things that the bandgaps of the three semiconductor materials in the cell can be tuned precisely to their optimal values (1.74 eV, 1.17 eV and 0.70eV). Unfortunately, real cell designs are limited by the availability and compatibility of materials with the necessary bandgaps. Some bandgap combinations are not easily achievable because materials exhibiting them are difficult to grow with high quality while other times it is the ability to grow two materials on top of each other that is difficult. The requirement for lattice matching between materials in adjacent subcells (necessary to achieve high quality interfaces without dislocations which act as recombination centers) is quite restrictive and has motivated engineers to find workarounds. So called metamorphic designs incorporate cleverly designed buffer layers such that materials with more ideal bandgaps can be used as adjacent cells despite having different lattice constants.

Regardless of the manufacturing approach the basic operating principles of the triple junction cell remains almost the same. Each triple junction cell incorporates three PN junctions stacked on top of each other and electrically connected in series in order to harvest the solar spectrum more efficiently. Figure 2-7a shows an updated schematic of the equivalent circuit discussed in Section 2.1.1 for a triple junction solar cell. Figure 2-7b shows a sketch of a triple junction cell with the main layers labeled.

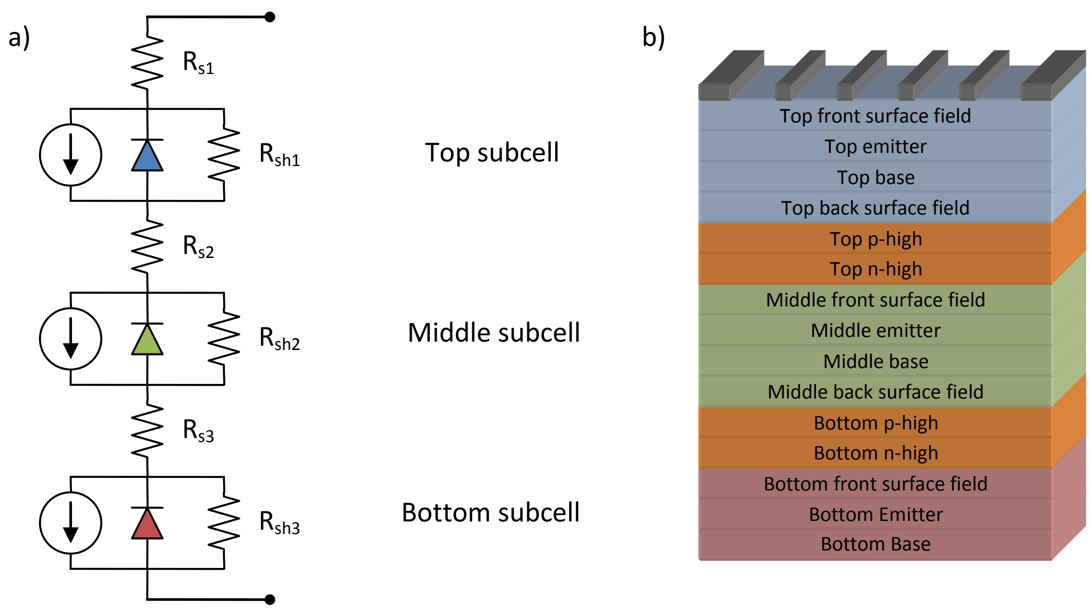

Figure 2-7: Schematic of the equivalent circuit for a triple junction cell and a corresponding cell diagram.

The basic principle is that by combining three solar cells (called subcells) each with a bandgap engineered to optimally harvest a different portion of the solar spectrum, as shown in Figure 2-8, it is possible to capture more of the energy of each incident photon as potential energy (resulting in a higher cell output voltage) rather than dissipating it as heat.

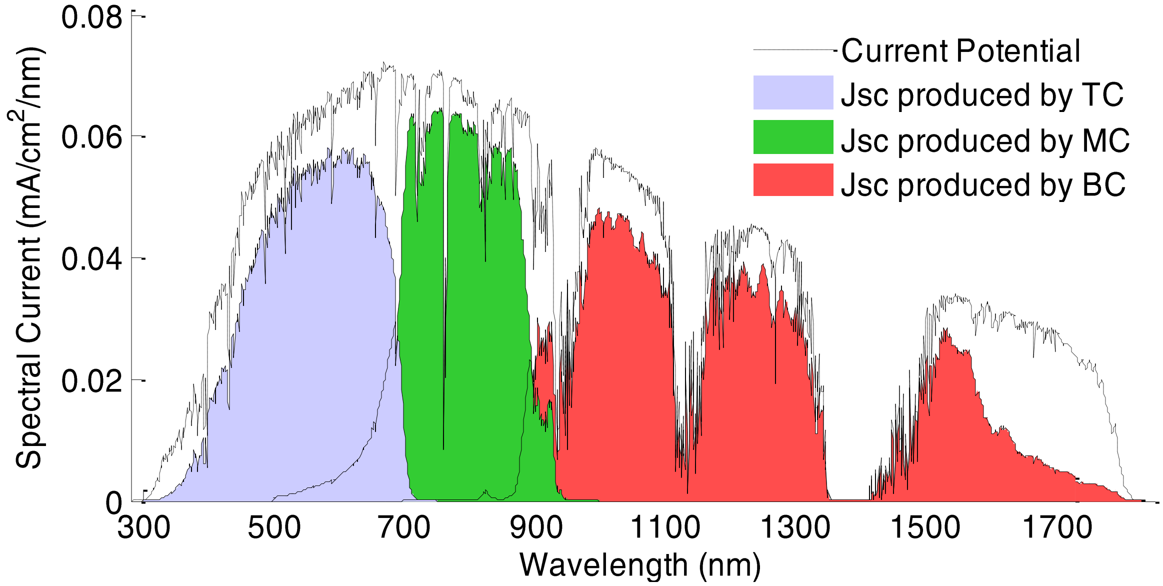

Figure 2-8: The AM1.5D standard solar spectrum (spectral current is photon flux multiplied by the elementary charge so that the area under the curve is meaningful) more optimally harvested with three junctions. This can be compared to Figure 1-4 in which the same exercise was performed for a single junction silicon solar cell. The areas integrate to give the short circuit currents of the various subcells.

The top subcell absorbs the highest energy photons but it transparent to photons with energies lower than its bandgap. These photons are thus transmitted to the middle subcell which, in a similar fashion, absorbs the photons that have energies greater than its bandgap and transmits photons with energies lower than its bandgap. The same process happens one more time in the bottom subcell. The remaining photons have energies lower that the bandgap of the bottom cell and are not harvested.

For the purposes of our band diagram analysis we will consider a lattice matched triple junction cell design that has been modeled using Synopsis TCAD software called Sentaurus, an optoelectronic modeling package. Table 1 shows the layer materials, thicknesses and doping levels of the generic design we will analyze.

Table 1: Generic design parameters of a lattice matched triple junction design. Negative doping levels represent n-type donors.

Structure	Material	Thickness (μm)	Doping (cm^{-3})	Molar Fraction (x)
Top sub-cell (GaInP)				
Top front surface field	$Al_xIn_{1-x}P$	0.03	6.00E+18	0.5
Top emitter	$Ga_xIn_{1-x}P$	0.063	8.00E+17	0.5
Top base	$Ga_xIn_{1-x}P$	0.405	-3.50E+16	0.5
Top back surface field	$Al_xIn_{1-x}P$	0.03	-1.00E+19	0.5
Top Tunnel Junction				
Top p-high TD	$Al_xGa_{1-x}As$	0.03	-1.00E+19	0.3
Top n-high TD	GaAs	0.03	1.00E+19	
Middle sub-cell (GaAs)				
Middle front surface field	$Ga_xIn_{1-x}P$	0.05	6.00E+18	0.5
Middle emitter	GaAs	0.16	1.00E+18	
Middle base	GaAs	3.5	-5.00E+16	
Mid back surface field	$Ga_xIn_{1-x}P$	0.1	-1.00E+19	0.5
Bottom Tunnel Junction				
Bottom p-high TD	$Al_xGa_{1-x}As$	0.03	-1.00E+19	0.3
Bottom n-high TD	GaAs	0.03	1.00E+19	
Bottom sub-cell (Ge)				
Bottom front surface field	GaAs	0.1	5.00E+18	
Bottom emitter	Ge	0.1	2.00E+18	
Bottom base	Ge	140	-4.00E+16	
Total		144.658		

It is extremely helpful when working with photovoltaics to have an intuitive understanding of what is going on in the device under test. Energy band diagrams are excellent tools that help us to visualize the complexities of carrier transport within devices.

In this explanation we use simulations to analyze the energy band diagrams of a generic lattice matched triple junction solar cell at equilibrium and under various bias conditions including at short circuit and at open circuit using TCAD Sentaurus optoelectronic simulation software.

The effects of temperature on the energy band diagram of the solar cell are also discussed.

2.2.1 Equilibrium

We will start by looking at the energy band diagram of the aforementioned generic triple junction cell under equilibrium conditions. This is the state of the cell when the cells top and bottom contacts are left floating and there is no light shining on the cell. A cell in equilibrium is studied by applying a detailed balance which simply states that in the dark with no applied bias every microscopic process within the cell is in perfect equilibrium with its inverse process as long as the whole cell is in thermodynamic equilibrium [47].

While this is our approach, the purpose of this report is to provide an intuitive visual understanding of a triple junction cell, so the focus will be on the implications of the theory to the band diagrams that have been simulated.

2.2.1.1 Complete Triple Junction Cell Energy Band Diagram

Figure 2-9 shows the energy band diagram of the entire cell where the vertical axis indicates the energy in electron volts and the horizontal axis is the device thickness. The top contact of the cell (from which light will enter the cell in later analysis) is at zero thickness and the bottom contact is at ~144μm but neither contact is depicted in the band diagram. In fact it is difficult to extract very much information at all from Figure 2-9 except for the enormous relative thickness of the germanium bottom layer. This is the lightly p-doped substrate on which the active layers of the cell are built. It not only acts as the base of the bottom cell from which holes are collected but it also gives the cell structural stability. The large thickness does not significantly influence the ability to collect current because the minority carrier lifetimes for electrons in p-doped Germanium are quite long leading to diffusion lengths on the order of several hundred microns [48].

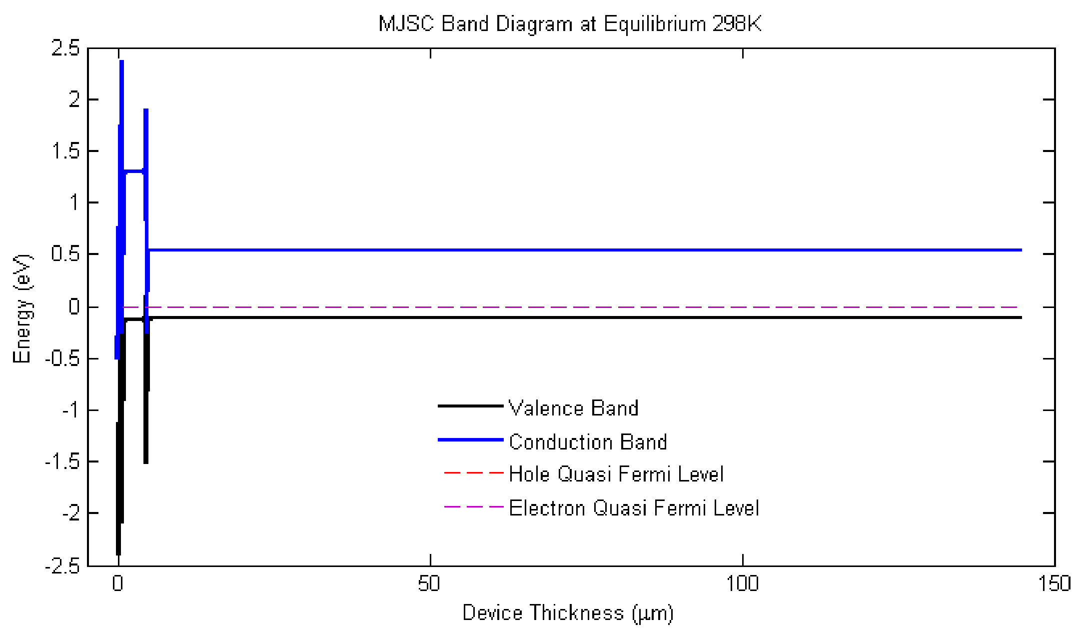

Figure 2-9: Equilibrium energy band diagram of a generic triple junction cell at 298K (25˚C)

2.2.1.2 Band Diagram of Top and Middle Subcells

Figure 2-10 shows more clearly how bands of adjacent subcells align when they are grown on top of each other. We know immediately that the cell is at equilibrium because the hole and electron Fermi levels are flat at 0eV and fall directly on top of one another. We will take a close look at how the Fermi levels shift under various biasing conditions in a later section but first we will take the opportunity to identify the various components of the cell.

The highlighted portions of Figure 2-10 and Figure 2-11 correspond to the colours in Figure 2-7. The areas highlighted in blue, green and red are the top, middle and bottom subcells respectively. The portions that are not highlighted in Figure 2-10 include the front and back surface fields (window layers) and the two tunnel junctions. Figure 2-11 shows a close up view of the top subcell and the top tunnel junction.

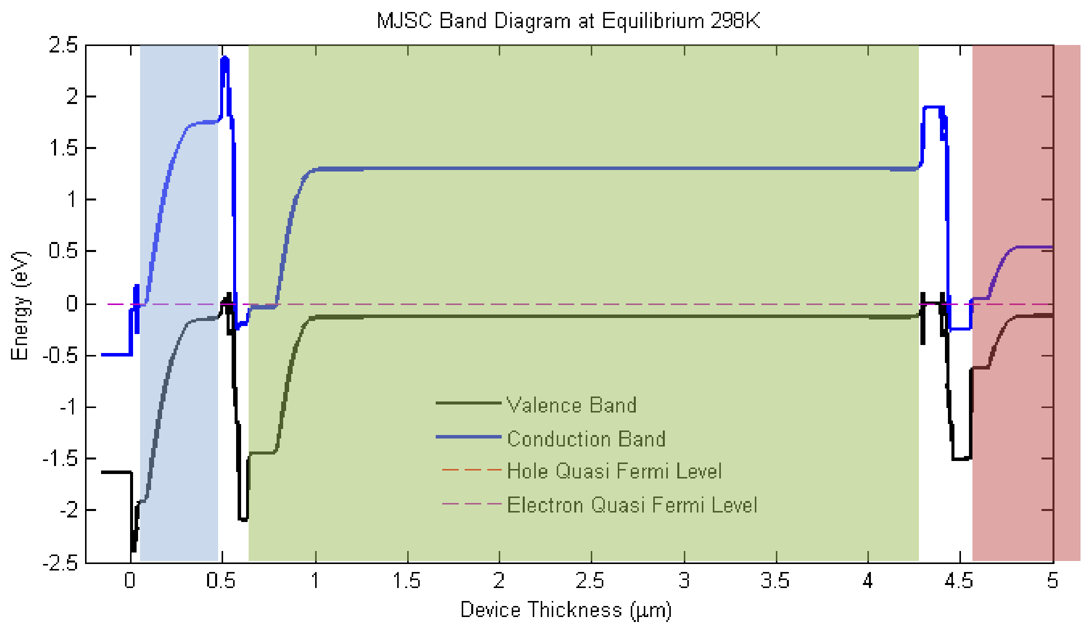

Figure 2-10: Equilibrium energy band diagram of the first 5 microns of a generic triple junction cell at 298K (25˚C). Only the top and middle junctions are completely shown.

It is also interesting to note in Figure 2-10 the thickness of the subcells and the positions of the junctions in each subcell. At ~4 µm the GaAs subcell is designed to absorb more than 95% of the incident photons at all energies above its bandgap energy. It is clear in the figure, though, that the p-type base is thicker than the n-type emitter. This is true for the top and bottom subcells as well. As mentioned previously in reference to the germanium subcell, this is because the minority carrier lifetimes of electrons in the p-type bases are longer than the hole life times in the n-type emitters. Thus, in the emitter, it is advantageous to reduce the distance holes have to travel to reach the junction at the expense of increasing the distance that electrons have to travel in the base.

2.2.1.3 Top Subcell, Window Layers and Tunnel Junctions

The areas in Figure 2-11 that are highlighted in purple are the front and back surface fields (also called window layers) of the top junction and the front surface field of the middle subcell. The purpose of the front and back surface fields is to impose a potential barrier to minority carriers on the upstream side of the junction so that they do not diffuse away from the junction and recombine before they have a chance to feel the electric field created by the junction’s built in potential.

Between the back window layer of the top subcell and the front window layer of the middle subcell we find the top tunnel junction. Tunnel junctions are a key part of the device design because they allow the three subcells to be connected to each other with almost no resistance to current flow between them. The detailed analysis of tunnel junction operation is beyond the scope of this report but an understanding of the basic concept is necessary and so it is presented below.

The goal is to connect the p-type base of the top and middle cells to the n-type emitter of the middle and bottom cells respectively with as little resistance as possible. The question is how to do this when a reversed biased junction is inherently necessary between cells. The solution is to make the junction narrow enough and steep enough that there will be a high probability of quantum mechanical tunneling of majority carriers between the valence band of the cell above and the conduction band of the cell below. The tunnel junction must also be optically transparent to photons that have not been absorbed by the subcell(s) above it. The top tunnel junction is highlighted in orange in Figure 2-11.

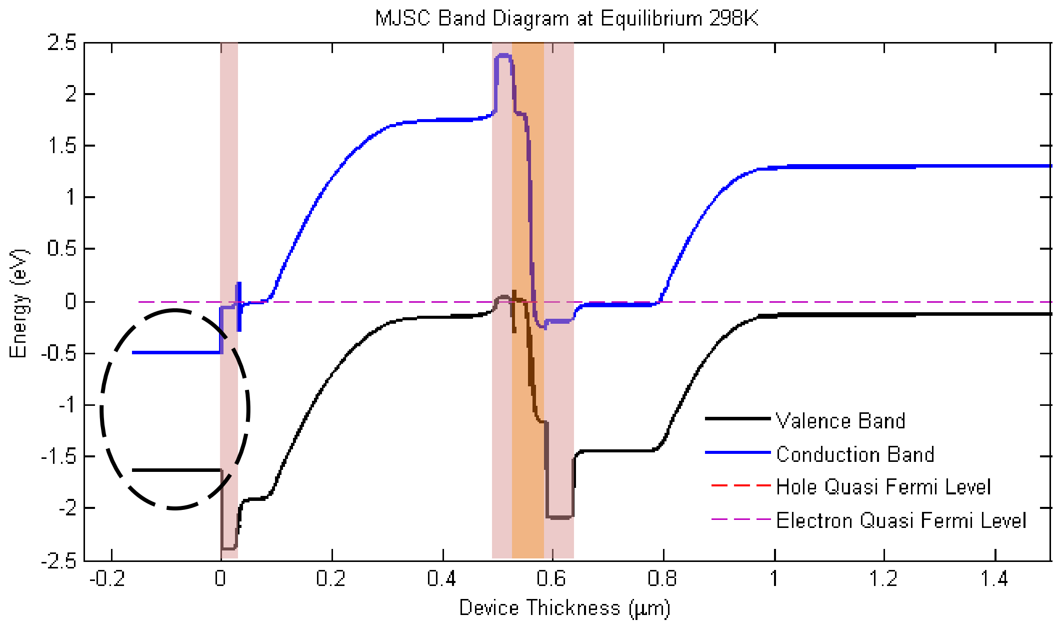

Figure 2-11: Equilibrium energy band diagram of the first 1.5 microns of a generic triple junction cell at 298K (25˚C). Only the top junction is completely shown.

The dashed circle in Figure 2-11 shows a conduction and valence band above the top contact. This is an artifact of the simulation that occurs because energy band properties of the antireflection coating material are not used in the simulation and thus are not specified. This difference between the bands in the figure is the default bandgap that Sentaurus assumes (Silicon's bandgap ~1.1eV) if no such material properties are specified. This has no influence on the rest of the simulation optically because only the index of refraction and the extinction coefficient are used to determine the transmission of the anti reflection coating. There is also no influence on the electrical calculations because carriers are collected at the top contact (at 0 μm) below the antireflection coating.

2.2.2 Open Circuit Voltage

The next step in our analysis is to shine light on the cell that we just looked at in equilibrium. If the top and bottom contacts of the triple junction cell are left disconnected we achieve an illuminated cell at open circuit voltage. A simulation was performed for an incident intensity of 1000 W/m^2, or approximately 1 sun, on the cell. Figure 2-12 and Figure 2-13 show the revised energy band diagram for the illuminated cell at open circuit voltage with the same axis as the band diagrams shown previously at equilibrium. For this analysis we will assume low level injection of minority carriers, which is reasonable for concentration levels up to more than 1000 suns. Under low level injection the minority carrier quasi-Fermi levels are non-degenerate. The same cannot be said for the majority carrier quasi-Fermi levels. This will be important in later.

As light is shone on the solar cell, electron hole pairs are created in each subcell thereby increasing the concentration of carriers. The increase in the number of majority carriers is negligible under low level injection compared to the number of majority carriers that existed at equilibrium (which is approximately the doping concentration) so the majority carrier quasi-Fermi levels do not change very much. However, the minority carrier concentrations increase dramatically with respect to their equilibrium values, which causes the minority carrier quasi-Fermi levels to split away from the majority carrier quasi-Fermi levels on both sides of each subcell junction. As more and more electron hole pairs are created, the minority carrier concentrations continue to rise and the quasi-Fermi levels continue to separate. The increase in minority carrier concentrations on both sides of the junction means that the carrier concentration gradients across the junction are reduced. A reduction in carrier concentration gradients means a reduction in diffusion currents, which induced the built in potential at the junction in the first place. The result is less charge build up and a smaller built in potential across the junction. Once again, no net current flows through the junction, and steady state has been reached.

It is interesting to point out that because the minority carrier Fermi level is set by the concentration of minority carriers under low level injection, the quasi-Fermi levels will always be set relative to the band edge in which the minority carriers exist, regardless of the size of the bandgap. Hence, if the junctions are current matched, (same number of electron hole pairs generated in each subcell) then the electron quasi-Fermi levels will be nearly the same distance from the conduction band in all three materials (with small corrections for varying density of states). The result is that a PN junction made of a material with a larger bandgap will see more band splitting given the same injection of minority carriers as a junction with a smaller bandgap. The arrows in Figure 2-12 indicate the position of the electron quasi-Fermi level relative to the conduction band on the p-side of each of the subcells.

In addition, Figure 2-13 shows that the hole quasi-Fermi level of the top cell and the electron quasi-Fermi level of the middle cell align at the same energy at the tunnel junction. These effects are precisely why it is advantageous to harvest each part of the solar spectrum with as large a bandgap as possible. It is because the sum of the differences between electron and hole quasi-Fermi levels (F_n and F_p respectively) in each of the three junctions gives the cells open circuit voltage as shown in equation 8,

$$qV_{oc} = \Delta F_{Top} + \Delta F_{Mid} + \Delta F_{Bot} = \left(F_{nTop} - F_{pTop}\right) + \left(F_{nMid} - F_{pMid}\right) + \left(F_{nBot} - F_{pBot}\right), \tag{8}$$

where the ΔF 's are the separations of the electron and hole quasi-Fermi levels in the non degenerate regions of each subcell. i.e. In the base where the doping levels are lower. An interesting subtlety in Figure 2-12 is that the position of the electron quasi-Fermi Level in the germanium bottom cell is not quite the same distance from the conduction band as it is in the top and middle cells. This is due to the fact that the three cells are not perfectly current matched but rather the small bandgap of the Germanium cell results in more photo-generation (higher injection) than in the top and middle cell. Higher injection means higher minority carrier concentration which is reflected by a higher electron quasi-Fermi level.

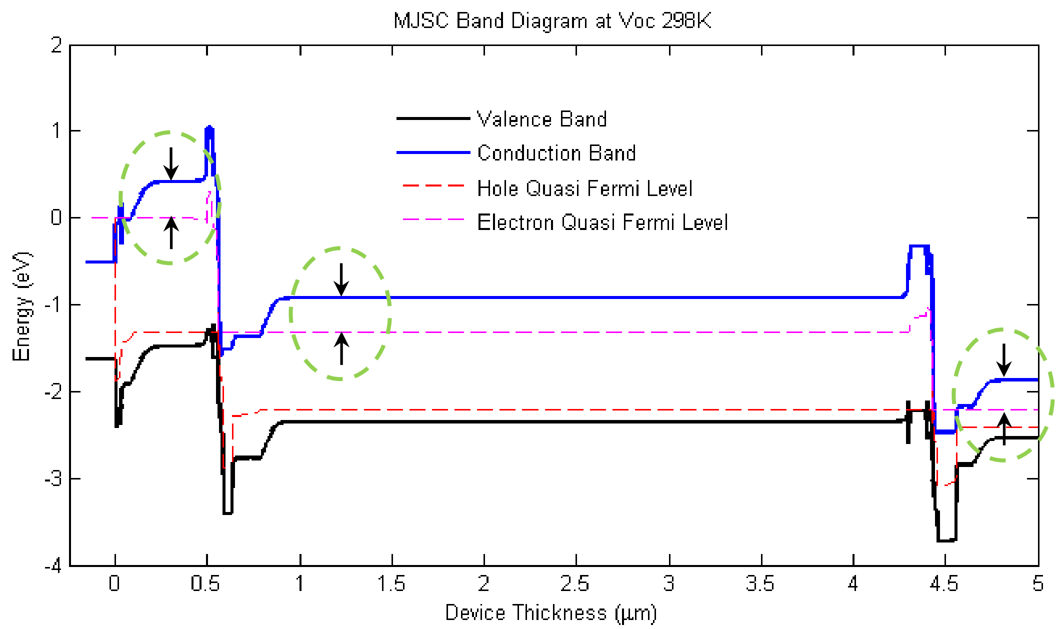

Figure 2-12: Energy band diagram of the first 5 microns of a generic triple junction cell at open circuit voltage at 298K (25˚C). Only the top and middle junctions are completely shown.

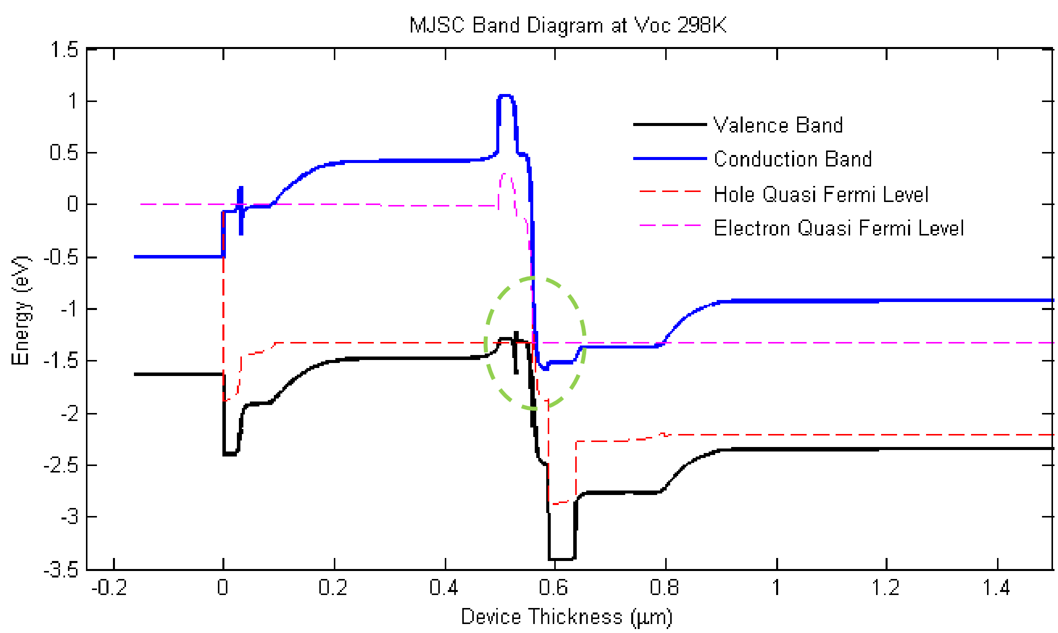

Figure 2-13: Energy band diagram of the first 1.5 microns of a generic triple junction cell at open circuit voltage at 298K (25˚C). Only the top junction is completely shown. Circle highlights the fact that electron and hole quasi-Fermi levels are aligned at the junction.

2.2.2.1 Solar Cell Efficiency: The Shockley – Queisser Limit

The fundamental increase in cell efficiency due to increasing concentration is a result of the fact that increasing the concentration of light increases the concentration of minority carriers in the solar cell shifting the quasi-Fermi levels closer to the band edges and increasing the output voltage. Thus, increasing the concentration helps the device approach the detailed balance efficiency limit.

The detailed balance limit, also referred to as the Shockley-Queisser limit, is a thermodynamic limit that assumes an external quantum efficiency of unity (perfect absorption and only radiative recombination potentially leading to reabsorption, now known as photon recycling) and normal incidence [49]. This limit is in practice difficult to achieve because it requires a device to have a perfect external fluorescence yield [49]. The external fluorescence yield is simply a gauge by which to measure how effectively photons are preserved in a device. Poor material quality, high fractions of nonradiative recombination and poor quality back reflectors will all act to reduce the external fluorescence yield.

A fluorescence yield of 100% means that, under open circuit conditions, for every photon with energy greater than the bandgap incident on the cell, a photon of the bandgap energy is eventually extracted from the front surface of the cell. This is a demanding requirement due to the narrow cone through which photons in the semiconductor can escape due to the prevalence of total internal reflection. A photon's escape requires many attempts and hence many absorption and radiative recombination cycles (photon recycling) to occur before the photon is extracted [49].

GaAs is an example of a direct bandgap material that can be grown with sufficient quality that its internal fluorescence approaches unity, however silicon has an indirect bandgap and an internal fluorescence yield of only about 20% which means it will never be able to reach the Shockely-Queisser limit [49].

The effect of an increased internal fluorescence yield is both an increase in the number of carriers collected (increased J_{sc}) and also an increase in the minority carrier concentration at a given illumination level (increased V_{oc}). The resulting increase in efficiency is for exactly the same reasons that an increase in efficiency is observed for increasing concentration. In the later case J_{sc} scales nearly proportionally to the photon flux but there is also an increase in the minority carrier concentration owing to the increased photon flux. This causes a simultaneous increase in the open circuit voltage resulting in a net increase in efficiency.

2.2.2.2 Efficiency Increase Due to Concentration

This increase in efficiency in a triple junction cell can be explained from an analysis of the quasi-Fermi levels and equation 8. The effect of increasing irradiance on the band diagram of a *pn*-junction is illustrated in Figure 2-14. If we once again assume low level injection of minority carriers, which is reasonable for concentration levels up to more than 1000suns, the minority carrier quasi-Fermi levels are non-degenerate and can be expressed as the natural logarithm of the minority carrier concentration as shown in equation 9 [50]. This calculation of the quasi-Fermi level is only valid for the minority carriers in the subcells and not necessarily for the majority carriers in the subcells or for any carriers in the tunnel junctions which exhibit degeneracy. The quasi-Fermi levels are thus given by,

$$F_n = E_i + kT\ln\left(\frac{n}{n_i}\right), \tag{9a}$$

$$\text{and } F_p = E_i - kT\ln\left(\frac{p}{n_i}\right), \tag{9b}$$

where F_n and F_p are the electron and hole minority carrier quasi-Fermi levels, E_i is the intrinsic Fermi level, k is the Boltzmann constant, T is the temperature, n is the electron minority carrier concentration, p is the hole minority carrier concentration and n_i is the intrinsic carrier concentration. The minority carrier concentration scales directly with the injection level, (i.e. the incident photon flux) so it can be shown that the change in minority carrier quasi-Fermi level in each subcell is dependent on the natural logarithm of the relative change in minority carrier concentration. The change in minority carrier quasi-Fermi levels is calculated in equation 10 for electrons,

$$\Delta F_n = F_{n2} - F_{n1} = kT\left[\ln\left(\frac{n_2}{n_i}\right) - \ln\left(\frac{n_1}{n_i}\right)\right] = kT\ln\left(\frac{n_2}{n_1}\right), \tag{10}$$

where ΔF_n is the change in electron minority carrier quasi-Fermi level and the subscripts 1 and 2 indicate two different levels of incident power as illustrated in the two cases presented in Figure 2-14. As shown in the figure, assume the second case is for increased incident power. We would like to determine the change in the separation between the electron and hole quasi-Fermi levels resulting from the added photon flux in case #2. Since the majority carrier quasi-Fermi levels do not change significantly under low level injection, the separation of the quasi-Fermi levels is nearly equal to the change in the minority carrier quasi-Fermi level. On the p-side of the junction,

$$\Delta F_p = F_{p2} - F_{p1} \approx 0 \text{, so}$$

$$(F_{n2} - F_{p2}) - (F_{n1} - F_{p1}) = F_{n2} - F_{n1} = \Delta F_n \tag{11a}$$

and on the n-side of the junction,

$$\Delta F_n = F_{n2} - F_{n1} \approx 0 \text{, so}$$

$$(F_{n2} - F_{p2}) - (F_{n1} - F_{p1}) = F_{p2} - F_{p1} = \Delta F_p \tag{11b}$$

To get a feel for the change in open circuit voltage with concentration we can assume that the change in the minority carrier quasi-Fermi level ΔF_n on the p-side is approximately the same as the change in the minority carrier quasi-Fermi level ΔF_p on the n-side for low level injection since holes and electrons are created by the same incident photons which means their concentrations increase and decrease at the same rate. It should be noted that the quasi-Fermi level separation on either side of the junction is only the same if the concentration of acceptors on the p-side is equal to the concentration of donors on the n-side. This is the assumption made in Figure 2-14 which we can tell by the fact that the majority carrier quasi-Fermi level on the p-side is the same distance from the valance band as the majority carrier quasi-Fermi level on the n-side is from the conduction band and by the fact that the junction is symmetrical.

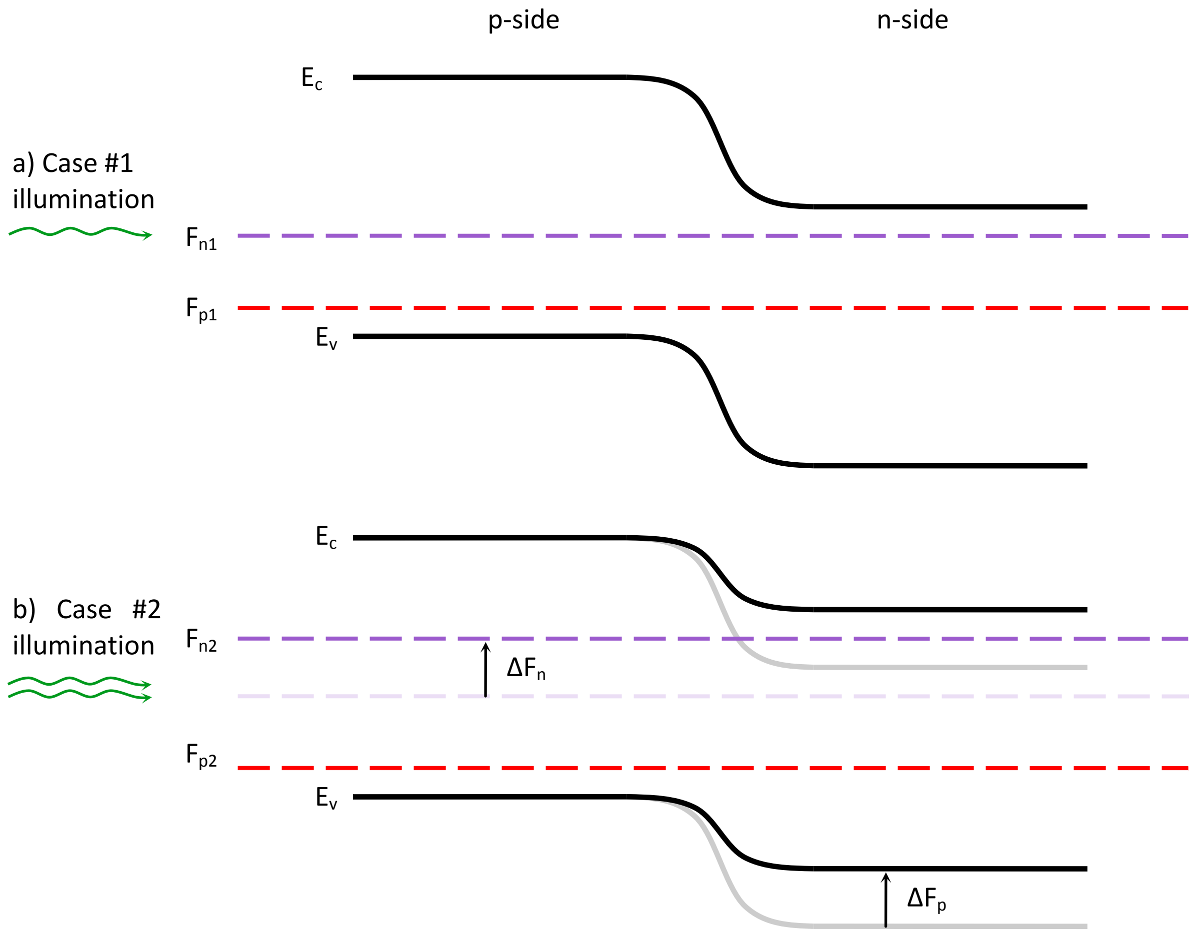

Figure 2-14: Schematic representation of a pn-junction band diagram under open circuit conditions before and after an increase in the incident intensity. a) Case #1 – lower intensity illumination and b) Case #2 – higher intensity illumination.

To find an expression for the open circuit voltage for Case #2 we can simply rewrite equation 8 which gives,

$$qV_{oc2} = \left(F_{nTop2} - F_{pTop2}\right) + \left(F_{nMid2} - F_{pMid2}\right) + \left(F_{nBot2} - F_{pBot2}\right), \tag{8}$$

and then substituting equation 11 into equation 8 we get,

$$qV_{oc2} = \left(F_{nTop1} - F_{pTop1}\right) + \Delta F_n + \left(F_{nMid1} - F_{pMid1}\right) + \Delta F_n + \left(F_{nBot1} - F_{pBot1}\right) + \Delta F_n,$$

which reduces to equation 12 below. This once again assumes that the changes in the quasi-Fermi level separations on both sides of each subcell are equal to the change in the electron minority carrier quasi-Fermi level. Equation 12 shows the increase in open circuit voltage resulting from the same effect in all three subcells. It assumes that the spectrum stays the same as concentration increases and that the density of states in the conduction and valence bands are the same in all three subcells. This is not true if the subcells are made of different materials but the approximation is reasonable because the effect of the density of states is not very significant under low level injection.

$$V_{oc2} = V_{oc1}(T) + \frac{3\Delta F_n}{q} = V_{oc1}(T) + 3\frac{nkT}{q}\ln\left(\frac{n_2}{n_1}\right) \quad (12)$$

Thus the open circuit voltage increases as the natural logarithm of the relative increase in incident photon flux. i.e. the concentration level. Another interesting point is the factor of 3 in the second term of equation 12 which stems from the fact that we are analyzing 3 cells rather than 1. This factor is not present in a similar analysis of a single junction cell as shown below in equation 13 which assumes parasitic resistances are negligible and that $I_{sc}/I_o >> 1$ is from [46]:

$$V_{oc1sun} = \frac{nkT}{q}\ln\left(\frac{I_{sc1sun}}{I_o}\right), \quad (13)$$

and if we continue with the derivation for a concentration of X suns we get,

$$V_{ocXsuns} = \frac{nkT}{q}\ln\left(\frac{I_{scXsuns}}{I_o}\right) = V_{oc1sun}(T) + \frac{nkT}{q}\ln\left(\frac{I_{scXsuns}}{I_{sc1sun}}\right) = V_{oc1sun}(T) + \frac{nkT}{q}\ln(X), \quad (14)$$

where $V_{ocXsuns}(T)$ is the open circuit voltage at temperature, T, at a concentration of X times the initial intensity which in this case we have set arbitrarily to one sun. The resulting efficiency gain can be calculated from the $V_{ocXsuns}$ determined above using a fill factor (FF) and the current and voltage at the maximum power (MP) point. The efficiency is defined as follows:

$$\eta = \frac{P_{MP}}{P_L}, \quad (15)$$

where P_L is the incident light power and P_{MP} is the power at the maximum power point which is given by equation 16,

$$P_{MP} = FF \times V_{oc} \times I_{sc}. \quad (16)$$

Substituting equation 16 into equation 15 we get the following at one sun:

$$\eta_{1sun} = \frac{FF_{oc1sun} \times V_{oc1sun} \times I_{sc1sun}}{P_{L1sun}}, \quad (17)$$

and at a concentration level of X suns,

$$\eta_{Xsuns} = \frac{FF_{ocXsun} \times V_{ocXsun} \times X \cdot I_{sc1sun}}{X \cdot P_{L1sun}}, \quad (18)$$

and taking the ratio of the efficiencies 17 and 18 and substituting 12 we find,

$$\frac{\eta_{Xsuns}}{\eta_{1sun}} = \left(\frac{FF_{Xsun}}{FF_{1sun}}\right)\left(1+\frac{\frac{3nkT}{q}\ln(X)}{V_{oc1sun}}\right), \tag{19}$$

If the spectral content of incident light stays the same, there are no parasitic resistances in any of the subcells, and the recombination mechanisms stay the same over concentration then the fill factor will remain constant and the ratio of the fill factors will equal unity. In reality the dominant recombination mechanisms change with concentration level and temperature and so the ratio of the fill factors is not a constant. Equation 19 shows explicitly how the efficiency increases with concentration but groups a number of subtle effects into the ratio of the fill factors. This fundamental increase in efficiency is built into the model presented in Chapter 4 but will not be covered in detail at that time. The effects of changing fill factor are taken into consideration when dealing with the equivalent circuit model by specifying a recombination current in addition to a saturation current resulting in a two diode model of each subcel as discussed further.

2.2.3 Effect of Temperature on Open Circuit Voltage

It is easiest to discuss the effects of temperature while considering open circuit conditions so the open circuit energy band diagrams from the last section have been re-simulated and presented again in Figure 2-15 for 350K (77˚C). Returning to the discussion about the splitting of the Fermi levels, we find that temperature has an effect on how much splitting takes place, which is reflected in the open circuit voltage calculation through equation 8.

Recall that as light is shone on the device, the minority carrier concentrations increase immediately resulting in a reduction in the concentration gradient across the junction. The diffusion current decreases proportionally and the potential barrier reflects the reduced charge build up across the junction. The diffusion current, however, is also dependent on temperature. The higher the junction temperature, the easier it is for majority carriers to overcome the built in potential and diffuse across it. Thus, increasing temperature increases the diffusion current which increases the built in potential. This results in an increased drift current, which reduces the minority carrier concentrations and limits the quasi-Fermi level splitting.

Increasing the temperature also has an effect on the Fermi-Dirac distribution increasing the length of the tails to reflect an increase in intrinsic carrier concentration with temperature. This also acts to limit the Fermi level splitting but not significantly unless the increased temperature causes the intrinsic carrier concentration to approach the minority carrier concentration due to illumination.

The separation between the electron quasi-Fermi level and the conduction band is clearly greater at 350K than at 298K. This difference is evident when comparing to Figure 2-12. A scale inset of the middle subcell band diagram of Figure 2-12 is included in Figure 2-15 to facilitate this comparison. A noticeable amount of band narrowing due to temperature is also evident from the scale inset. This effect is a fundamental property of semiconductor materials that results from changes in the semiconductor lattice over temperature and is described by the Varshni Model [51]. Band narrowing is an effect that must be taken into consideration when optimizing the bandgap combination in a triple junction cell for maximum energy production over a year [52].

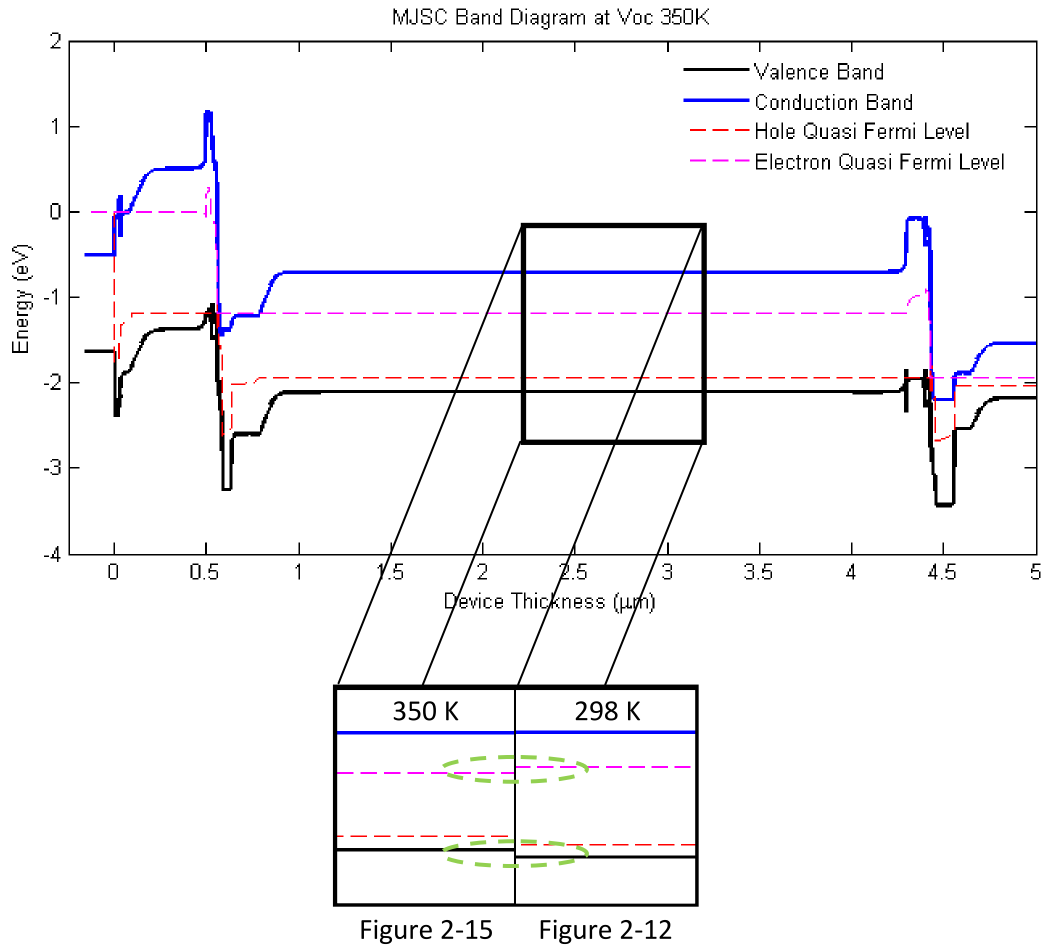

Figure 2-15: Energy band diagram of the first 5 microns of a generic triple junction cell at open circuit voltage at 350K (77˚C). Only the top and middle junctions are completely shown. The upper dashed oval in the energy band diagram comparison between Figure 2-15 and Figure 2-12 (the same cell at 298 K) highlights the increase in the separation between the electron quasi-Fermi level and the conduction band edge compared to the simulation at 350 K. Band narrowing in the simulation at 350 K is also evident when comparing the bandgap at 350 K to the bandgap in the original simulation at 298 K.

2.2.4 Short Circuit Current

Next we look at the energy band diagram under short circuit conditions. To achieve this one would connect the top and bottom contacts in the previous open circuit voltage case while maintaining the same level of illumination.

In this case, the quasi-Fermi levels are pinned at either side of the energy band diagram at zero Volts. The hole and electron quasi-Fermi levels still align in the tunnel junction as before. The biggest difference in this case is the fact that there are significant gradients in the quasi-Fermi levels at the junctions which indicates that current is flowing in the device. The effect of pinning the Fermi levels on either side of the band diagram is that the junctions are stretched and the quasi-Fermi levels exhibit corresponding slopes.

As the forward bias on the cell is reduced from Voc towards 0 V, majority carriers are extracted at the contacts. Much like reverse biasing a diode, this results in a wider depletion region in the subcells. The increased width of the depletion region means a higher potential difference across the junction.

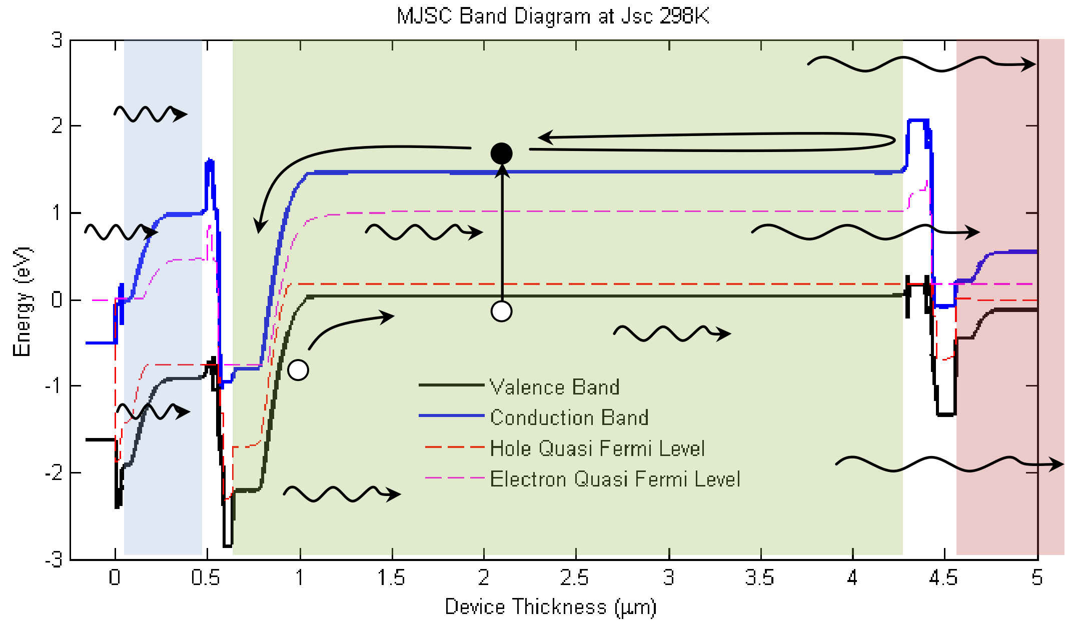

Figure 2-16: Energy band diagram of the first 5 microns of a generic triple junction cell under short circuit conditions at 298K (25˚C). Only the top and middle junctions are completely shown.

Now that we are finally looking at a case in which current is flowing, a quick review of the photovoltaic process is appropriate. Consider the middle subcell highlighted in green in Figure 2-16. Squiggly lines represent incoming photons that are being absorbed by the solar cell at various depths depending on their energy. When a photon is absorbed in the middle junction, as shown in the figure, an electron hole pair is created. An electron is represented by a black filled circle and a hole is represented by a white circle. The minority carrier must then be directed to the subcell junction if it is to be collected. As the arrows indicate, the minority carriers (minority carrier is the electron in the case of the p-side of the middle subcell) experiencing a random walk away from the depletion region cannot overcome the potential barrier of the window layer so eventually they tend to diffuses towards the junction where they are swept into the emitter and then tunnel into the valence band of the top subcell. The process is the same in each subcell and hence three photons must be collected in order to supply one electron to an external circuit. The inherent reduction in current that is exhibited by the triple junction design compared to its single junction counterpart is accepted in exchange for a much higher cell voltage at the maximum power point which we study next.

2.2.5 Maximum Power Point

Finally, we discuss the maximum power point at which we hope to operate solar cells in the field. In one sense this case is not an extreme and as such we do not really identify any new physical processes. The maximum power point is simply the bias level between the short circuit and open circuit conditions (which we have already seen) that results in peak output power, where power is the product of the output current and voltage.

Figure 2-17 shows the energy band diagram of the solar cell at it maximum power point. The maximum power point of this generic cell is at ~1.8 V. In this case we still see a gradient in the quasi-Fermi levels in the junction, as we did in the short circuit case, which means we cannot simply add the quasi-Fermi level separations in each subcell to get the voltage as we did in the open circuit case. Rather the voltage can be read off the plot by comparing the majority carrier quasi-Fermi levels of the top subcell emitter (electrons) and the bottom cell base (holes). The voltage difference between the open circuit condition and the maximum power condition is due to the change in the quasi-Fermi levels across each subcell junction. Recall that the electron quasi-Fermi levels were flat across the junctions in fig. The majority carrier quasi-Fermi levels are once again equal in the tunnel junction. This is a necessary condition if tunneling is occurring. In an energy diagram it is not possible to visually determine how much current is flowing. A gradient in the quasi-Fermi levels indicates that current is flowing but that is all the information that is readily available.

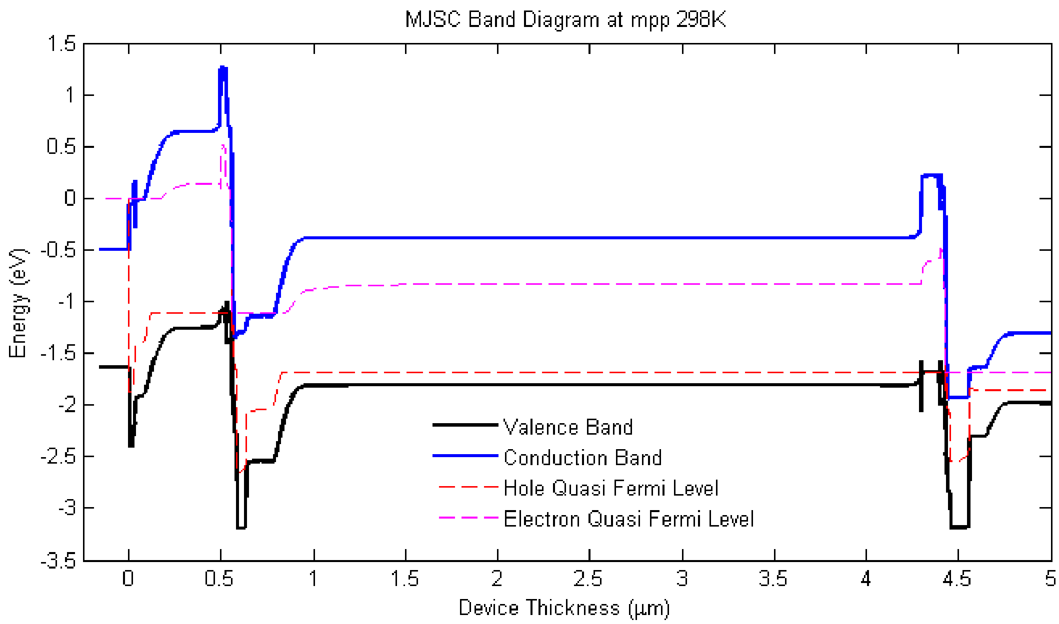

Figure 2-17: Energy band diagram of the first 5 microns of a generic triple junction cell at its maximum power point at 298K (25˚C). Only the top and middle junctions are completely shown.

3 Measurements, Equipment and Experimental Techniques

In this section the instrumentation and measurement techniques used to measure the solar resource are discussed. This corresponds to a) in Figure 1-11.

3.1 Equipment and Instrumentation

This section is intended to provide a description of the instrumentation used to monitor the SUNRISE demonstrator, a grid-connected solar energy test facility for CPV system evaluation. Also described are the in-house tools used to characterize high efficiency cells in the SUNLab before they are deployed. The data collected with these instruments are shown and analyzed.

The SUNRISE demonstrator was installed at the Canadian Centre for Housing Technology, Ottawa, Canada (45.45°N, 75.62°W) during the summer of 2010 and has been operational since September of the same year. The demonstrator holds 33 OPEL Solar MK-I Fresnel-lens-based, passively cooled, 550x concentrating modules on an OPEL Solar dual axis tracker that feed a two channel, 3kW, metered inverter. Each module contains six two-stage Fresnel-based concentrators that illuminate high-efficiency III-V triple-junction quantum-dot-enhanced solar cells designed and manufactured by Cyrium Technologies Inc..

An instrumentation panel on the tracker holds a pyrheliometer with a 5.7° circumsolar acceptance angle, a tracking pyranometer with a shading disk to measure diffuse irradiance and a spectroradiometer (wavelength range 350-1830 nm) used to measure the spectral content of the direct normal insolation (DNI). Temperature, pressure and relative humidity in a module are also monitored.

Climactic data are available via a weather station beside the test site that provides ambient temperature, relative humidity, wind speed and direction, and vertically and horizontally mounted global irradiance measurements.

It was necessary to develop a system capable of handling all of the data that would be collected. That system is described in Section 3.1.1.1.

3.1.1 Outdoor Test Suite at the SUNRISE Demonstrator

3.1.1.1 Remote Data Acquisition System

The first version of the data acquisition system, which has since been copied to facilitate the collection and distribution of data for other large projects, was developed with the help of Allan Johnson, a summer student who worked with me in the SUNLab during the summer of 2010. The system we developed is outlined schematically in Figure 3-1 [53].

Figure 3-1: Schematic of the SUNRISE demonstrator remote data acquisition system.

The picture in the top right of the schematic is the SUNRISE demonstrator. The following are the various components of the system.

A. Spectroradiometer – Mounted on the SUNRISE demonstrator and controlled remotely from the SUNLab at the university of Ottawa. Data logged directly on the SUNRISE server (G).
B. Weather station – Mounted on an adjacent test house at the Canadian Center for Housing Technology. Data logged and then saved to the on-site computer (E).
C. Two way grid meter and metered inverter – Inverter mounted on tracker pedestal and grid meter mounted indoors log data to the site computer (E).
D. Surveillance camera – Mounted in test house south of the demonstrator pointing north. Real time video feed accessible online and scheduled stills logged to on-site computer (E).
E. Site Computer – Backed up automatically through secure shell (ssh) network connection to SUNRISE Server (G) in the SUNLab at the University of Ottawa.

F. Remote Connection – Secure network connection through which scheduled backups are run in order to automatically transfer data from NRC to SUNRISE Server (G) at the University of Ottawa.
G. SUNRISE Server – Serves the SUNRISE Project Website from which queries can be made by authorized users to remotely access data organized in a database
H. Data Logger – Used to measure and log the signals produced by the pyrheliometer, the pyranometer and thermocouples mounted on the instrumentation panel.
I. SUNRISE Project Website – Allowed raw data to be accessed remotely over the internet via a password protected data return form.

3.1.1.2 Pyrheliometer

The instrumentation panel on the sunrise demonstrator holds three complementary pieces of instrumentation. The first is called a pyrheliometer which measured the direct normal incident (DNI) component of the *in*cident *sol*ar radi*ation* (insolation). The pyrheliometer is highlighted in Figure 3-2. It consists of a tube, painted black on the inside, with a high quality quartz window over a circular aperture, that achieves a 5.7° field of view. The sensing element is a thermopile (a number of thermocouples (~50-100) connected in series) that acts to convert a temperature gradient into an electrical signal. The thermopile is contained within a small black coated disk designed to achieve a flat absorption profile over the entire solar spectrum. The sensor is designed to have a linear response to incident radiation and is nearly temperature independent.

Figure 3-2: The highlighted instrument is the pyrheliometer mounted on the SUNRISE demonstrator. The pyrheliometer is used to measure the total incident power of the direct portion of the insolation.

The Eppley Normal Incidence Pyrheliometer (NIP) is factory calibrated and outputs an analogue signal, on the order of µV, that must be conditioned and logged with a data logger. A Campbell Scientific CR3000 programmable data logger was employed for this purpose.

In order to get a better feel for the accuracy and stability of the DNI measurement, made with the pyrheliometer at the SUNRISE demonstrator, the data were compared to that measured with a second Eppley NIP at another test site (APECS Project) located at the University of Ottawa. Due to the fact that the two pyrheliometers were not side by side this comparison is only meaningful when the sky is clear because clouds are understandably going to influence the insolation differently from one location to another. Table 2 shows the result of the comparison for mostly sunny days between March 2011 and September 2011 for the time both pyrheliometers were collecting data. The relative difference in the DNI measurements is plotted in Figure 3-3 where a negative percentage indicates that the pyrheliometer at the APECS site gave a higher reading and a positive percentage indicates that the SUNRISE pyrheliometer gave a higher reading. The red points indicate the relative difference between measurements on the first sunny day after both pyrheliometers were cleaned.

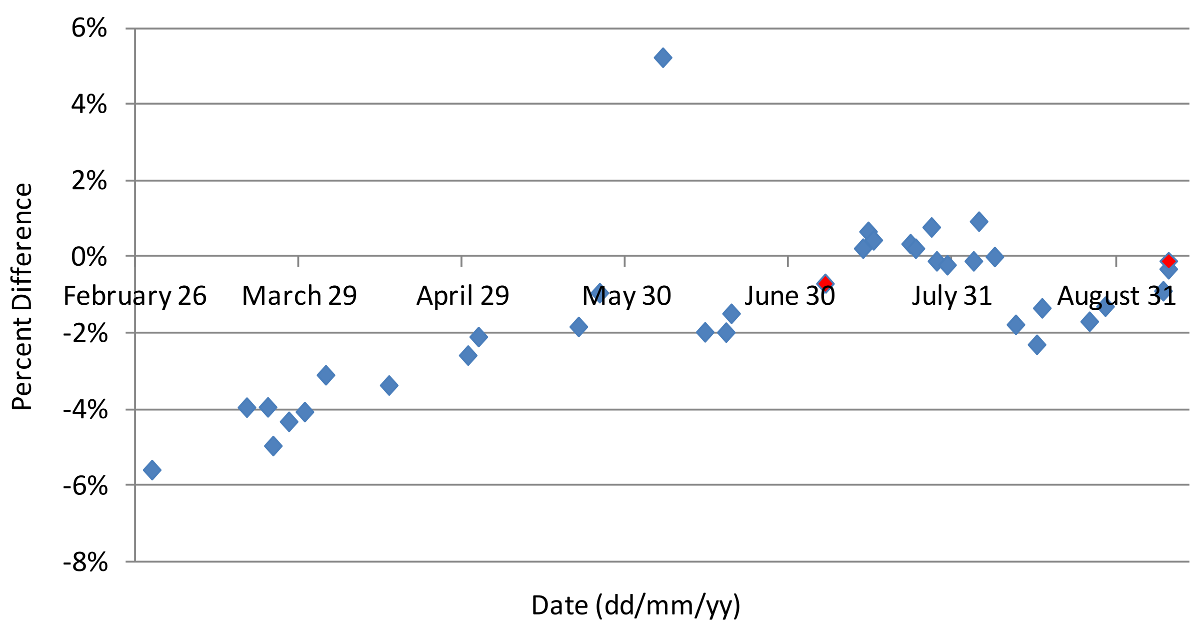

Figure 3-3: APECS / SUNRISE pyrheliometer comparison. Relative difference between DNI measurements at the SUNRISE and APECS demonstrator sites.

Due to the location of the pyrheliometers, a regular cleaning schedule was not followed. They were however cleaned a number of times and these dates are highlighted in Figure 3-3 and Table 2.

It is difficult to measure the effect of cleaning when the pyrheliometers are not right beside each other because this requires extremely clear days so that we can argue there should be no difference in insolation between the two test sites in Ottawa. When the sky is not perfectly clear the DNI between the two test sites is very difficult to compare. The single point at 5% on June 6th in is a result of trying to compare the DNI measurements on a relatively sunny day but when high cirrus clouds were present.

Table 2: Pyrheliometer comparison between identical Eppley NIP's at separate test sites (SUNRISE and APECS) in Ottawa, Ontario, Canada.

Pyrheliometer Comparison

Date	SUNRISE Max DNI (A) W/m^2	APECS Max DNI (B) W/m^2	Absolute Difference (A-B) W/m^2	Reletive Dif. (A-B)/(A+B)/2
Sunny Days				
March-01-11	903	955	-52	-5.60%
March-19-11	966	1005	-39	-3.96%
March-23-11	968	1007	-39	-3.95%
March-24-11	923	970	-47	-4.97%
March-27-11	949	991	-42	-4.33%
March-30-11	938	977	-39	-4.07%
April-03-11	951	981	-30	-3.11%
April-15-11	932	964	-32	-3.38%
April-30-11	915	939	-24	-2.59%
May-09-11	894	913	-19	-2.10%
May-21-11	863	879	-16	-1.84%
May-25-11	943	952	-9	-0.95%
May-31-11	SUNRISE Pyrheliometer Cleaned			
June-06-11	882	837	45	5.24%
June-14-11	901	919	-18	-1.98%
June-18-11	947	966	-19	-1.99%
June-19-11	932	946	-14	-1.49%
June-27-11	SUNRISE and APECS Pyrheliometers Cleaned			
July-07-11	951	958	-7	-0.73%
July-14-11	913	911	2	0.22%
July-15-11	909	903	6	0.66%
July-16-11	915	911	4	0.44%
July-23-11	887	884	3	0.34%
July-24-11	920	918	2	0.22%
July-27-11	905	898	7	0.78%
July-28-11	885	886	-1	-0.11%
July-30-11	925	927	-2	-0.22%
August-04-11	880	881	-1	-0.11%
August-05-11	866	858	8	0.93%
August-08-11	879	879	0	0.00%
August-12-11	890	906	-16	-1.78%
August-16-11	857	877	-20	-2.31%
August-17-11	884	896	-12	-1.35%
August-26-11	933	949	-16	-1.70%
August-29-11	914	926	-12	-1.30%
September-09-11	886	894	-8	-0.90%
September-10-11	APECS and SUNRISE Pyrheliometers Cleaned at 1:05 and 1:25pm respectively			
Before Cleaning	931	934	-3	-0.32%
After Cleaning	953	954	-1	-0.10%

It is interesting to note some trends in Figure 3-3. First, it should be noted that the DNI measurement at both sites agree quite well if they are cleaned once in a while, usually within 2%.

Also, in March and April it appears that the pyrheliometer at the SUNRISE site was quite dirty which is in agreement with visual checks performed during this period. There is a lot of dust and pollen in the air in the spring and the sunrise demonstrator sits in relatively close proximity to trees and pollen producing fields. However, the APECS site is in on a 4 story parking garage well above the trees and in a relatively dense area of town; it is conceivable that the APECS pyrheliometer simply would not soil as quickly in the spring.

To see how much cleaning the quarts window influenced the measurement, and also to see if both pyrheliometers were equally soiled, several attempts were made to clean both pyrheliometers at roughly the same time on a nice day. This was done on September 10th 2011, an extremely clear day in Ottawa. Before cleaning, the APECS pyrheliometer was reading about 1% higher than the SUNRISE pyrheliometer and after cleaning they read almost exactly the same. As shown in Figure 3-4 the SUNRISE DNI measurement increased by about 2.5% and the APECS DNI measurement increased by about 2%.

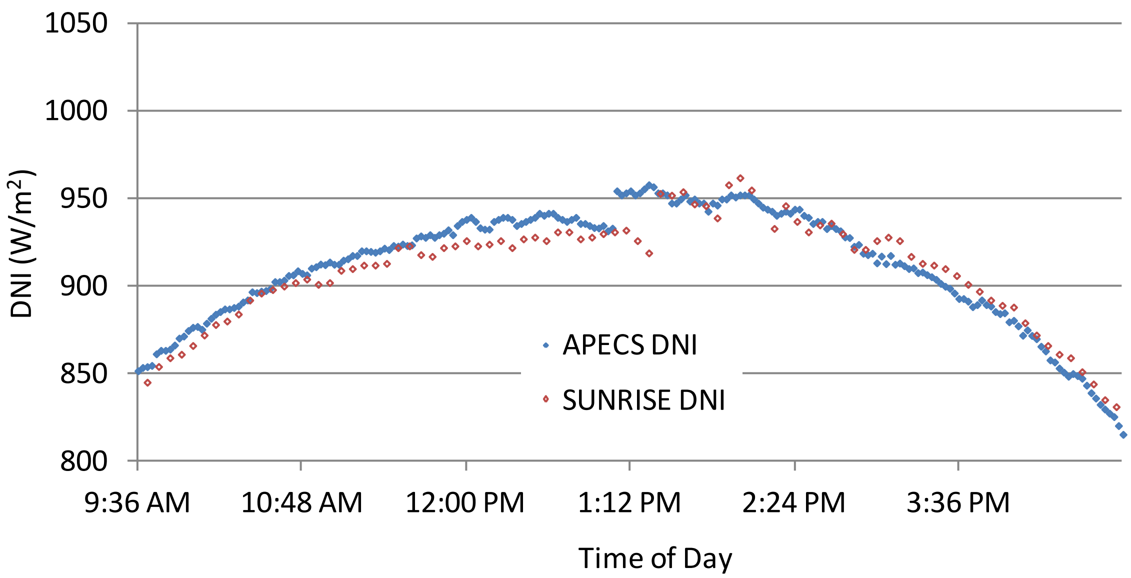

Figure 3-4: DNI measurements of pyrheliometers at the APECS and SUNRISE test sites. APECS data is logged every 2 minutes which is why the blue points are closer together than the points logged every 5 minutes at the SUNRISE site.

It is clear that a regular cleaning schedule is critical if an accurate measurement of the DNI is critical. Extra attention should be given to cleaning in the spring when there is more dust and pollen in the air and the location of a test site in proximity to rural landscape should also be considered. Cleaning the pyrheliometers once a week appears to result in measured DNI values within 2% of each other.

3.1.1.3 Pyranometer with Shading Disk

The instrumentation panel on the SUNRISE demonstrator also holds a pyranometer with a shading disk to measure the indirect (or diffuse) component of the insolation. The pyranometer and the shading disk are highlighted in Figure 3-5. A pyranometer by itself is a radiometric instrument that measures global irradiance, that is, the insolation from an entire hemisphere. The sensing element is a thermopile similar to the one used in the pyrheliometer (described in Section 3.1.1.2) The sensor is designed to have a linear response to incident radiation and to have a directional response that is described perfectly by the cosine of the angle between incident rays and the normal to the sensor. A double glass dome over the sensor has two effects (other than protecting the sensor from dust and rain) while maintaining a 180° field of view: the first is that it limits the absorption window by transmitting only wavelengths that are between ~300 nm and ~2800 nm; the second is the protection of the sensor surface from convective air currents which could affect the temperature at the surface of the sensor.

Similar to the pyrheliometer, the radiation absorbed by the pyranometer is converted to heat that flows through the thermopile and into the pyranometer housing. The gradient in temperature produces a proportional voltage output from the thermopile which can be measured and recorded with a data logger (an analog voltage output) and eventually converted to a total irradiance in W/m^2.

Figure 3-5: Highlighted instrument is the pyranometer with a shading disk mounted on the SUNRISE demonstrator. The pyranometer in this configuration is used to measure the total power of the diffuse or indirect portion of the insolation.

There were a several reasons for including a tracking pyranometer with a shading disk on the sunrise demonstrator. First, a tracking pyranometer without a shading disk would have measured the solar resource available to a traditional flat panel tracking without concentrating optics. However, for CPV applications we are more interested in the amount of light not captured by the optics. Since the direct portion of the insolation was already being measured by the pyrheliometer, it was more advantageous to measure the indirect portion of the insolation directly. This corresponds to the component of the insolation that is not harvested by high efficiency cells relying on concentrating optics.

It should be noted that concentrating optics have an acceptance angle within which light is concentrated onto the active area of the solar cell. The nearly parallel rays coming from the solar disk are within this acceptance angle but any rays incident on the optics from other points in the sky (due to Raleigh scattering in the atmosphere, reflections from clouds etc.) that are not within the optical acceptance angle are directed somewhere other than the active surface of the solar cell.

Looking first at the sunny days listed in Table 2, we find that given clear skies the average proportion of indirect insolation is 9.1% with a standard deviation of 1.9% absolute. This is a measure of the amount of indirect sunlight with respect to the tracking global irradiance when the sky is clear in Ottawa. This is true at any instant in time for an unoccluded-sun but the percentage increases quickly as clouds move by the solar disk. On March 19th there were no clouds obscuring the sun. The total integrated indirect insolation over the whole day was 9.0% of the total integrated global insolation. Measurements of the direct and indirect components of the insolation are shown for March 19th in Figure 3-6.

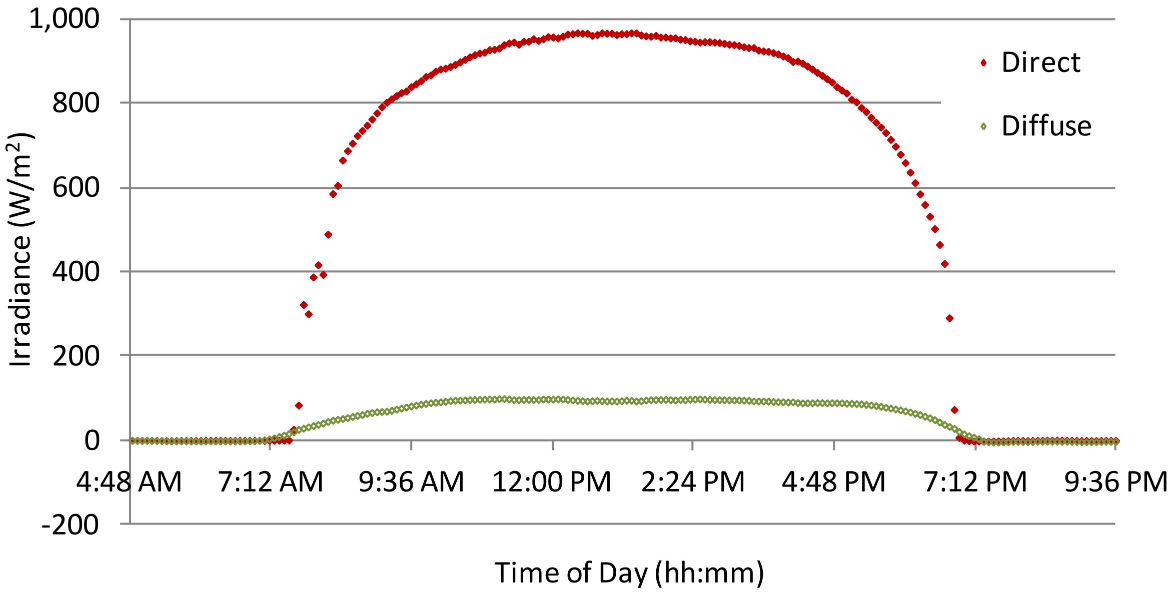

Figure 3-6: Direct and indirect components of the insolation on March 19th, 2011. March 19th, 2011 was a cool clear day with moderate ambient temperature fluctuation: High: 2°C, Low: -5°C and 30-40% relative humidity. The integrated indirect light was 9.0% of the tracking global irradiance on this day.

A more typical sunny day might look more like March 14th 2011, data for which are shown in Figure 3-7. There were a few clouds during the morning hours but largely clear skies thereafter, as the figure reveals.

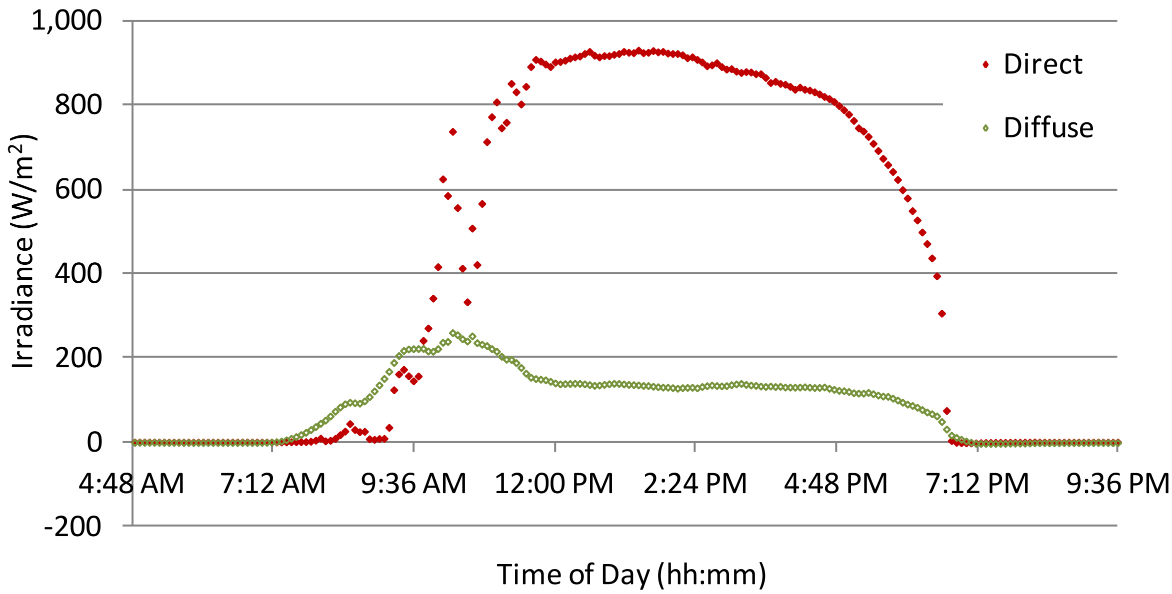

Figure 3-7: Typical sunny day (March 14th, 2011) in which a portion of the day was somewhat cloudy but a significant portion of the day is clear. It should be noted that even during the portion of the day that appears clear the indirect component of the insulation is approximately 13% of the global insolation.

April 20th, 2011 is an example of an overcast day in which almost no direct light was measured. The direct and indirect insolation on that day is shown in Figure 3-8. On completely overcast days with 100% cloud cover the direct light falls off to almost zero. The indirect component fluctuates with the thickness of the cloud cover but tends to remain quite low unless the cloud cover becomes extremely thin.

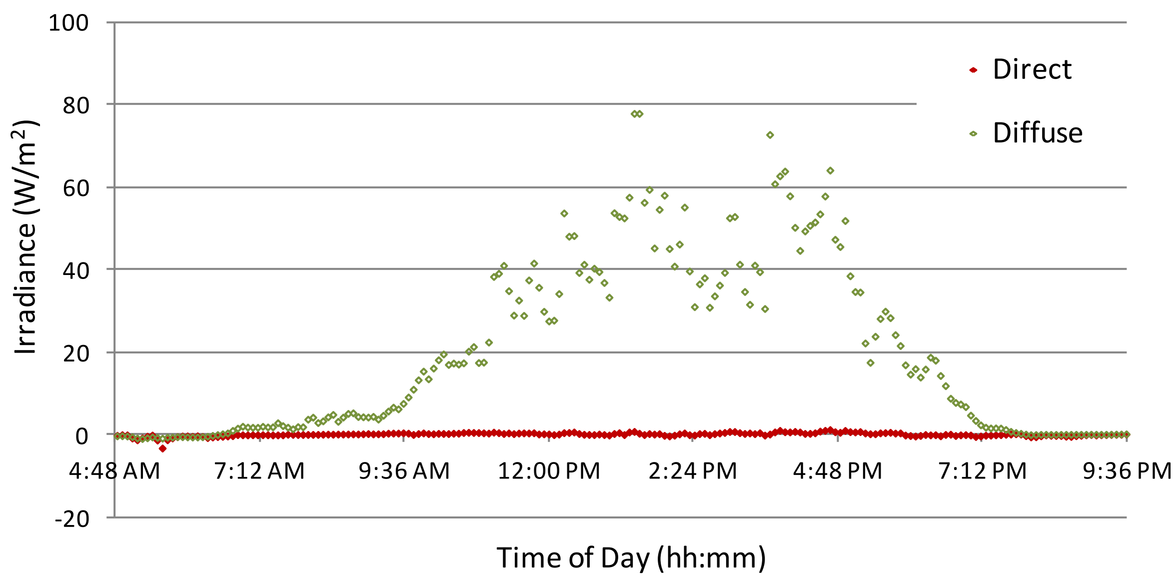

Figure 3-8: DNI and diffuse irradiance for April 20th 2011. The sky was completely overcast all day.

The diffuse component of the insolation becomes most significant under partially clouded conditions. When the sky is partially clouded the diffuse component tends to increase due to scattering and reflection from clouds. On September 22nd, 2010 a weather front moved through

Ottawa and provided four very distinct regimes on the same day. Figure 3-9 shows the data measured on September 22nd, 2010 with a picture of the sky taken at 3:48pm in the background.

The first period (7am – 9:30am) was a result of heavy cloud cover that steadily became thinner as the day went on. Data during the second period (9:30AM – 12:00PM) were taken when the tracker was manually powered down so that some work could be done. The third period (12:00pm – 4:20pm) occurred after the tracker came back on-sun but before the weather front had completely moved past the sun. During this period cloud cover was high and thin causing incredibly high forward scattering that resulted in extremely high diffuse insolation at more than 350 W/m^2. The fourth occurred when the front passed completely resulting in blue sky until sunset. At this point the diffuse insolation quickly dropped to 90 W/m^2 and then remained at 8% of the global irradiance until sunset.

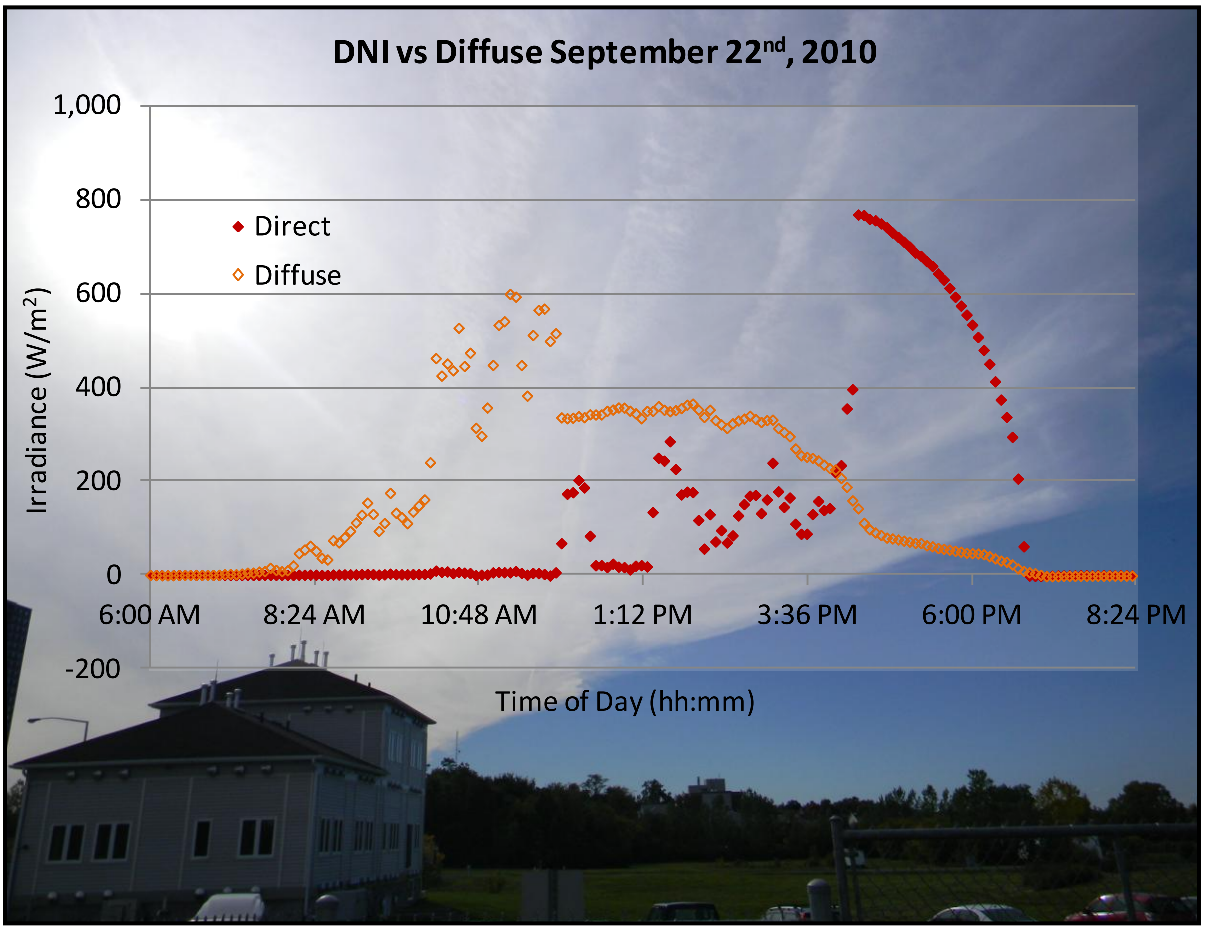

Figure 3-9: On September 22nd, 2010 a weather front moving through Ottawa and 4 distinct regimes were measured. From about 9:30am until just after 12:00pm the tracker was manually powered down so that work could be done. During this time while the cloud cover was becoming ever thinner, the pyrheliometer measured insolation from a small spot in the sky off sun and the pyranometer measured very close to the tracking global irradiance because the shading disk was not blocking out the solar disk. Thus the diffuse measurement just before noon is showing the sum of the direct and the diffuse and when the tracker went back on sun the direct and diffuse measurements were once again separated.

A useful observation was made when comparing the direct and diffuse measurements. Since the pyrheliometer has an acceptance angle of just over 5°, and the shading disk provides an exclusion angle of just over 5°, any time the tracker goes off sun the pyrheliometer measurement goes to zero and the pyranometer begins to measure the global irradiance. Thus on a sunny day we have a very effective way to determine if the tracker is on sun by simply looking at the collected data. Figure 3-11 is a calendar of select sunny days between March 19th and September 10th, 2011.

Beginning around March 30th spikes begin to appear in the morning and evening diffuse measurement indicating that some direct light was getting around the shading disk to the pyranometer sensor. Upon investigation, it was determined that azimuthal range limits in the tracker's software control system were set to allow azimuthal tracking of only 90° east and west of due south (i.e. 90° - 270° azimuth). This means that between the spring and fall equinoxes (March 21st and September 21st) the tracker was not able to track the sun from sunrise to sunset. This is most evident near the summer solstice when the days are the longest as we can see the data plotted for June 18th in Figure 3-11. In fact, on June 18th 22.1% of the direct insolation was incident when the sun was at an azimuth less than 90° or greater than 270°.

Once the problem was identified an attempt was made to modify the tracking software. It was soon determined that the azimuthal limits in the software could only be increased to allow for 208° of total azimuthal swing (i.e. 76° - 284°). This 76° - 284° range represents the mechanical limits of the tracker due to a missing pie slice as shown in Figure 3-10. On the summer solstice in Ottawa however, the sun rises at an azimuthal angle of 54° and sets at an azimuthal angle of 306°. Hence the mechanical limit of the tracker does not permit the tracker to follow the sun all year around. In fact, even on the equator the sun rises and sets at azimuthal angles of 66° and 293° on the summer solstice which is still beyond the tracker's mechanical limit. Thus there is no location on earth where the SUNRISE demonstrator would be able to track the sun all day long on every day of the year. This is a failure in tracker design.

Figure 3-10: The azimuthal tracking gear and the missing section which limits the azimuthal range of the tracker.

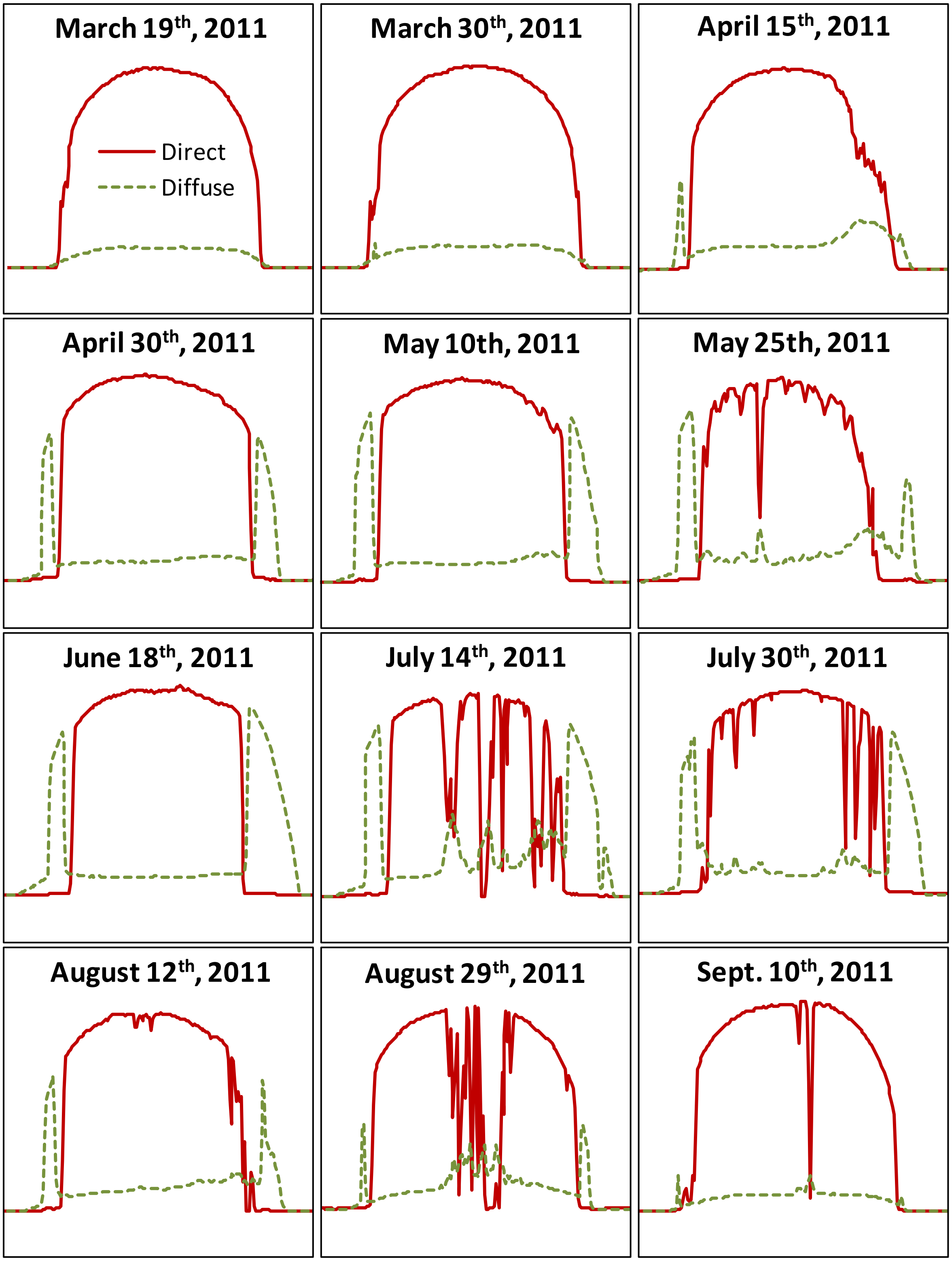

Figure 3-11: Calendar of sunny days during the spring and summer of 2011. Due to limits on the azimuthal range of the tracker the SUNRISE demonstrator was unable to track the sun for the whole day during the summer.

3.1.1.4 Spectroradiometer

A spectroradiometer is an instrument used to measure the intensities of the various colours comprising the light emitted from a source. Equivalently, this instrument is used to measure the spectral power distribution of an illuminant. The source in the present case is the sun, which as discussed in Section 1.3.2 emits a well characterized spectrum approximately described by a black body curve at the sun's surface temperature. However, despite the fact that the emitted solar spectrum is relatively stable over time (within about 15mW/m^2/nm at all wavelengths [54]), this is not what we observe on the surface of the earth. In fact, due to changes in air mass, water optical thickness and the aerosol optical depth the solar spectrum undergoes significant changes every day as well as over the course of a year. The most obvious daily change that a spectroradiometer allows us to quantify is the red shift that occurs in the morning and evening arising from stronger Raleigh scattering due to increased air mass. Higher energy photons scatter more often than low energy photons so the blue end of the spectrum responds more severely to changing air mass throughout the day than the red end of the spectrum. The fluctuations in the spectral irradiance are important to understand when trying to balance the photo currents generated in multiple subcells.

Figure 3-12: The highlighted instrument is the spectroradiometer mounted on the SUNRISE demonstrator in a ventilated heated enclosure. The custom enclosure allows the instrument to be left outdoors to collect spectra continuously even through a harsh Canadian winter. The direct attachment (white tube pointing at the sun) ensures that only the direct component of the insolation reached the diffuse cosine receptor which couples the light into the spectrometers fiber input.

The spectral distribution of sunlight is of interest in the solar power industry (especially in the CPV industry) because the PV systems used to convert light into electricity do not harvest energy from light with equal efficiency at all wavelengths. High-efficiency triple-junction solar cells, such as those undergoing development throughout the SUNRISE project (present in the SUNRISE demonstrator), are particularly susceptible to the influence of changing light conditions because their design is optimized to a specific spectrum.

The spectrum for which the cells should ideally be optimized is largely governed by the amount of atmosphere that the light travels through before reaching the ground. Thus the spectrum for which cells are optimized is in theory different for every latitude and elevation.

Ultimately, the spectral data collected by the spectroradiometer can be used in conjunction with the optical transfer function of the concentrating optics, a solar cell's spectral response, and other system characteristics (such as temperature and alignment) to determine the effects of said lighting conditions on overall system performance.

On the SUNRISE demonstrator a FieldSpec 3 (FS3) Portable Field Spectrometer from ASD Inc. (as shown in Figure 3-13) was installed as a spectroradiometer to characterize the solar spectrum at the site. The FS3 is a rugged spectrometer intended for outdoor use. It uses two detectors to measure between 350 and 1830nm. A 512 element silicon photodiode array was used to measure 350 nm to 1000 nm, and a thermoelectrically cooled InGaAs detector was used to measure between 1000 nm and 1850 nm. The fiber input to the spectrometer is factory calibrated and therefore permanently coupled to the spectrometer. The radiometric calibration necessary to configure the FS3 as a spectroradiometer with the diffuse cosine receptor (the foreoptic required for radiometric measurements) was also performed at the factory. It was done by placing the foreoptic on the end of the fiber input to the FS3 (set up as a spectroradiometer) and then measuring a well characterized light source at a known distance in a dark room. The known spectrum of the characterized source divided by the calibration measurement gives the calibration file used to correct other radiometric measurements.

Figure 3-13: ASD Inc. Field Spectrometer configured as a spectroradiometer sitting beside the enclosure that was retrofit to keep the instrument cool in the summer and warm in the winter.

When the spectroradiometer is put outside to measure the spectral composition of the direct portion of the sunlight, a tube called a direct attachment is placed over the fore optic to block out diffuse light. This ensures that only the spectrum of the direct light is measured since this is what is concentrated on the solar cell.

Table 3: Solar position, time of day and air mass on June 18th, 2011 in Ottawa, Canada

Zenith Angle	Elevation	Morning	Afternoon	Air Mass
85	5	5:51:57 AM	8:17:44 PM	11.47
80	10	6:24:30 AM	7:45:17 PM	5.76
75	15	6:55:21 AM	7:14:25 PM	3.86
70	20	7:25:11 AM	6:44:33 PM	2.92
65	25	7:54:24 AM	6:15:19 PM	2.37
60	30	8:23:13 AM	5:46:28 PM	2.00
55	35	8:51:52 AM	5:17:48 PM	1.74
50	40	9:20:34 AM	4:49:06 PM	1.56
45	45	9:49:37 AM	4:20:04 PM	1.41
40	50	10:19:26 AM	3:50:16 PM	1.31
35	55	10:50:45 AM	3:18:56 PM	1.22
30	60	11:25:00 AM	2:44:25 PM	1.15
25	65	12:08:53 PM	2:01:51 PM	1.10
22	68	1:04:31 PM	1:04:31 PM	1.08

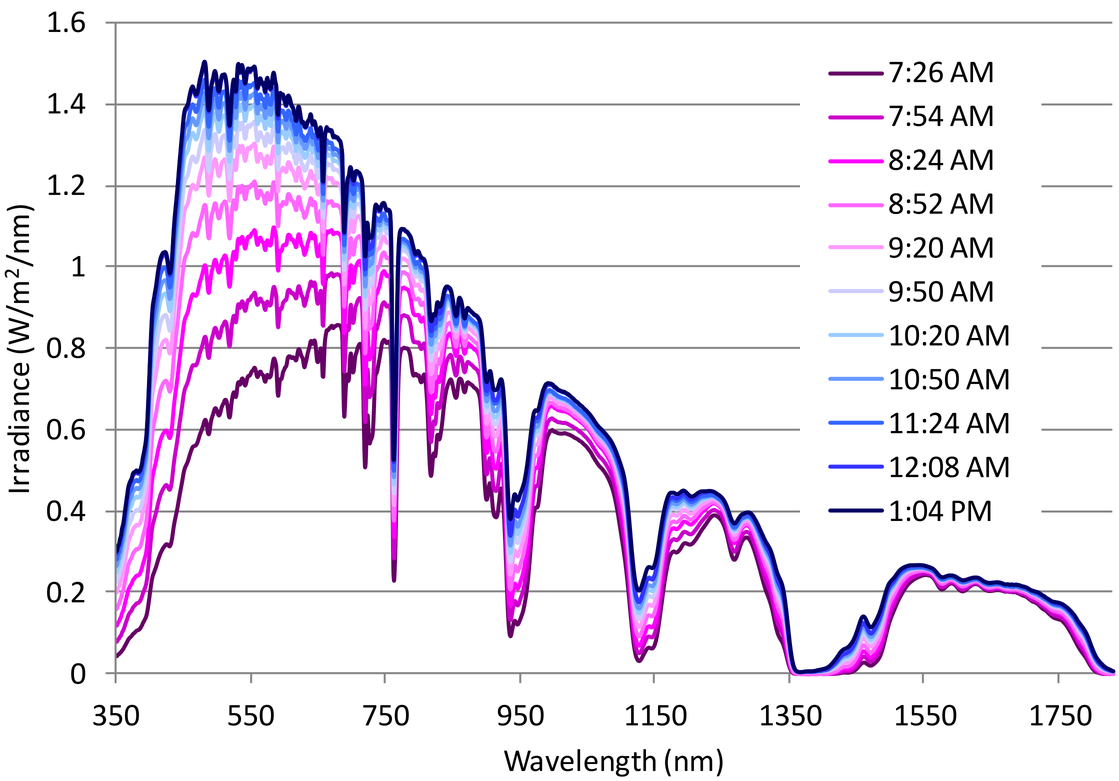

Figure 3-14: Direct solar irradiance measurements made in Ottawa on June 18th, 2011, the sunniest day near the summer solstice.

The solar elevation, zenith angle, time of day and air mass on June 18th are listed in Table 3 . Figure 3-14 shows an irradiance measurement for each air mass values shown in Table 3 except for the very early ones at which point the tracker was not yet on-sun.

The spectra presented in Figure 3-14 have been calibrated to the total DNI using the following method. First, the integrals of the measured spectra must be compared to the DNI measured with the pyrheliometer. This is achieved by calculating the percentage of the integrated power that is between 350 - 1830 nm for SMARTS2 simulated spectra (which extend from 280 - 4000 nm) at each air mass value. The integrals of the measured spectra should equal this fraction of the corresponding DNI measurements because the pyrheliometer absorbs almost perfectly across the same wavelength range (280 - 4000 nm). If the integrals do not already match they are scaled so that they do.

Notice again that the measured data extend from 350 - 1830nm. Sometimes however, it is necessary to estimate the spectra outside of this range, especially for shorter wavelengths, in order to make more accurate calculations of the expected subcell currents. If this is necessary, data are added using the tails (wavelengths shorter than 350 nm and longer than 1830 nm) of SMARTS2 simulated spectra of the same AM value. The appropriately scaled tails of the SMARTS2 spectra for each AM value are simply added to the measured data to complete the extrapolation. The result for June 18th, 2011 is shown in Figure 3-15.

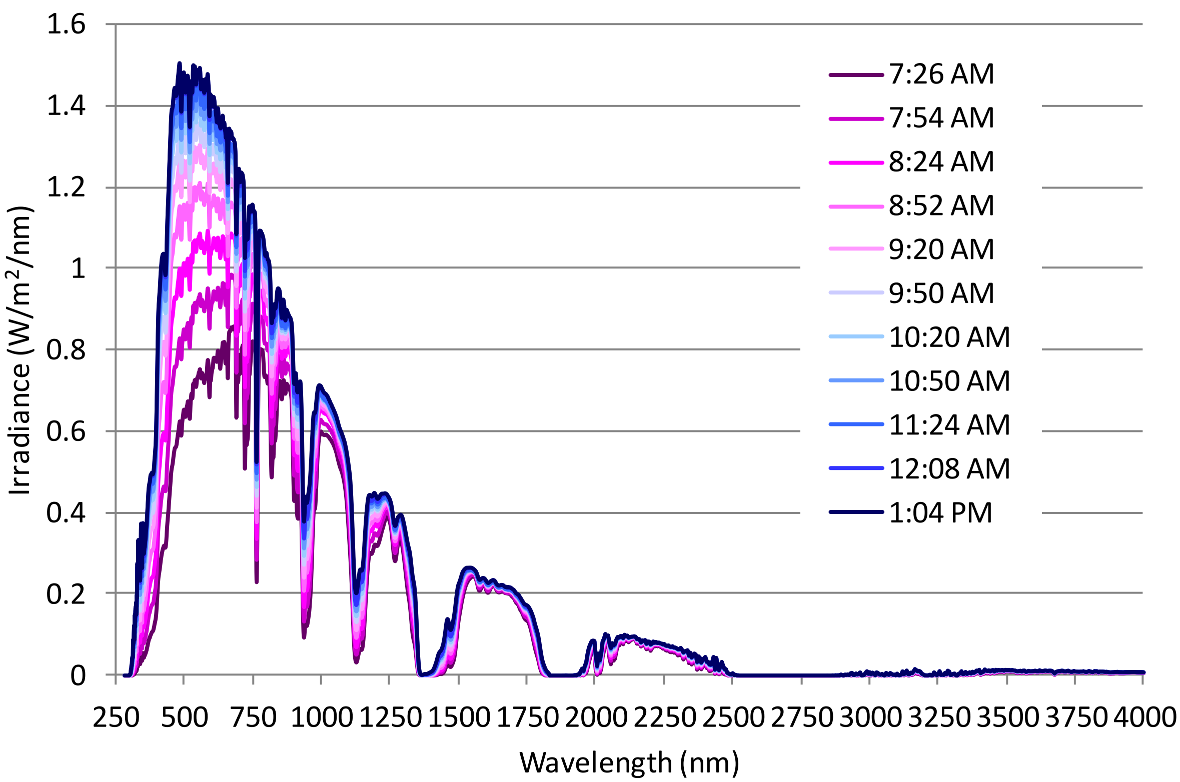

Figure 3-15: Direct solar irradiance measurements made in Ottawa on June 18th, 2011 with tails (data for wavelengths outside of the 350-1830 nm range that the spectroradiometer measures) added from SMARTS2 simulated spectra of the same air mass values.

3.1.1.5 Camera

A surveillance camera was installed in a building just to the south of the SUNRSIE demonstrator. The ProView Megapixel PoE Internet Camera from TrendNet provides a live feed accessible over the internet and is programmed to save still photos every minute so that it is possible to look back at the tracker at a given point in time if questions arise during data analysis. Tracking issues, shading from buildings in the winter months and stow events due to high winds are examples of interesting phenomena that can be confirmed by looking at the saved stills.

Time lapse footage of the SUNRISE demonstrator was also created by stitching the stills together at 25 frames per second in an *.avi file. This provided an easy way to visualize the effects of shading from buildings and cloud cover on the system performance.

3.1.1.6 Inverter (SUNRISE Demonstrator Electrical Performance)

The SUNRISE demonstrator was equipped with a two channel 3kW Aurora Inverter. Two sets of modules were installed, 15 modules in series on channel 1 and 18 modules in series on channel 2. Monitoring software supplied with the inverter allowed us to measure the following quantities:

- DC Voltage, current, power channel 1
- DC Voltage, current, power channel 2
- AC Voltage, current, power out
- Cumulative daily energy production

Figure 3-16 shows the cumulative energy production from the SUNRSIE demonstrator between October 2010 and September 2011. To this point, the demonstrator has produced just less than 1.8 MWh of AC electrical energy. Inverter efficiency has remained level at 97.0 % since the installation of the demonstrator.

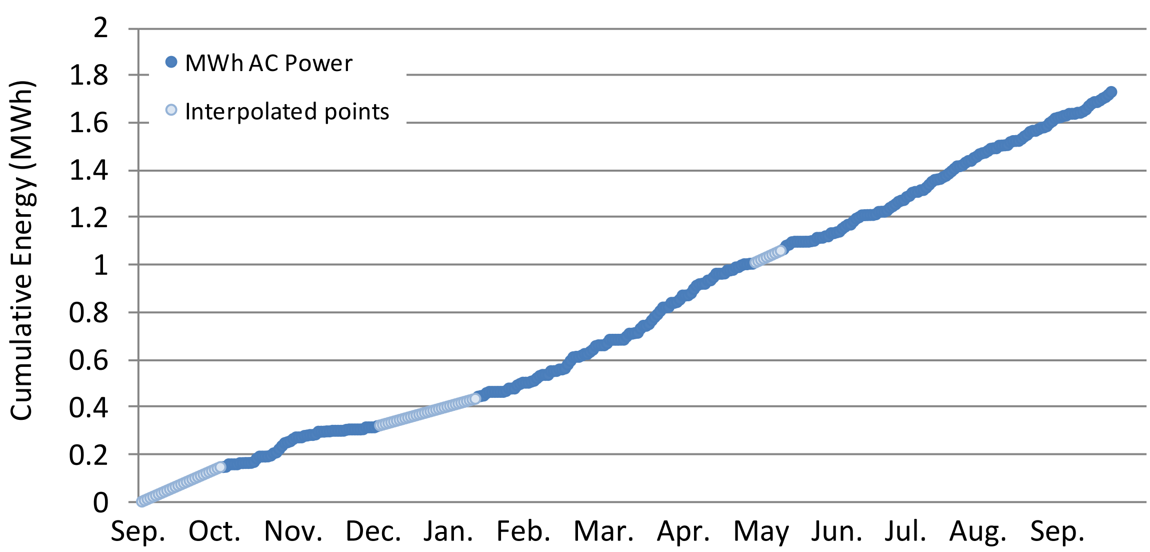

Figure 3-16: Cumulative energy production from the SUNRISE demonstrator between October 21st 2010 and September 18th 2011. The interpolated data points are included to represent estimates of the actual production because the inverter monitoring system was down for maintenance during these times.

3.1.1.7 Channel Voltage

Perhaps the most interesting system performance data are the channel voltages. The DC voltage of the two strings at the input of the inverter, sampled at 5 minute intervals, is shown in Figure 3-17 and Figure 3-18 for channels 1 and 2 respectively. It is immediately obvious that the full sun channel voltage is not stable over time as we would like it to be. The uncharacteristic decay of the channel voltage over time means that at least some of the cells are not operating at their maximum performance. The question is, what has caused this gradual drop in operating voltage?

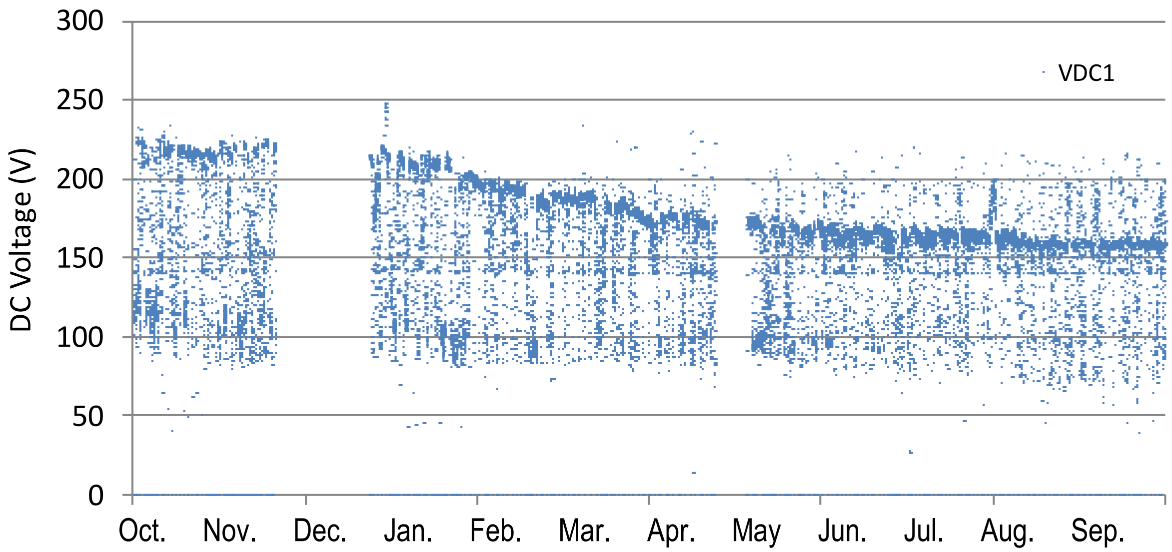

Figure 3-17: DC Voltage of channel 1 (15 modules of 6 cells each) at the input to the inverter. A very interesting uncharacteristic decay behavior is visible beginning at the end of November and early December. The gaps in the data exist because the inverter monitoring system was down for maintenance during these times. The inverter continued to produce power while this work was done.

It is important to understand what the various parts of these plots represent. We must, thus, know a little bit about how the inverter operates. The inverter itself remains off when it is not needed. It sits waiting while control circuitry monitors the open circuit voltage of its two DC input channels. The monitoring software does not record the channel voltages when the inverter is off. When the voltage on one of the channels (not necessarily both) increases to the preset "turn-on" voltage (200 V_{DC} on the SUNRISE demonstrator) the inverter turns on. The inverter then initializes that channel's connection to the grid which takes a few minutes. The monitoring software begins recording the voltage at the input of both channels as soon as the inverter turns on. Once a channel is connected to the grid, a maximum power point tracker (MPPT) (one dedicated for each channel) ensures that the channel remains biased for maximum power output. When the inverter is on, the monitoring software measures the voltage at the input of both channels even if one of them is below the turn on voltage. However, if the inverter is on and the voltage of one of the channels is below the turn on voltage then the MPPT for that channel is not operating and so the monitoring software records the open circuit voltage on that channel as opposed to the maximum power point voltage. The inverter transfers the maximum available power to the grid for any input voltage above 70% of the turn-on voltage which in this case is 140 V. The inverter will only turn off if the voltage on both channels falls below 70% of the turn on voltage. If the voltage on one of the channels falls below 140 V for a user specified amount of time, the inverter terminates that channels grid connection. The other channel will continue to supply power to the grid as long as the maximum power point voltage remains above 140 V. When the voltage on the second channel falls below 70% of the turn-on voltage the inverter waits for a few minutes (during which time the MPPT holds the input voltage of the second channel at 140 V) and then terminates that channels grid connection and turns off. This delay is in place so that fluctuations in the channel voltage due to intermittent cloud cover do not drive inverter cycling, as this would be inefficient.

The cluster of points that form a horizontal line visible in the middle of the channel 1 data and near the bottom of the channel 2 data at 140 V is an artifact of the inverter measurement that is only visible when data for many months is consolidated onto a single plot. It occurs because a few points are sometimes recorded at 140 V during the grid connection sequence and during the user specified delay before the inverter shuts down.

The vertical thickness of the data set, or the daily voltage range, is governed on the low voltage end by the minimum open circuit voltage the cells can provide when they are illuminated with only diffuse light. In the data for channel 1 which only has 15 modules we see many measurements below the 140 V level because if channel 2 which has 18 modules remained above 140 V then the inverter remained on. Channel 2 data sets have a few points below 140 V which can be measured if the illumination fluctuated during the grid connection process. The maximum voltage is governed by the open circuit voltage of the cells when they are under full illumination. The thick decaying line represents the maximum power point of the string which is further from the open circuit voltage at the end of the year than it is at the beginning of the year.

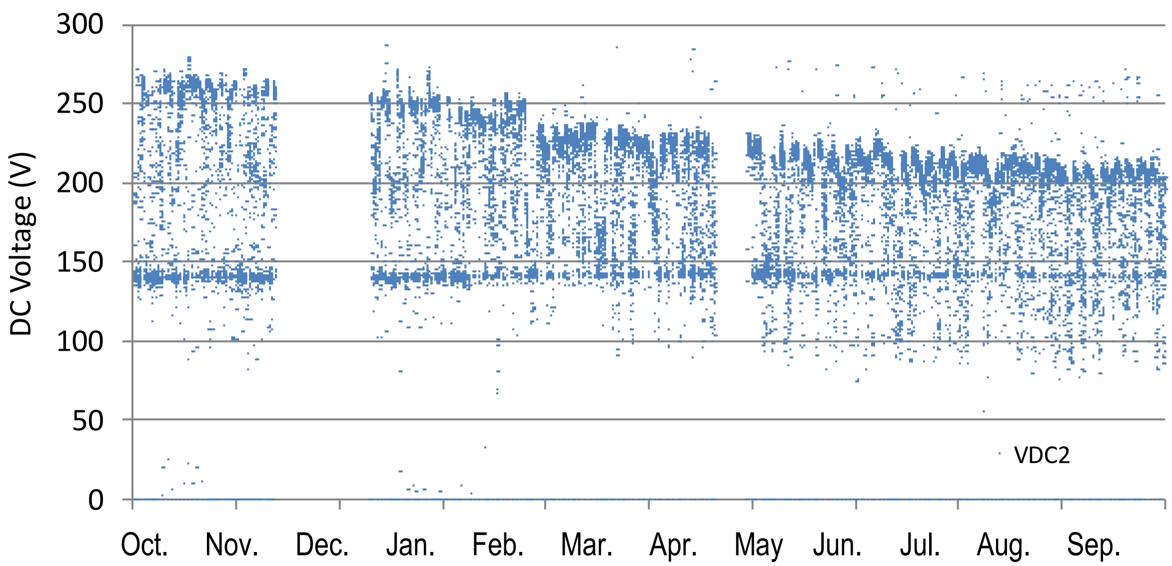

Figure 3-18: DC Voltage of channel 2 (18 modules of 6 cells each) at the input to the inverter. The gaps in the data exist because the inverter monitoring system was down for maintenance during these times. The inverter continued to produce power while this work was done.

It is interesting, that there are data points above the slowly decaying thick line (which is the sag in maximum power voltage under stable full sun conditions over the year). These points are measured at the open circuit voltage of the string when the string is not grid connected. It is also interesting that very few of these points were measured before December on either channel. This is expected since at the beginning of life the cells maximum power voltage is expected to be quite close to the open circuit voltage. The points usually occur on partially cloudy days, when the sun first strikes the demonstrator in the morning, or on a very rare occasions when very thin even cloud cover reduces the direct insolation considerably without blocking it altogether. Figure 3-19 shows the channel 1 voltage for May 20th, 2011, a day with intermittent cloud cover and May 21st, 2011, a clear sunny day.

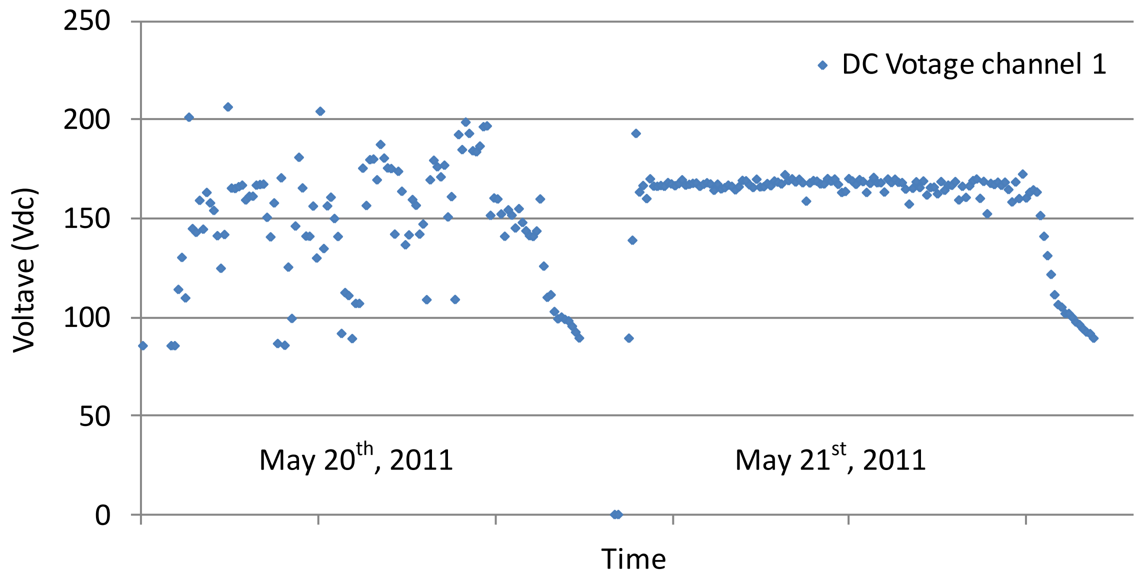

Figure 3-19: DC voltage on channel 1 on a partially cloudy day (May 20th, 2011) and on a sunny day (May 21st, 2011)

The sporadic distribution of points on May 20th 2011 occurs because the channel is only grid connected for a couple of short periods of time throughout the day. Most of the time the voltage measured is the open circuit voltage of the string and not the maximum power point voltage. If one looks closely, a few points at 140 V are noticeable which occur at different points during the day during the grid connection sequence. On May 21st 2011 the sun was stable for the whole day. A few points were recorded at the beginning of the day before the channel was grid connected but then the maximum power voltage is recorded for most of the rest of the day. When the sun goes down the measurement does switch back to the open circuit voltage but this transition is not very noticeable due to the resolution (5 minute samples) of the data set.

3.1.1.8 Channel Current

The DC current from channels 1 and 2 are plotted in Figure 3-20 and Figure 3-21 respectively. Theoretically, the maximum currents produced should scale almost linearly with the DNI so the upper profile of the data in these plots should highlight the time of year when the solar resource was the most intense given clear skies. This profile can then be compared to the maximum instantaneous DNI measurement taken for each day plotted in Figure 3-22.

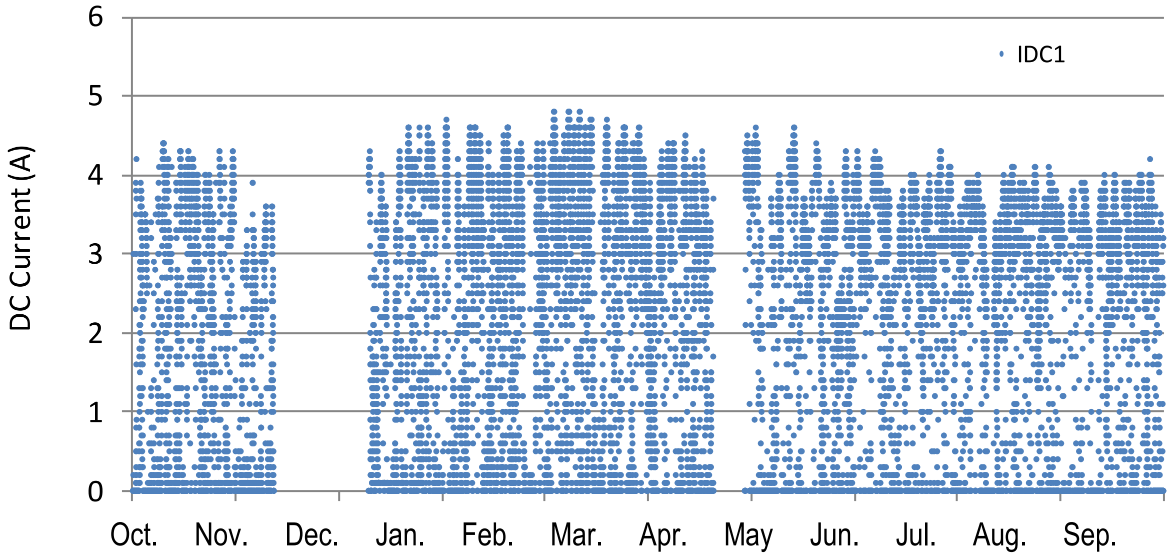

Figure 3-20: DC current of channel 1 at the input to the inverter. The gaps in the data exist because the inverter monitoring system was down for maintenance during these times. The inverter continued to produce power while this work was done.

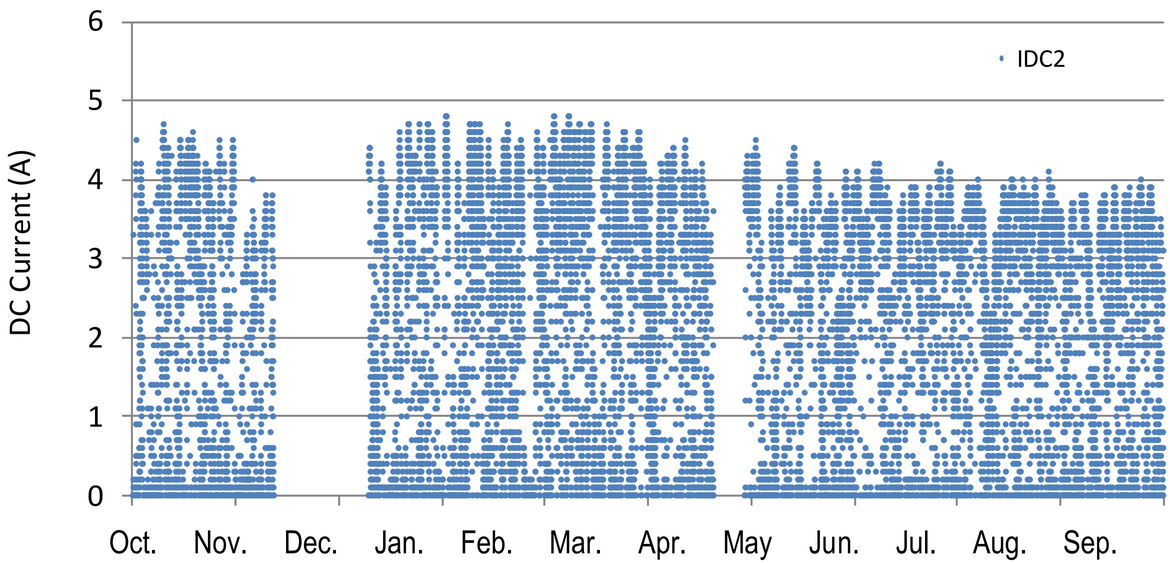

Figure 3-21: DC current of channel 2 at the input to the inverter. The gaps in the data exist because the inverter monitoring system was down for maintenance during these times. The inverter continued to produce power while this work was done.

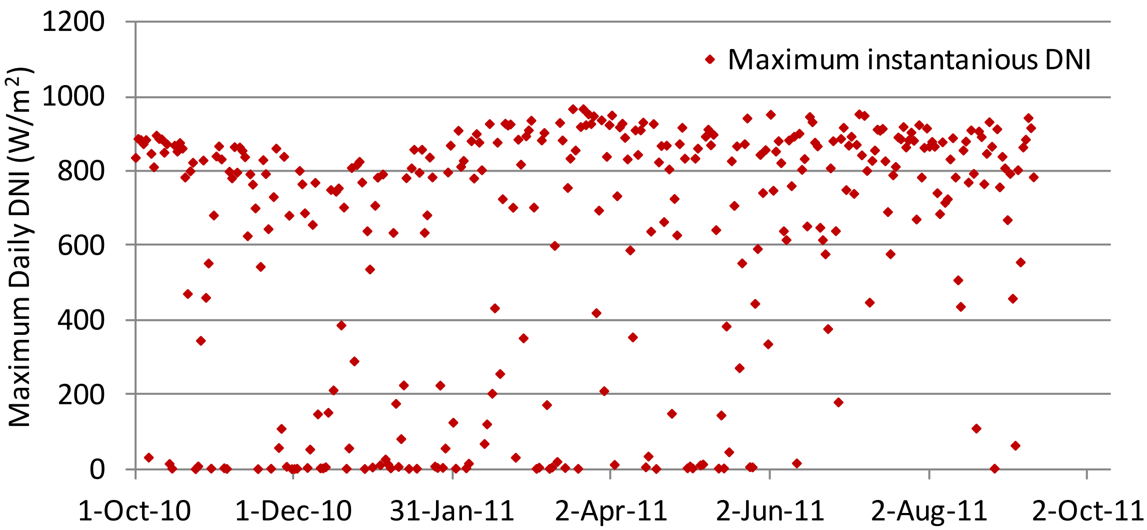

Figure 3-22: Maximum instantaneous DNI measurement each day of the year. The dip in the data is centered around the winter solstice. On this day the sun reaches a maximum elevation of 21.18° which corresponds to an AM value of 2.8. The very high air mass acts to reduce the maximum DNI.

It is clear that when comparing Figure 3-21 and Figure 3-22 that the current does not follow the DNI throughout the year as one would expect. Rather the maximum power current roughly follows the DNI late in 2010 but then steadily decays between February 2011 and September 2011 over which time the DNI remains at its highest and relatively constant. This indicates that either there exists a mechanism whereby the optical transfer function of the concentrating optics is changing over time, or the IV characteristics of the strings have changed in such a way that the maximum power current is different from the short circuit current. The latter could be the case if an increase in series or shunt resistance were to arise as a result of a damaged cell.

A measurement of the L-I-V characteristics of the modules would provide useful information about the series and shunt resistance and the differing performance of various modules. Such a measurement is recommended as future work. Other effects such as the warping of Fresnel lenses or the discoloration of concentrator material which would lead to changes in the optical transfer function of the concentrating optics could also affect the current over time. Measurements of the optical transfer function of new modules and a comparison with the optical transfer function of old modules would show if such degradation had occurred. Measurement of the optical transfer function of modules is also recommended as future work.

3.1.1.9 Instantaneous Channel Power

The net effect of the degradation in voltage and current is apparent when we look at the power being extracted from the system. Figure 3-23 and Figure 3-24 show the instantaneous DC power being extracted from channel 1 and channel 2 respectively. The same plateau in late 2010 and then constant decaying shape we saw in the plots of channel voltage is once again evident here. Since both the voltage and the current decreased over the year, it is expected that the power (the product of these two quantities) will follow the same trend. This is exactly what we observe. The decreased output power divided by the strong DNI through the summer results in system efficiencies that are significantly reduced since the system was deployed.

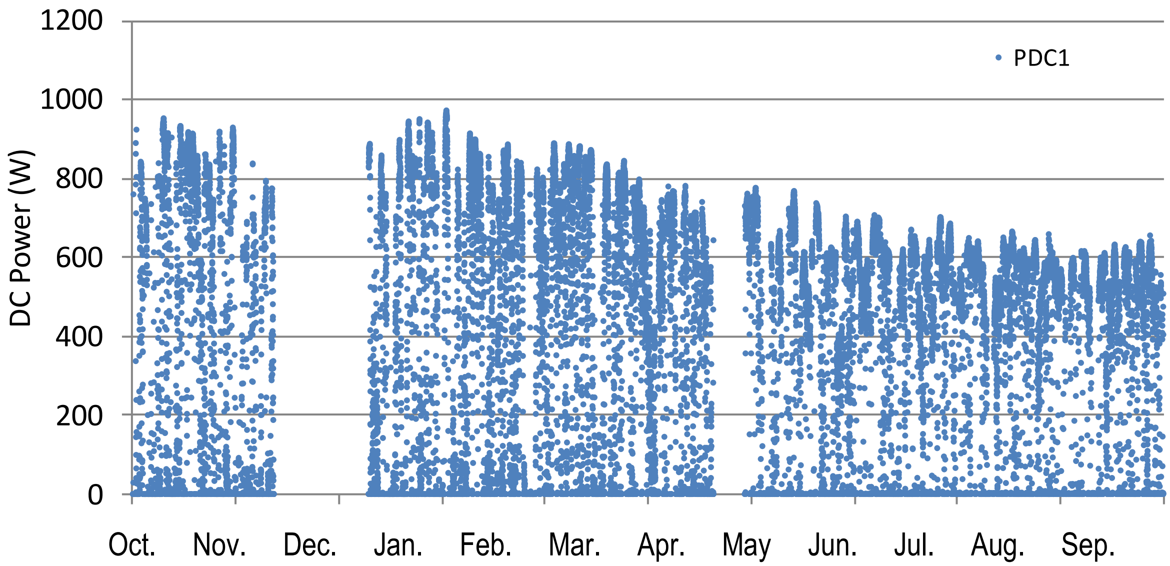

Figure 3-23: DC power of channel 1 at the input to the inverter.

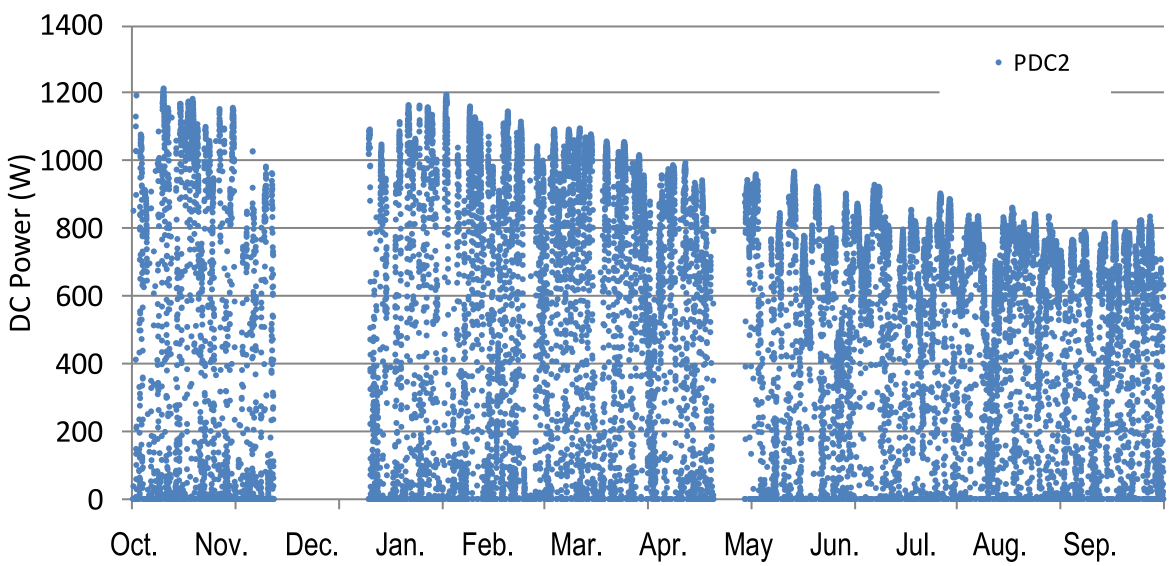

Figure 3-24: DC power of channel 2 at the input to the inverter.

3.1.1.10 System Efficiency

The efficiency calendar shown in Figure 3-25 allows us to see how the system performance changes over time. The efficiency curves are extremely helpful when trying to identify performance issues because the efficiency takes into consideration the system current, the system voltage, and the available insolation. Even the spectral content of the insolation has an obvious effect on the shape of the efficiency curves and thus almost all performance limiting issues are visible in the system efficiency curves. Some of these issues will be discussed below.

In summary, we see a decrease in the peak system efficiency over the first year from over 21% to less than 14% in some cases by September 2011. This system degradation is unacceptable for a system that is intended to operate for more than 20 years with minimal interference.

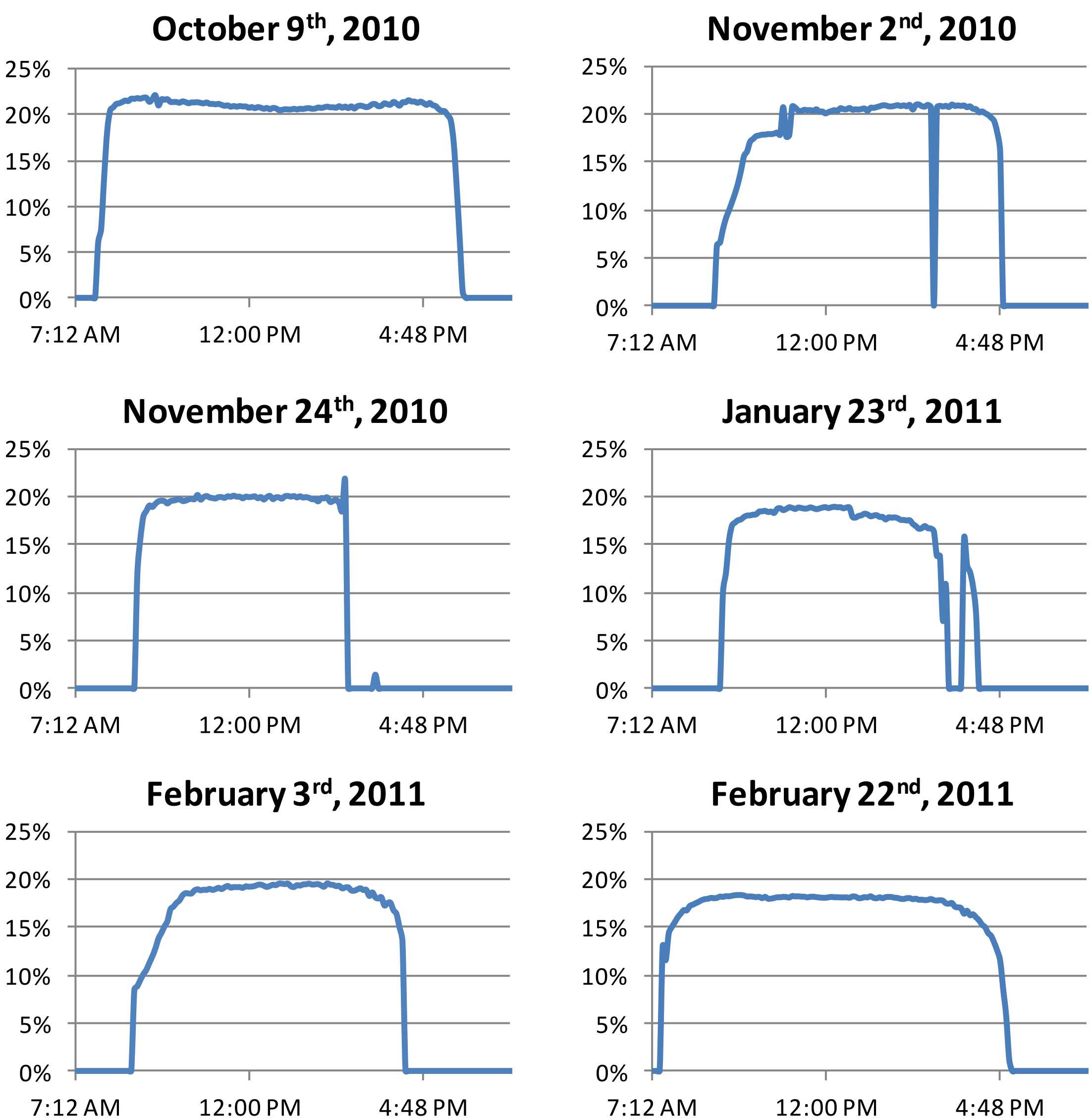

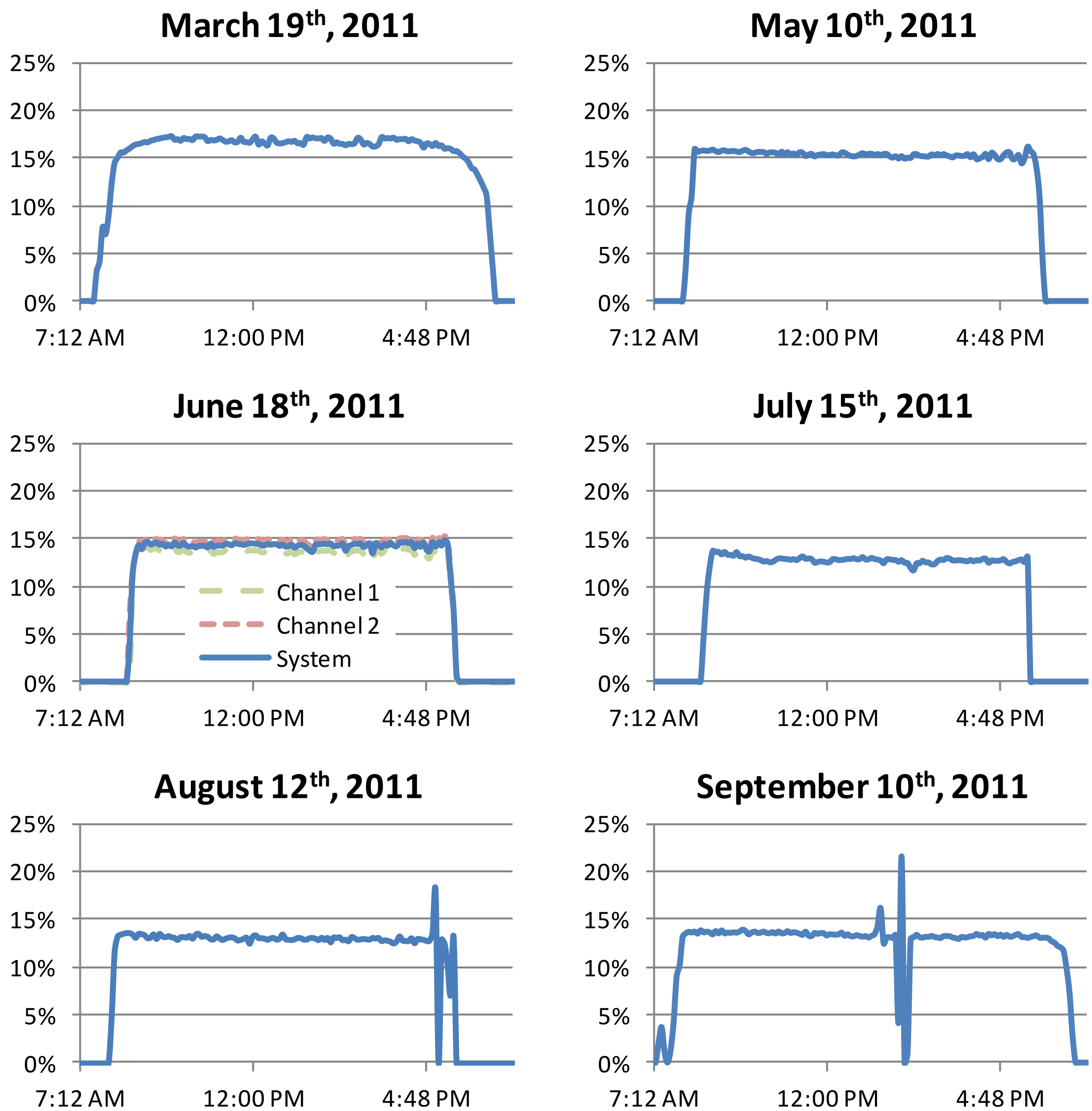

Figure 3-25: DC system efficiency of the SUNRISE demonstrator on the specified dates calculated using the optical aperture of the module optics. i.e. the narrow frame of the module is not included in the area calculation.

October 9th 2010 was the first completely clear day of sunshine that the SUNRISE demonstrator experienced. With a peak DC efficiency of 22 % the demonstrator produced a total of 19.2 kWh of AC energy. This was the demonstrator's highest producing day since it went online at the end of September 2010. The broad shoulders on the efficiency curve are characteristic of a tracked system and the efficiency peaks at 9:15am and 4:25pm which both correspond to an air mass value of ~2.5 are the points at which the top and middle subcells are nearly perfectly current matched. Since the cells are optimized for an air mass value of 1.5 at an estimated operating temperature, this suggests that either the optimal air mass has shifted due to a change in the subcell absorption properties or the optics are causing a blue shift in the incident spectrum as the light traverses the optical train to the cell. Relatively more power towards the blue end of the spectrum means that the middle subcell will become current limiting at higher air mass values (i.e. earlier in the morning and later in the afternoon).

On November 2nd, 2010 a realignment of the tracker was performed around 10:30AM because the sun sensor that is used to track the sun had become misaligned. The realignment process resulted in the spike and eventual increase in efficiency from just under 18% to just over 20%. An alignment issue should mainly affect the current produced by the cells which is confirmed in Figure 3-26 and Figure 3-27 which show the channel currents and voltages on November 2nd. A step is clearly visible in the current output on both channels, however, there is almost no fluctuation in the voltage. This is what we expect since the current is basically linearly dependant on the intensity while the voltage is only logarithmically dependant on the intensity.

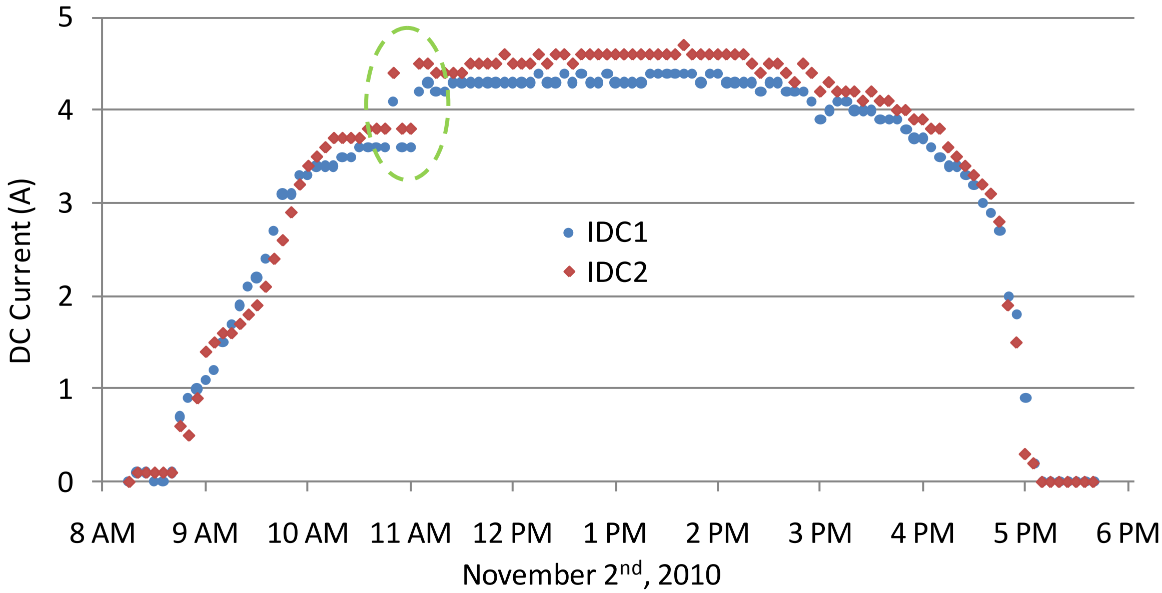

Figure 3-26: Current produced by channels 1 and 2 on November 2nd, 2010. The spike in the current as the tracker was moved past optimal alignment and then the eventual increase in current is visible as a step in the data around 10:30 in the morning.

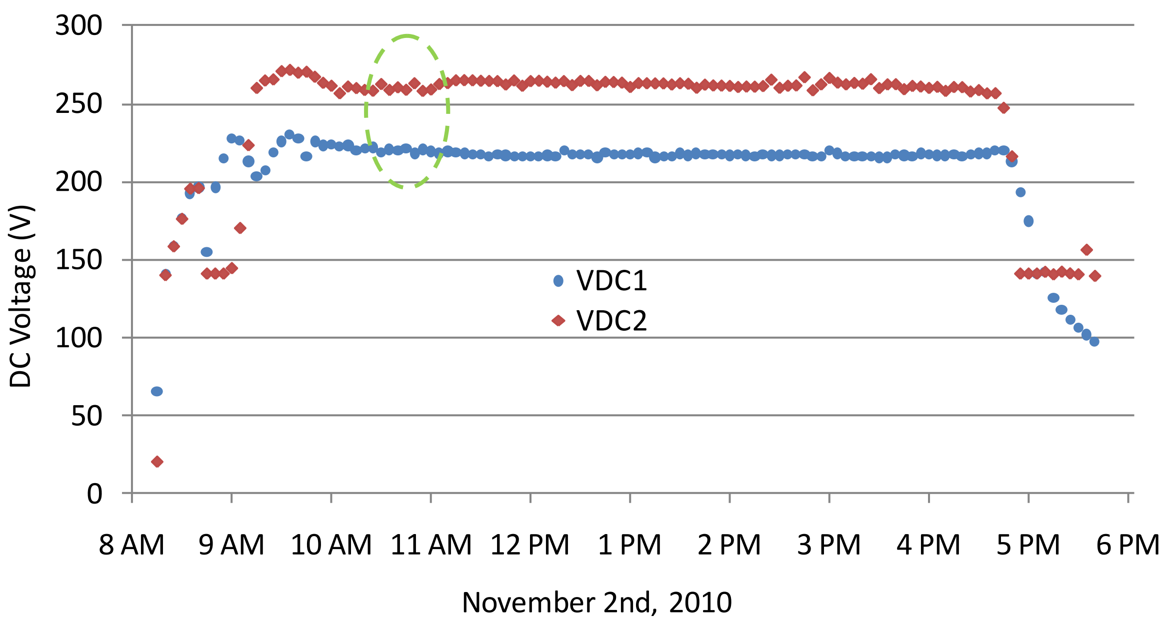

Figure 3-27: Voltage produced by channels 1 and 2 on November 2nd, 2010. Almost no voltage fluctuation due to the realignment is visible in the data.

On November 24th and January 23rd the efficiency curves cut out in the late afternoon. This is simply due to shading from a distant apartment building because the sun is particularly low in the sky at that time of year.

There is another feature in the November 2nd data which is uncharacteristic. The slow steady rise to peak efficiency in the morning (also visible in the February 3rd, 2011 efficiency curve) is due to a slight tracking misalignment during this period which corrects itself by about 10:00am. In general a feature like this in an efficiency curve (resulting from low channel currents as shown in Figure 3-28 but almost normal voltages as shown in Figure 3-29) could also be caused by shading if the pyrheliometer was illuminated while a portion of the modules were shaded resulting in less electrical power output than would be expected for the measured DNI. This is not the case here. During the shortest days of the year around the winter solstice, the sun comes up over the building to the south-east of the demonstrator and since the pyrheliometer is on the instrumentation panel in the lower left hand corner of the demonstrator it is illuminated at the same time as the last few modules. The only artifact we see in this case is an "infinite" efficiency resulting from the production of power from illuminated modules before the pyrheliometer is illuminated. On November 2nd and February 3rd the inverter turned on and began exporting power before the pyrheliometer was illuminated. The pyrheliometer was illuminated by about 9:00am on both of these days which is where the plotted efficiency curves begin. The whole demonstrator was completely unshaded on both days by 9:30am but the artifact in the efficiency curves does not disappear until after 10:00am. Also, a shading issue would appear in the data on days between November 2nd and February 3rd. Thus a minor tracking error seems the only explanation.

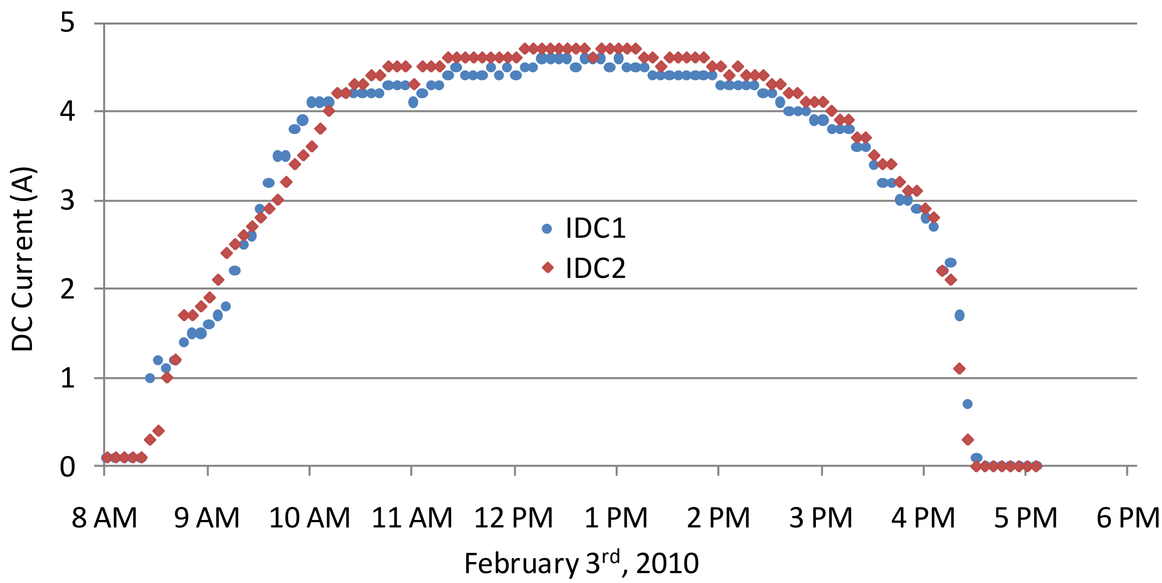

Figure 3-28: Current produced by channels 1 and 2 on February 3rd, 2010.

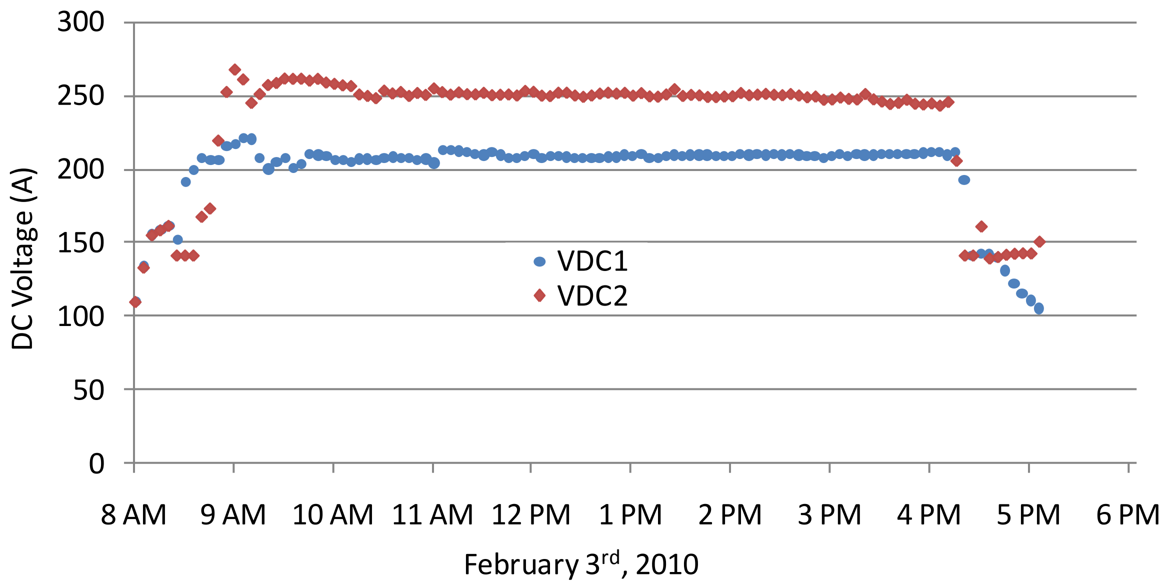

Figure 3-29: Voltage produced by channels 1 and 2 on February 3rd, 2010.

The artifact in the efficiency curve could be in part due to the fact that the sun sensor (also on the instrumentation panel) which optimizes the alignment of the tracker, was not illuminated on these days until about 9:15am. Before the sun sensor is illuminated the tracker relies on a preprogrammed solar position calculator which is not as accurate as the closed loop tracking provided by the sun sensor. Thus, it is conceivable that the slight misalignment occurred after the inverter turned on but before the sun sensor began optimizing the tracking position. Unfortunately, this does not explain why it took until 10:00 am for the sun sensor to find the sun on the two days discussed, nor does it explain why this artifact does not seem to exist in the efficiency curves between November 2nd and February 3rd when the same shading effect was happening daily.

The only other interesting artifact in the efficiency curves shown in Figure 3-25 is the sharpness of the corners of the curves for days between March 21st and September 21st. As discussed in Section 3.1.1.3, this is a result of the fact that the tracker did not have enough azimuthal range to track the sun on those days. Thus, the data are simply cut off in the morning and the evening when the tracker began following the sun and finished following the sun respectively.

3.1.2 Indoor Test Suite at the University of Ottawa SUNLab

The SUNLab is a solar cell characterization facility and is equipped with all of the instruments necessary to make accurate electrical and optical performance measurements on solar cells under concentrated illumination.

3.1.2.1 Artificial Suns

The use of artificial suns allows the indoor testing of devices without exposing them to the elements or requiring expensive packaging. Bare cells or cells on carriers can thus be tested in the laboratory under controlled conditions before they are incorporated into modules and put on sun in the field. Artificial suns also allow us to compare various cells under well understood illumination conditions.

The artificial suns (or solar simulators) in the SUNLab were used to characterize the solar cells that were then installed in the SUNRISE demonstrator. This information was then used to calibrate the model that is described in Chapter 4.

3.1.2.1.1 Oriel Solar Simulator (Low concentration continuous illumination ~1-150suns)

The Oriel 92191 solar simulator is capable of uniformly illuminating a solar cell at up to 150 suns intensity and is powered by a 1600W xenon lamp. The maximum uniform beam area is approximately 5cm by 5cm at low concentration. A series of optional filters are used to control the output spectrum and can be chosen to yield a beam that simulates the following Air Mass (AM) spectra: AM0, AM1, AM1.5G, AM1.5D, and AM2.

The photovoltaic characterization station that accompanies the Oriel solar simulator is shown in Figure 3-30 and includes a test stage fitted with a temperature controller and a vacuum pump so that both bare cells and chips-on-carriers can be characterized. The ability to measure cell characteristics over temperature allows temperature coefficients to be determined using this experimental setup.

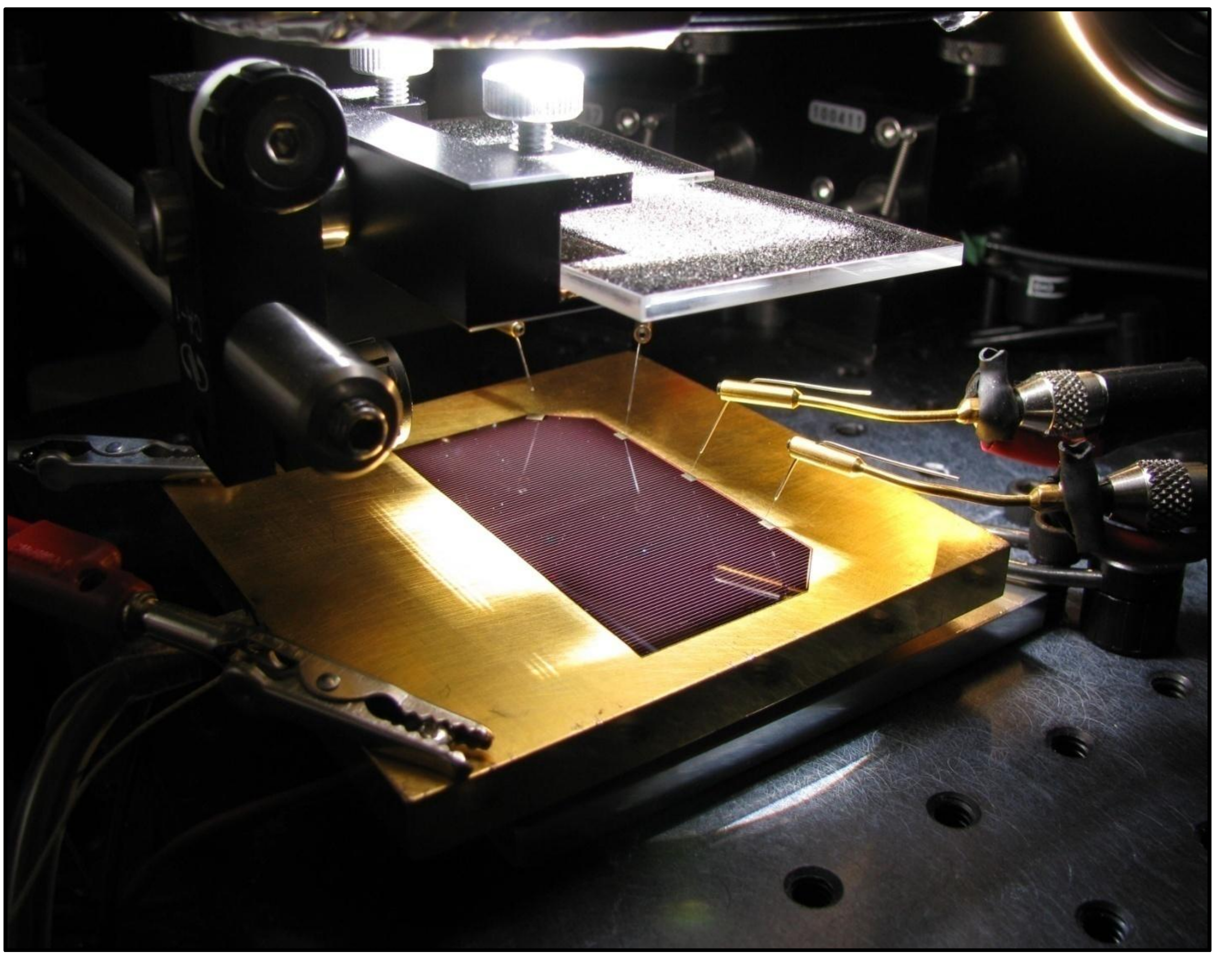

Figure 3-30: Oriel solar simulator test station SUNLab, 2010. In this picture an EMCORE solar cell is illuminated under an attenuated beam. The solar cell is secured with a vacuum pump, on a gold plated stage which serves as the connection to the back contact of the cell. Four micro manipulators are used to touch probes down onto the top contacts on the surface of the cell.

3.1.2.1.2 XT-30 Solar Simulator (High concentration continuous illumination~1000suns)

This state-of-the-art system is the first of its kind in the world. Designed by Spectrolab, the XT-30 solar simulator shown in Figure 3-31 is powered by a 3000W Xenon lamp capable of delivering over 1000 suns continuous illumination uniformly over a 1cm by 1cm area. The system includes an AM1.5D filter in order to simulate the terrestrial spectrum. The spectrum can be modified further with the addition of band filters mounted within the system. Water cooled stages allow chips-on-carriers to be characterized at high intensity without overheating. This heat removal method relies on successful heat transfer from the cell surface to the stage which may be limited by vulnerabilities in the cell and/or receiver. Such vulnerabilities are easily identifiable.

The characterization system that accompanies the XT-30 allows for the collection of cell I-V curves and the calculation of related parameters, such as fill factor and efficiency as well as temperature-related information.

Figure 3-31: Spectrolab XT-30 in the SUNLab at the University of Ottawa.

3.1.2.2 External Quantum Efficiency (EQE)

The SUNLab's External Quantum Efficiency (EQE) measurement system was designed and built by a fellow Ph.D. student, Olivier Thériault. An EQE, or equivalently, a spectral response measurement system is an extremely important tool when studying devices designed to absorb light such as solar cells. The measurement consists of counting the number of electrons that are collected at the device terminals and finding the ratio between this number and number of photons that are incident on the active area. EQE measurements tell cell designers how efficiently the materials in their devices are absorbing photons, identifying material composition and quality. In a multijunction solar cell the combined EQEs of all the subcells in a device is the primary measure of how well the device is optimized to harvest a particular solar spectrum.

An EQE measurement of a quantum-dot-enhanced triple-junction solar cell designed and manufactured by Cyrium Technologies Inc. is shown in Figure 3-32. This measurement is one of the defining inputs to the system model presented in Chapter 4 and will be discussed further at that time. A more thorough discussion of this measurement is found in Appendix B.

In the figure we see three quantum efficiency curves which together represent the absorption properties of the triple junction cell. The high energy edge of the top subcell falls off for energies approaching the bandgap of InGaP but the slope of the absorption edge is governed by the thickness of the top subcell. In this case the top subcell is thin enough that a small percentage of the photons just greater than its bandgap energy travel through the top subcell and are absorbed by the middle subcell. The portion of the spectrum that is transmitted by the top subcell is now available for absorption in the middle subcell. The blue end of the spectrum has already been absorbed which governes the slope of the high energy edge of the middle subcell EQE. Layers of quantum dots in the middle subcell help extend the low energy EQE edge of the middle subcell to lower energy to shift some of the excess current in the bottom cell to the middle cell. This is done to optimize the current matching conditions for a given spectrum. Finally the remaining photons above the energy of the Ge bottom cell are absorbed. The wide wavelength range for which photons are absorbed in the bottom cell is a result of the fact that Ge has a bandgap that is lower energy than would be optimal in combination with the materials currently used in the top two subcells.

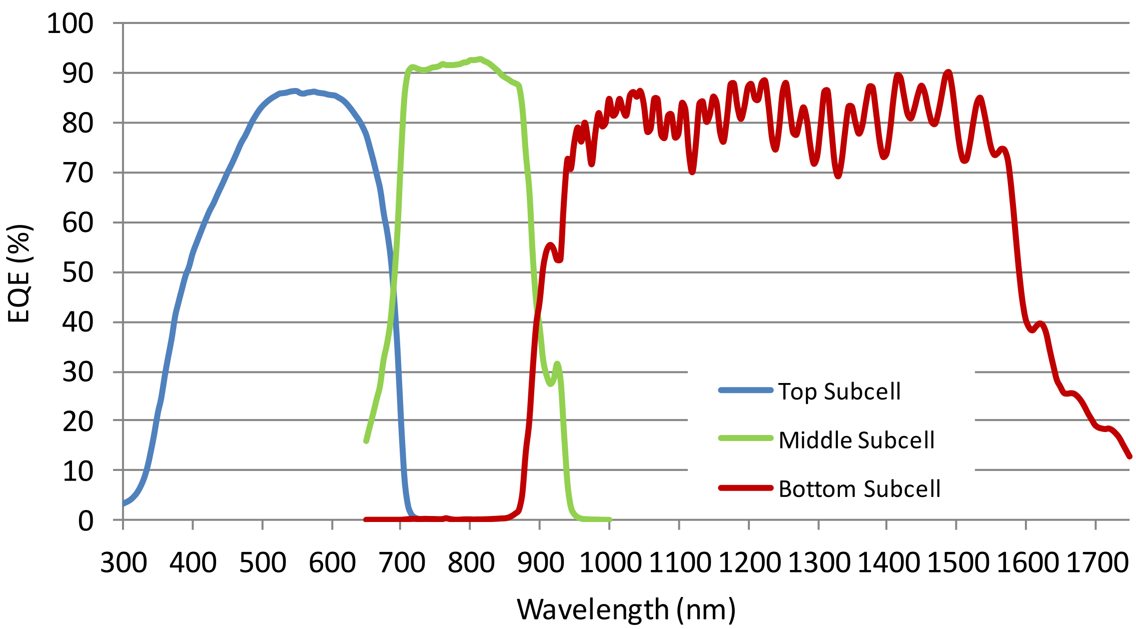

Figure 3-32: EQE measurement of a quantum-dot-enhanced triple-junction solar cell designed and manufactured by Cyrium Technologies Inc. Absorption peak in the middle subcell due to quantum dot layers is visible on the long wavelength edge of the middle subcell EQE. Absorption edge is effectively pushed down to ~950 nm.

4 CPV System Model

Once the monitoring system was complete and the first performance data for the SUNRISE demonstrator became available it became evident that it was necessary to have a means of making some basic calculations to determine what performance should be expected from the demonstrator. A prediction of the expected system performance would provide a baseline to which the measured system performance could be compared. To satisfy this need a system model was developed in order to determine how various aspects of a CPV system affect its overall performance. The model relies on the following inputs:

- Spectral irradiance curves to account for changes in the solar resource due to air mass variation over a given day in a particular location
- Solar cell quantum efficiency to describe the absorption properties of the cells themselves
- Optical transfer function (OTF) of the concentrating optics to quantify any changes in the spectral distribution of the light on-route to the solar cell
- The cell temperature
- The concentration ratio

Based on the inputs listed, and the equivalent circuit model of a single triple junction solar cell as described in Section 2.2 and Figure 2-7, the model is able to show how various quantities such as Isc, Voc, Imp, Vmp, power output and system efficiency vary over a day. It should be noted that predicting system performance based on calculations made for a single representative solar cell inherently assumes that either all cells in the system are behaving identically.

The accuracy of the model is directly related to the accuracy of the inputs. The spectral irradiance and the external quantum efficiency are measured quantities that are relied upon in order to predict the performance of the system. The optical transfer function (OTF) of the concentrating optics is not well known and will also have a significant effect on the light that actually gets to the cell. An OTF simulated using ZEMAX optical design software for the concentrating optics used in the SUNRISE demonstrator was used in the simulations presented here.

The models predictive power is also limited by the accuracy of the cell parameters that are specified in order to generate the solar cells I-V characteristics. These parameters were extracted by fitting simulated I-V curves to measures I-V curves. I-V curves of Cyrium triple junction cells were measured in the SUNLab for this purpose.

4.1 System Model Design and Functionality

The following steps outline theoretical principles applied to simulate the performance of a CPV system. The model was implemented in MATLAB.

4.1.1 Subcell Short Circuit Current

The first step in the system model is to calculate the photo current density produced by each subcell given the spectrum of incident light and the quantum efficiency of each subcell. Equation 20 is the theoretical expression used to calculate the photo current density (J_{sc}) of a single junction solar cell,

$$J_{ph} = q \cdot \int \frac{I(\lambda)}{E_{ph}} \cdot Tr(\lambda, T) \cdot IQE(\lambda, T) d\lambda , \tag{20}$$

where $I(\lambda)$ is the spectral irradiance, $E_{ph}(\lambda)$ is the photon energy, $Tr(\lambda,T)$ is a transmission function which includes the optical OTF of the module optics, $IQE(\lambda,T)$ is the internal quantum efficiency and q is the elementary charge. It should be noted that both $Tr(\lambda,T)$ and $IQE(\lambda,T)$ potentially depend on temperature in addition to wavelength. An approximation to this equation will be used for the rest of this discussion because in the laboratory we have measured external quantum efficiency (EQE) instead of internal quantum efficiency. Thus, since losses due to reflection are already incorporated into the EQE measurement this no longer needs to be accounted for in the transmission function. As shown in equation 21 an optical transfer function (OTF) that only accounts for the effects of the concentrating optics can be used replacing the transmission function above.

4.1.2 Spectral Input

The calculation is complicated by a couple of factors. First, the spectral irradiance $I(\lambda)$ changes as the air mass changes throughout the day. Thus the calculation must be performed for each spectrum in a representative set of spectra for a given day in a given location. Two such sets of spectra for Ottawa (45.45°N, 75.62°W) on or near the summer solstice are given for comparison in Figure 4-1 and Figure 4-2.

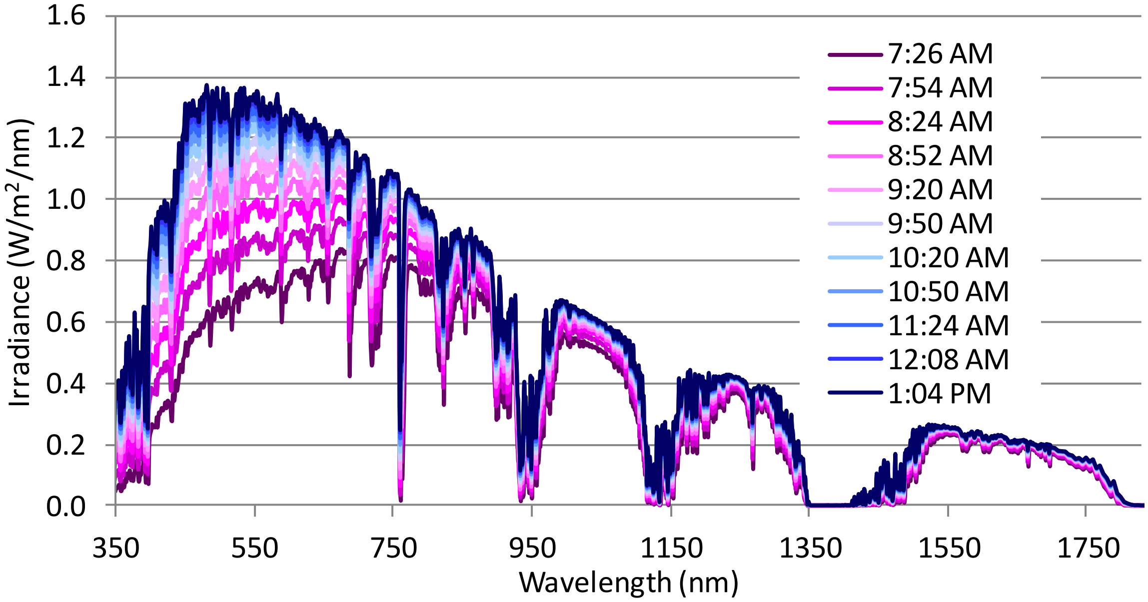

Figure 4-1: SMARTS2 simulated direct spectra during the day on the summer solstice in Ottawa, Canada.

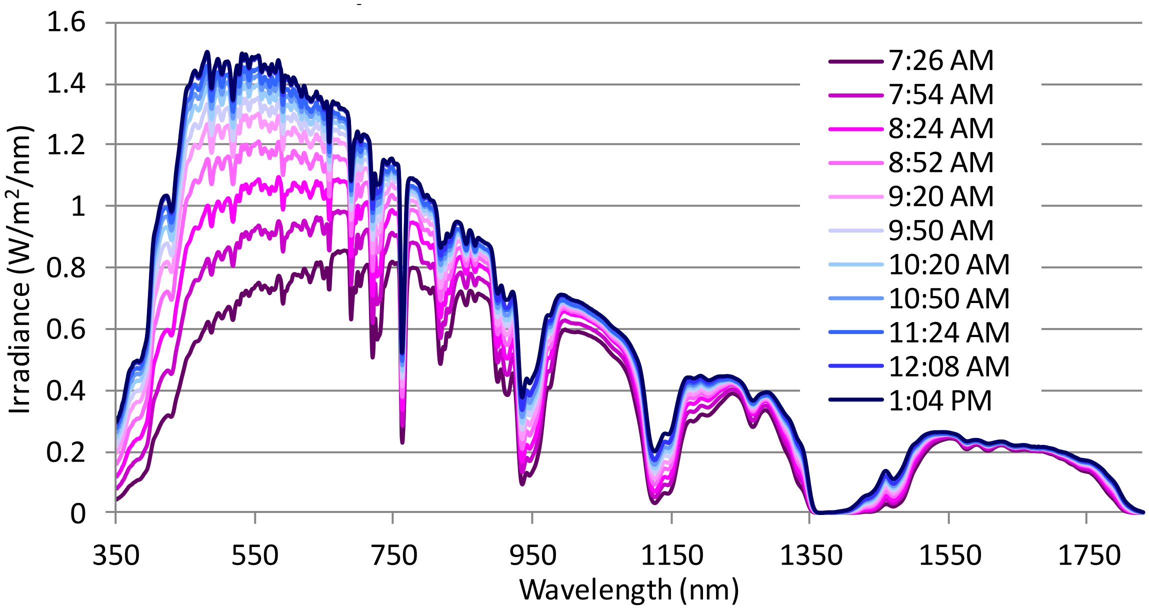

Figure 4-2: Measured direct spectra on June 18th, 2011, three days before the summer solstice in Ottawa, Canada.

There are differences between the simulated spectra and the measured data. The measured data for example exhibits higher peak irradiances at wavelengths that are blue shifted relative to the SMARTS2 simulated peaks. These differences stem from the fact that we have not established confidence in the local atmospheric data required to use as input to the SMARTS2 software. Thus while the SMARTS2 software provided an excellent first approximation upon which to build the system model, in order to ensure the model accurately represents the field performance of a system measured spectra should be used as input.

That said, the SMARTS2 software allows the simulation of spectra that correspond to any desired air mass value. It is thus possible to simulate spectra for very high air mass values when the sun is close to the horizon which are difficult to measure without a very clear vantage point of the horizon. For this reason, simulation results in Section 4.1 will be based on SMARTS2 spectra so that the trends can be analyzed over a larger range of air mass values.

4.1.3 Optical Transfer Function

Second, the spectral irradiance of the insolation is not precisely the same as what strikes the solar cell. Rather, it must be modified by a transmission function that describes all of the spectral changes that occur as the light interacts with the concentrating optics and is coupled into the solar cell.

It is sometimes difficult to determine precisely what light enters the solar cell. This is largely due to the fact that the various components of the optical train are not easy to isolate. As a first approximation, equation 21 was used in the model,

$$J_{ph} = q \cdot \int \frac{I(\lambda)}{E_{ph}} \cdot OTF(\lambda) \cdot EQE(\lambda, T) \cdot d\lambda \, , \tag{21}$$

where $OTF(\lambda)$ is the temperature independent optical transfer function of the two stage Fresnel based concentrating optics and $EQE(\lambda,T)$ is the temperature dependent external quantum efficiency of the solar cell. In general the external quantum efficiency (measured with normally incident light) cannot be assumed to be independent of the angle of incident light (θ) in a Fresnel based system in which concentrated light strikes the cell as a large range of angles (~0-30°). However, the necessary adjustment in the calculation can simply be coupled into the OTF until more accurate measurements of the temperature dependant and angularly dependent optical train can be made in the future.

4.1.4 External Quantum Efficiency

The temperature dependence of the external quantum efficiency is governed by the Varshni model [51] which describes the change in semiconductor bandgap energies with temperature. The Varshni relation is given by equation 22,

$$E_g(T) = E_g(0) - \alpha \frac{T^2}{T + \beta} \, , \tag{22}$$

where $E_g(0)$ is the bandgap of the semiconductor at 0K, T is the temperature of the semiconductor in Kelvins and α and β are material dependent constants. The material dependent constants used in the current analysis, specified in Table 4, were taken from the literature [52], [55], [56] where they were determined through experimental calibration of the Varshni relation.

Table 4: Summary of Varshni parameters used to implement the temperature dependent external quantum efficiency of a triple junction solar cell.

Varshni Parameters	$E_g(0)$	α	β
Units	eV	eV/K	K
Top subcell (InGaP)	1.879	6e-4	350
Middle subcell (GaAs)	1.519	5.405e-4	204
Bottom subcell (Ge)	0.75	4.77e-4	235

The resulting temperature dependent EQE is shown in Figure 4-3 where the measured EQE is compared to the simulated EQEs at 5°C,15°C,50°C and 75°C. The normalized AM1.5D standard spectrum is plotted in the background for convenience.

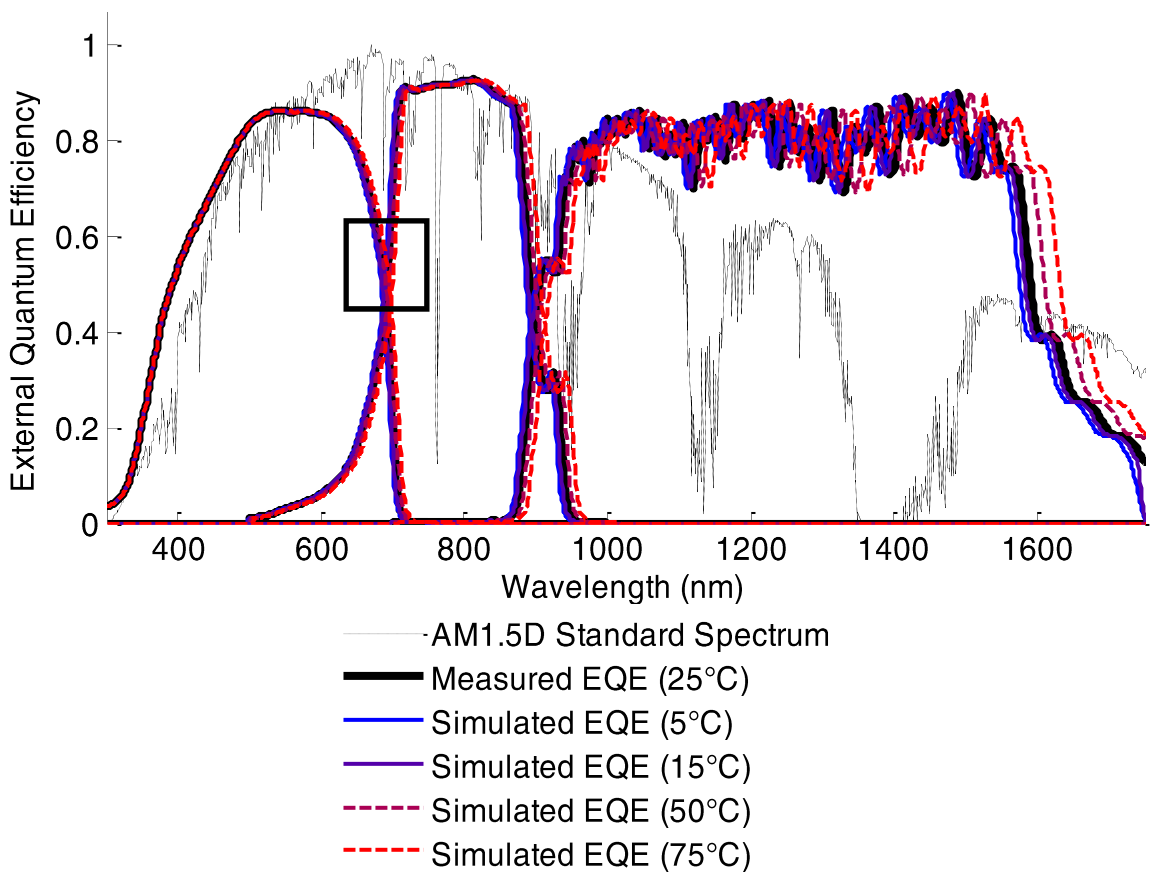

Figure 4-3: Temperature dependent external quantum efficiency of a triple junction solar cell implemented using the Varshni model. Legend applies to expanded plot of highlighted window shown in Figure 4-4 as well.

The temperature dependent EQE was calculated by starting with an EQE measurement taken at 25°C and then shifting the EQE edges in energy to reflect the effect of a change in temperature on the material. The amount of shift was dictated by the change in the bangap energy which was calculated using the Varshni Model. Figure 4-4 shows a blow up of the area in the square in Figure 4-3. This is a portion of the EQE at the bandgap edge of the top subcell. At 50% EQE the high energy cutoff of the middle subcell EQE is also visible. The same legend as in Figure 4-3 also applies to Figure 4-4. Here we can see the horizontal shift in the EQE that occurs when the bandgap of the semiconductor material changes. The dashed lines are for temperatures above 25°C and the thin solid lines are for temperatures below 25°C. The thick black line is the original measurement at 25°C.

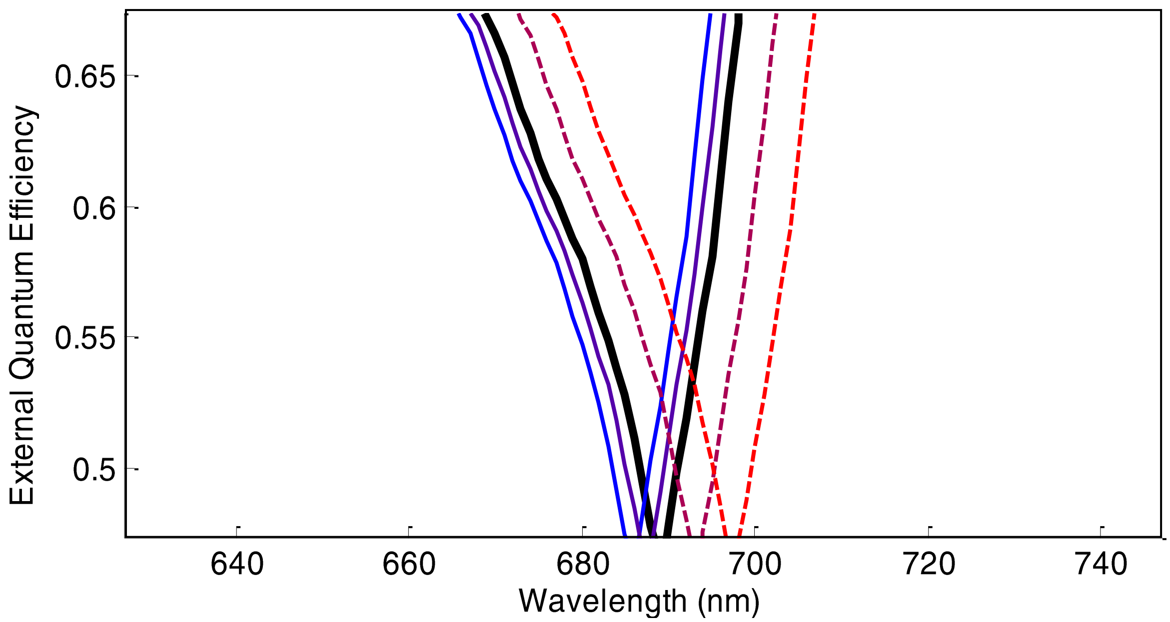

Figure 4-4: Temperature dependent external quantum efficiency of a triple junction solar cell at the bandgap edge of the InGaP top subcell at the 50% threshold where absorption is cut off from the GaAs middle subcell. Legend presented in Figure 4-3.

4.1.5 Daily Variation in Subcell Current

With an optical transfer function (OTF) and a temperature dependent external quantum efficiency EQE it is possible to calculate the subcell short circuit currents using equation 21. Figure 4-5 shows a visual break down of the entire calculation performed in equation 21. The OTF shown in this figure was simulated by OPEL Solar for a two stage Fresnel based optic like the one shown in Figure 1-11 using ZEMAX. The dips in the transmission curve centered at ~1200 nm and ~1375 nm are due to the absorption properties of the lens material. The simulation results are limited in range due to the lack of available material parameters for wavelengths longer than 1700 nm and shorter than 350 nm.

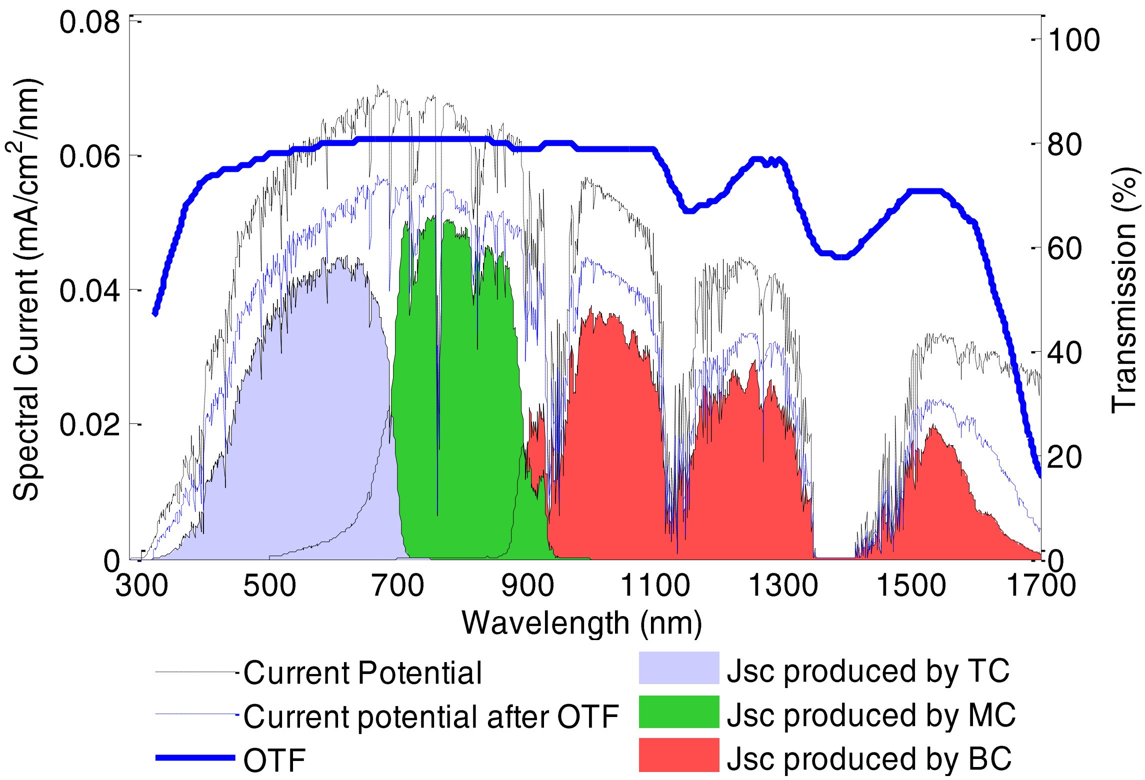

Figure 4-5: Subcell currents for the ASTM G173 AM1.5D standard spectrum, a ZEMAX simulation of the OTF of a two stage Fresnel based concentrating optic and the EQE of a triple junction solar cell. Note: Overlapping areas are transparent to the outline of area plots.

Figure 4-5 clearly shows the relative magnitude of current losses resulting from the concentrating optics verses those due to the absorption properties of the cell itself. The most intense spectrum in the figure plotted in black is simply the AM1.5D standard solar irradiance divided by the photon energy to get the photon flux and multiplied by the elementary charge to get the current per nm that could potentially be harvested. The second slightly lower spectrum is simply the former plot multiplied by the OTF of the concentrating optics. Thus the loss, due to the specified OTF, in the amount of current per nm that can potentially be harvested is the difference between these two curves. The current potential after the OTF just described is then multiplied by the EQE of the solar cell to get the three curves that are filled blue, green, and red which represent the current harvested by the top middle and bottom subcells respectively at each wavelength. The integrated areas under these curves (the filled areas) represent the photo currents produced by each subcell.

4.1.6 Generation of Light-Current-Voltage Curves

The coloured areas in Figure 4-5 represent the photo currents (J_{ph}) produced by each subcell. So if these values are calculated for each of a number of spectra that correspond to the geometrical air mass (AM) values experienced during a given day, they may be used, in conjunction with a cell temperature and parasitic resistance values, to generate a set of light-current-voltage curves that describe the solar cell operation during that day. These cell parameters must be substituted into equation 23 and the equation must be solved numerically since the cell current is not easily isolated in the equation.

$$J = J_{ph} - J_o\left[\exp\left(\frac{q(JR_s + V)}{nk_BT}\right) - 1\right] - \frac{JR_s + V}{R_{sh}} \tag{23}$$

Figure 4-6 shows such a set of IV curves generated for each subcell. The darker the line the lower the air mass for which the IV curve was calculated. Notice that the middle subcell with an open circuit voltage of 1.2 V has the smallest short circuit current at solar noon of just over 6 A. Thus for low air mass values (which occur in the middle of the day) the middle subcell limits the performance of the cell.

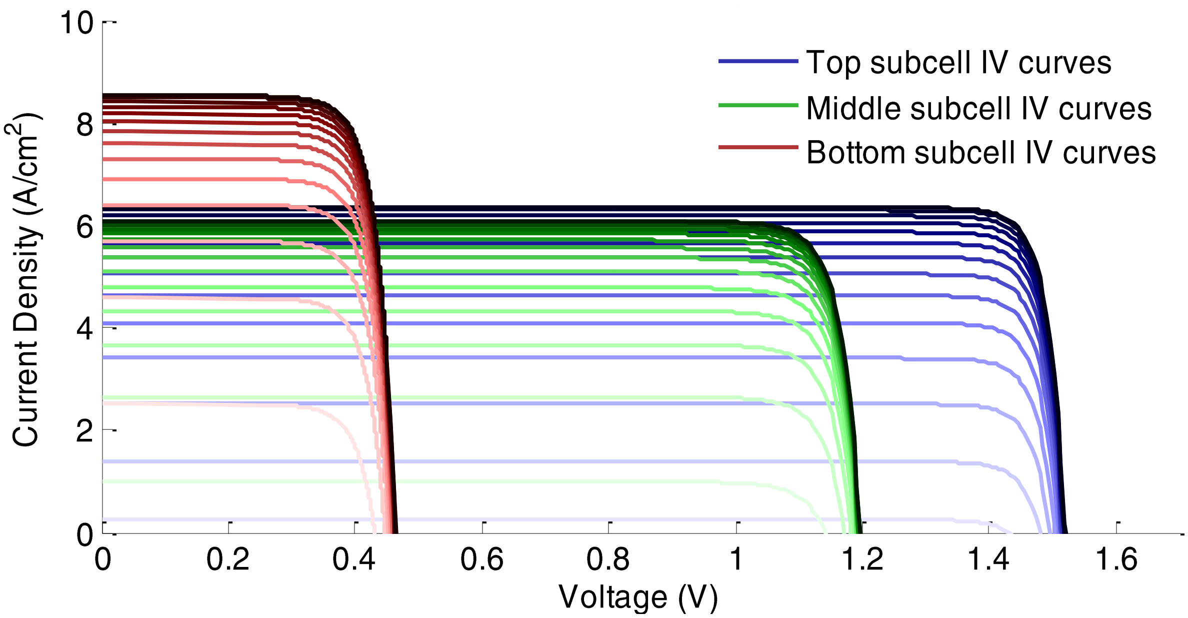

Figure 4-6: Subcell IV curves for representative daily spectra. The IV curve with the highest short circuit current for each subcell was calculated for the AM1.08 spectrum which is the highest point the sun reaches in Ottawa. Current density calculations assume 500x concentration.

4.1.7 Daily Variation of Current, Voltage, Power & Efficiency

It is more telling to look at the short circuit currents of the IV curves in Figure 4-6 plotted against the geometric air mass and the time of day at which these air mass values occur. The simulated subcell photo currents (equivalent to short circuit currents in this case because parasitic resistances are negligible) are shown in Figure 4-7 along with the corresponding efficiency curve. The efficiency at each air mass is calculated by first adding the three subcell IV curves in series to achieve a single set of IV curves for the triple junction cell during a given day. The maximum power point on the triple junction IV curve is then determined and that power is divided by the incident light power to determine the DC conversion efficiency. The triple junction IV curves and the corresponding power curves are shown in Figure 4-8 and Figure 4-9.

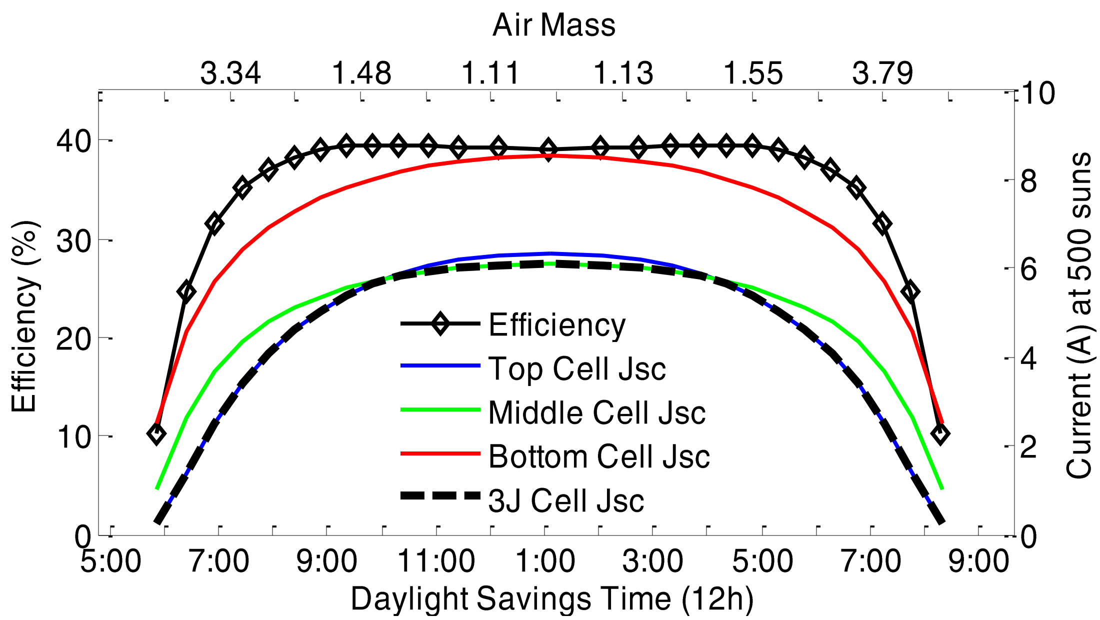

Figure 4-7: Simulated subcell short circuit currents and system efficiency throughout the day based on measured spectra on June 18th, 2011 assuming a perfect optical transfer function and a cell temperature of 25°C.

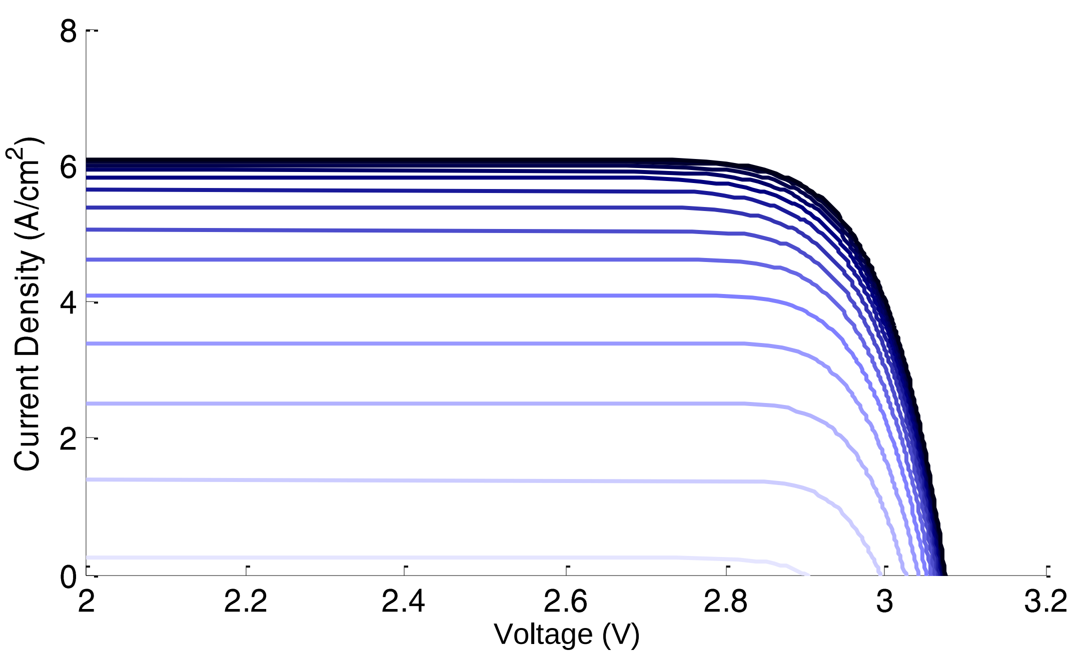

Figure 4-8: Triple junction current density curves simulated as a function of voltage. The highest (darkest) current density curve shown in the figure was calculated for the AM1.22 spectrum which is the highest point the sun reaches in Ottawa.

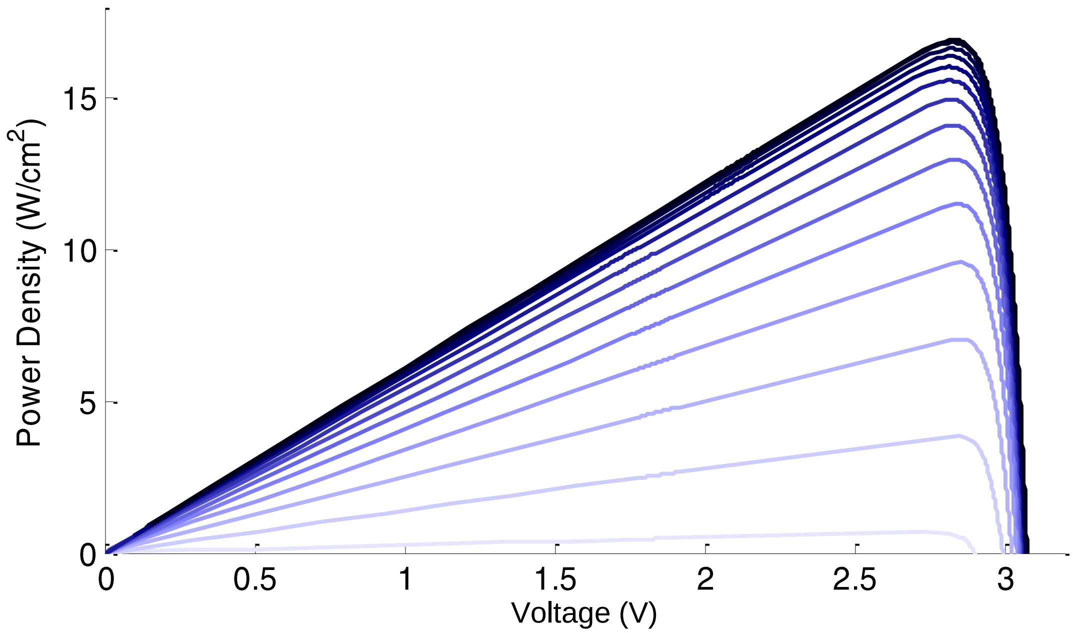

Figure 4-9: Triple junction power density curves as a function of cell bias voltage simulated within the system model over the course of a day. The highest (darkest) power density curve shown in the figure was calculated for the AM1.22 spectrum which is the highest point the sun reaches in Ottawa.

Once triple junction IV curves have been simulated any number of parameters that can be calculated from an IV curve can be plotted over the course of a day. Figure 4-10, Figure 4-12 and Figure 4-13 show the current and voltage at the maximum power points and the fill factor over the course of the day respectively.

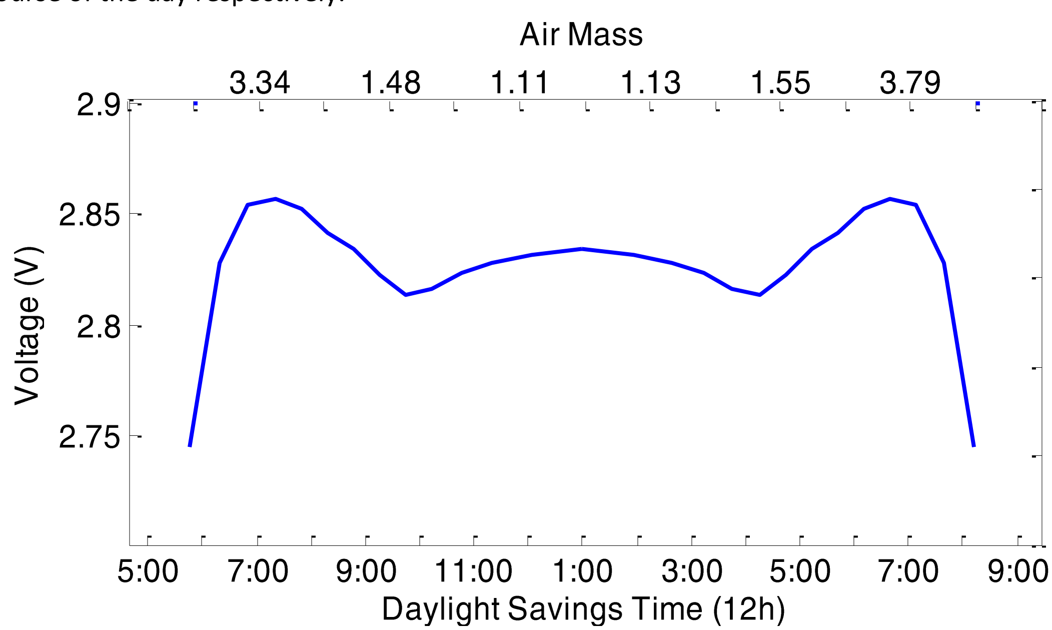

Figure 4-10: Voltage at the maximum power point throughout the day.

One might think that the plot of the voltage at the maximum power point throughout the day should highlight the fundamental increase in efficiency that results from increased intensity like the open circuit voltage does as shown in Figure 4-11. This would be true except that the fact that the spectrum is also changing significantly which means that the logarithmic increase in voltage due to increasing intensity is counteracted by a decreasing fill factor at some points during the day.

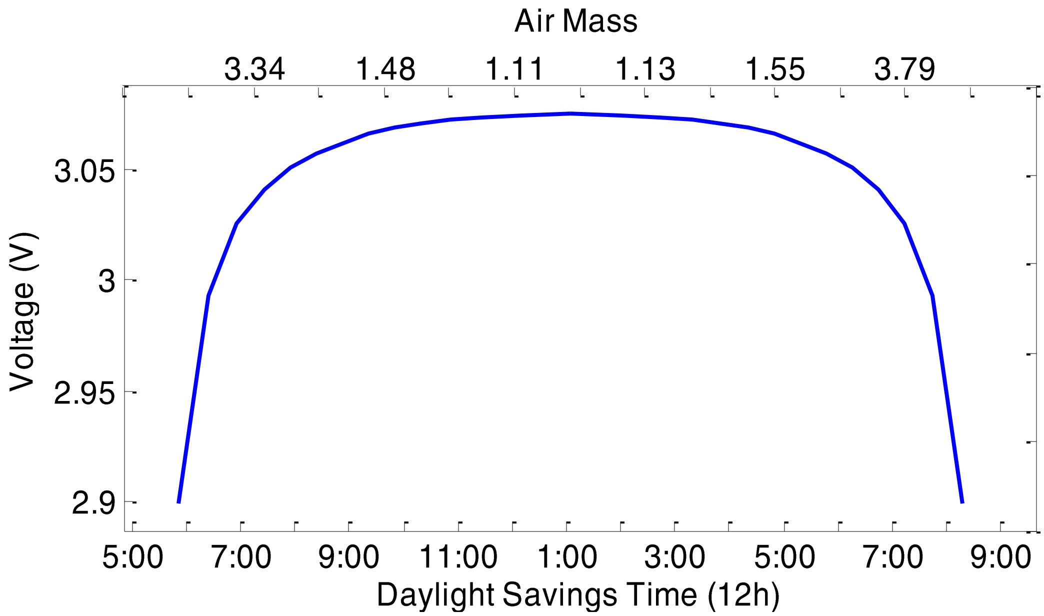

Figure 4-11: Open circuit voltage throughout the day. The open circuit voltage increases logarithmically with intensity resulting in a fundamental increase in efficiency with increasing intensity.

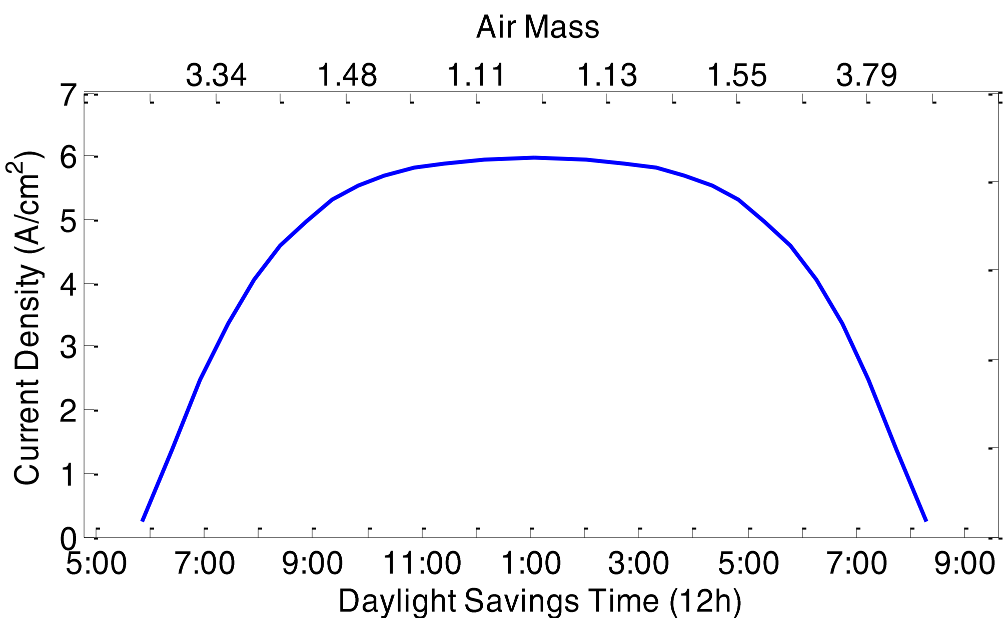

Figure 4-12: Current at the maximum power point throughout the day.

The current at the maximum power point scales almost linearly with the DNI but not exactly. Due to the fact that the maximum power point moves around as the subcell short circuit currents shift relative to each other, the current at the maximum power point does not follow exactly the same trend as the DNI and the short circuit current.

The fill factor is a particularly interesting parameter to follow throughout the day. In a single junction solar cell the goal is always to maximize the fill factor because it is a measure of how ideally the cell is operating. In a multijunction cell however, power output is maximized when all subcells are perfectly current matched and because the subcell IV curves are added in series the fill factor will necessarily be at a minimum at this point. This is easily understood if one visualizes the addition of two identical IV curves in series. If they have the same photo currents then when summing the voltages the resulting IV curve will have a slower exponential behavior than if one of the IV curves in the sum has a higher photo current than the other. If one of the IV-curves has a much larger photo current, adding the IV curves means adding a nearly constant voltage to the IV curve with the smaller photo current. The exponential in this case is almost the same as each individual IV-curve was in the first place. The slower exponential behavior corresponds to a lower fill factor because there will be a greater difference between I_{sc}, V_{oc} and I_{mp}, V_{mp} respectively.

Thus while the goal is still to maximize the fill factor of each individual subcell in a triple junction cell, the minimum(s) in a plot of the fill factor for different air mass values shows the point at which the cell is optimized. Thus, the dips in a plot of the fill factor vs the air mass values that occur over a day represent the points at which the best current matching is achieved and in turn where the peak efficiencies occur.

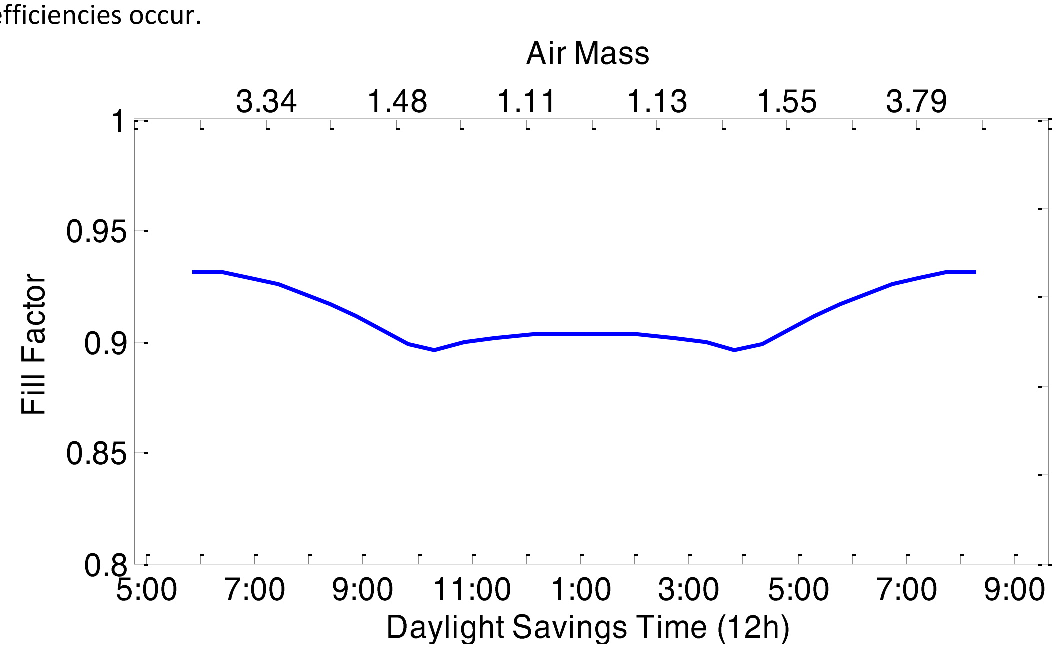

Figure 4-13: Fill factor of the IV curves throughout the day.

The simulation described in this section made use of SMARTS2 simulated spectra and assumed a perfect OTF and a constant operating temperature of 25°C in order to isolate the effect of air mass variation throughout the day. In Section 0 spectra measured on June 18th are used in a simulation of the SUNRISE demonstrator in which an optical transfer function is applied and the effects of temperature are considered.

4.2 Calibration of Solar Cell IV Characteristics

In order to build a model with true predictive power, the model must first be calibrated such that it is able to predict well characterized quantities with sufficient accuracy. In this case, this means that the system model must be able to accurately calculate the short circuit current of a representative triple junction solar cell and subsequently predict the IV curve of the solar cell given the short circuit current and a temperature.

In order to achieve this, a two diode model of each subcell was implemented. [57] Once calibrated to a specific solar cell this model is capable of generating an IV curve for a cell under any illumination and at any temperature.

The subcell IV curves were generated by solving for the current density (J) in equation 24.

$$J = J_{ph} - J_s\left[\exp\left(\frac{q(JR_s + V)}{n_s k_B T}\right) - 1\right] - J_r\left[\exp\left(\frac{q(JR_s + V)}{n_r k_B T}\right) - 1\right] - \frac{JR_s + V}{R_{sh}} \quad (24)$$

where J_{ph} is the photo current which is almost equal to the short circuit current as long as parasitic resistances are insignificant, J_s, J_r, n_s and n_r are the saturation current, recombination current, saturation emission coefficient (or ideality factor of n = 1) and the recombination emission coefficient (or ideality factor of n = 2) respectively, R_s and R_{sh} are series and shunt resistances respectively, q is the elementary charge, k_B is Boltzmann's constant and T is the temperature of the cell.

In this equation the dark current is divided into two components to simulate two distinct regimes in an IV curve. The recombination term dominates at currents near the short circuit current of the solar cell and the more ideal behavior of the saturation term dominates for currents far from the short circuit current. Figure 4-14 shows the effect of the superposition principle in this equation.

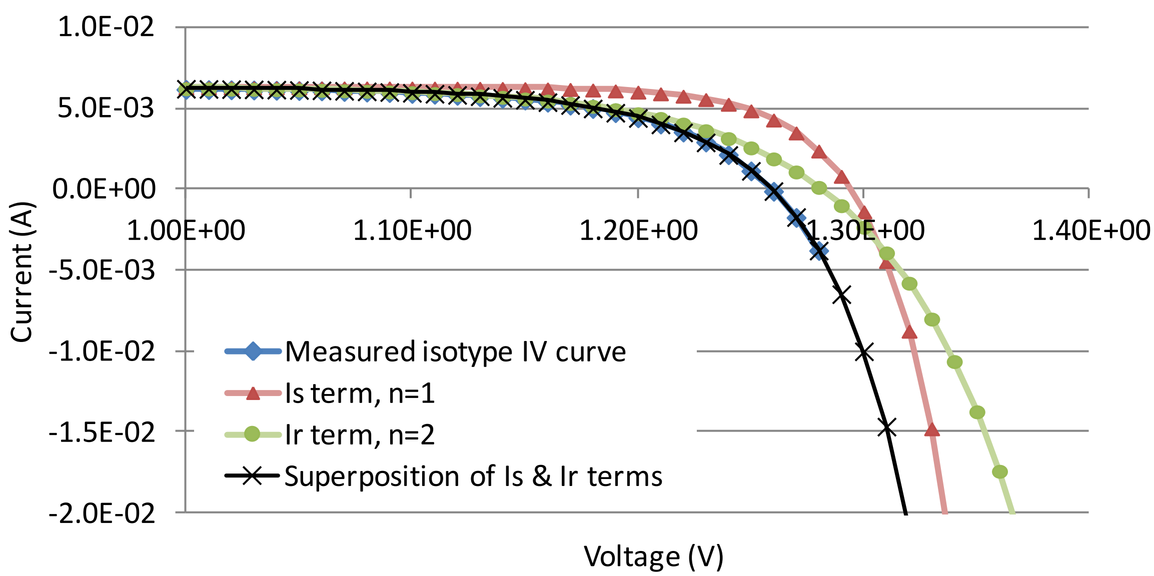

Figure 4-14: The two diode model of a single junction solar cell or subcell. The saturation and recombination terms exhibit ideality factors of 1 and 2 respectively. The figure shows how the superposition of these terms allows the recreation of a measured IV curve.

Fortunately, J_s, and J_r are related by the following temperature dependent expressions.

$$J_s(T) = J_s(T_{nom})\left(\frac{T}{T_{nom}}\right)^{\chi} \exp\left(-\frac{q}{k_B}\left(\frac{E_g(T)}{T} - \frac{E_g(T_{nom})}{T_{nom}}\right)\right) \tag{25}$$

$$J_r(T) = J_r(T_{nom})\left(\frac{T}{T_{nom}}\right)^{\frac{\chi}{2}} \exp\left(-\frac{q}{2k_B}\left(\frac{E_g(T)}{T} - \frac{E_g(T_{nom})}{T_{nom}}\right)\right) \tag{26}$$

where T_{nom} is a reference temperature, T is the cell temperature, χ is the temperature exponent, q is the elementary charge, k_B is Boltzmann's constant, E_g is the bandgap energy of the semiconductor and $E_g(T_{nom})$ is the bandgap energy at the reference temperature.The temperature exponent can be extracted from temperature dependent isotype IV measurements, an exercise which is beyond the scope of the current discussion. The results of the calibrations are presented in Figure 4-15 and Figure 4-17.

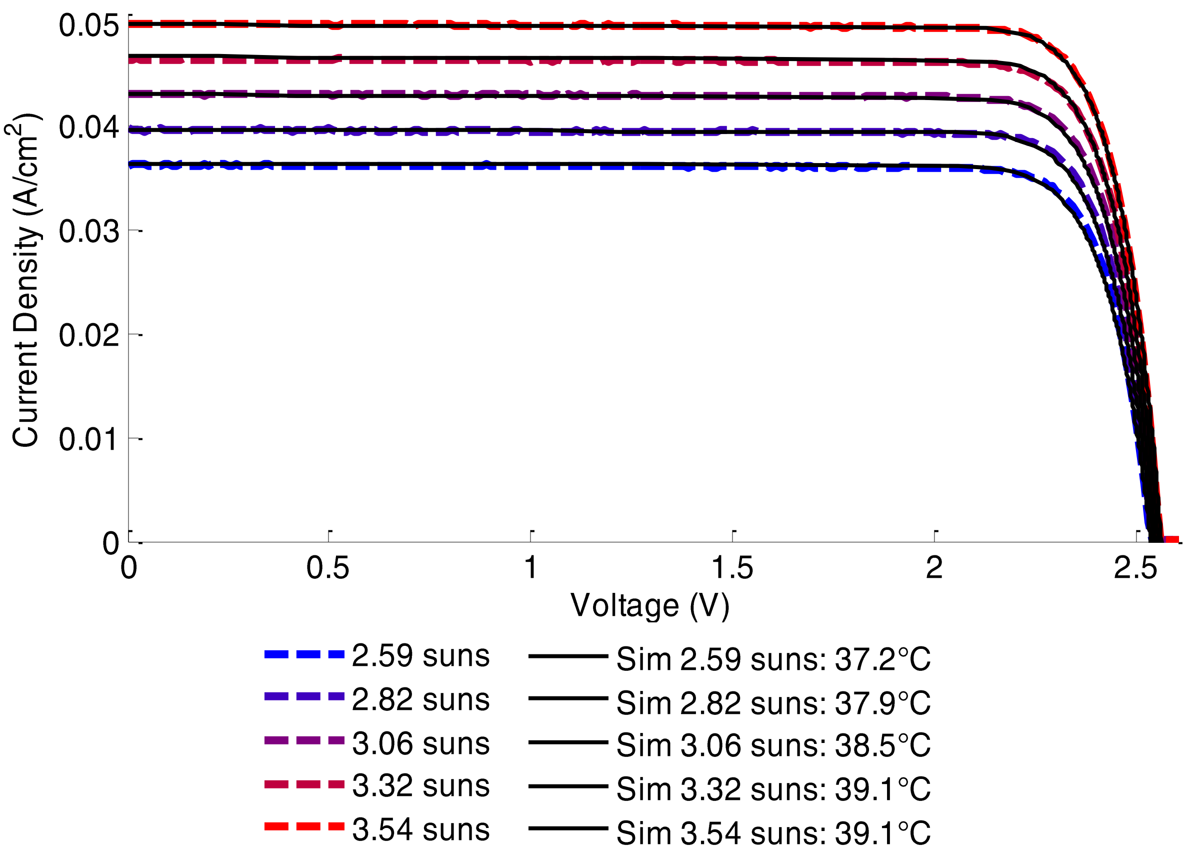

Figure 4-15: Calibration over intensity. The black solid lines are simulated curves. These curves overlay the measured curves which are plotted with dashed lines. The measured data represent the IV curves of a chip-on-carrier. The triple junction III-V semiconductor solar cell (Cyrium 2395E) was measured in the SUNLab under the Oriel solar simulator at lamp powers of 1300W, 1395W, 1490W, 1595W and 1680W which correspond to the intensities listed in the figure where 1 sun is defined as 1000W/m^2. The junction temperatures used in the simulation are also listed in the figure.

Figure 4-15 shows the IV calibration over intensity. IV curves were measured in the SUNLab for a chip-on-carrier device under the Oriel solar simulator. The spectrum of the Oriel solar simulator which was used in the system model to generate the simulated IV curves is shown in Figure 4-16. It was assumed for the purposes of this calibration that the spectrum does not change as the lamp power is adjusted to scale the intensity. This is not strictly true as a slight blue shift does occur as the lamp power is increased. A better calibration could be achieved if this shift was well characterized and implemented in the system model.

It is immediately obvious that the spectra plotted in Figure 4-16 do not look like the measured spectra plotted in Figure 4-2. It is very difficult, in fact, to simulate the solar spectrum in the laboratory. Artificial suns are necessary however so that during the development process it is not necessary to fully package solar cells in completed modules before they can be tested. The differences between the xenon spectrum and the solar spectrum have a minimal effect on the performance of the cell if the photo currents in each subcell can be adjusted in the laboratory so that they are the same under the xenon lamp as they are under real sunlight.

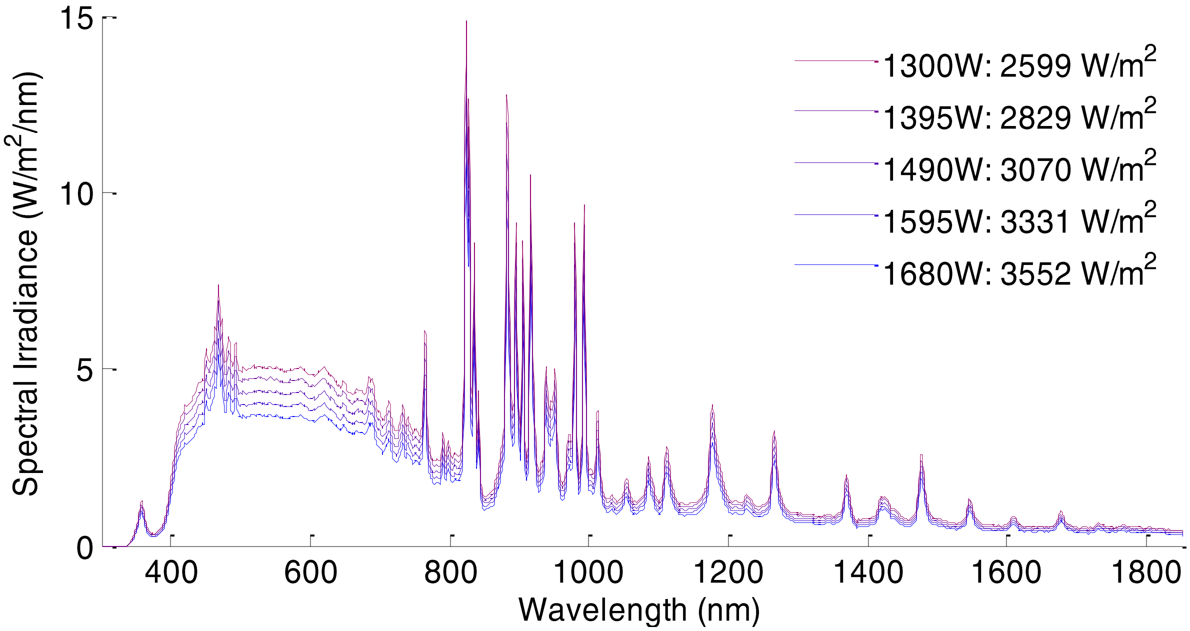

Figure 4-16: Oriel solar simulator spectrum. Intensity spikes between 800nm and 1000nm are characteristic of xenon lamps due to the intrinsic transitions in the gas. Notice the apparent difference between the Oriel spectrum and the solar spectra shown in Figure 4-2. In the legend the first number given is the lamp power of the solar simulator and the second power given is the intensity measured using a reference cell for which the short circuit current at 1 sun (1000 W/m^2) is known.

Figure 4-17 shows the IV calibration over temperature. These dark IV curves were measured in the SUNLab for a chip-on-carrier device very similar to the one used for the intensity calibration. Dark curves (as opposed to IV curves measured while the cell is illuminated) were used for the temperature calibration for two reasons. First, a thermoelectric cooler under the test stage was used to control the temperature of the cell. When the cell is illuminated from above a temperature gradient is established from the surface of the cell to the temperature sensor in the test stage. Thus the cells junction temperature is difficult to determine with accuracy when the cell is illuminated.

The second and more fundamental reason for performing a temperature calibration with dark curves is that this is the only way to know precisely the relative positions of the individual subcell IV curves without having to know the spectrum of the light illuminating the cell. In the dark, one can be certain that they all have a short circuit current of exactly zero Amperes. Accurate spectral measurements of the solar simulators output are difficult to make owing to the high intensity of the lamp light, the changes in the spectrum as the lamp power is varied, and the cumulative aging of the lamp itself. Thus this element of complexity should be avoided if possible.

This is extremely important when calibrating a model of a triple junction cell because under illumination if all three subcells are not perfectly current matched the subcell IV curves shift relative to each other which changes the shape and fill factor of the resulting triple junction IV curve.

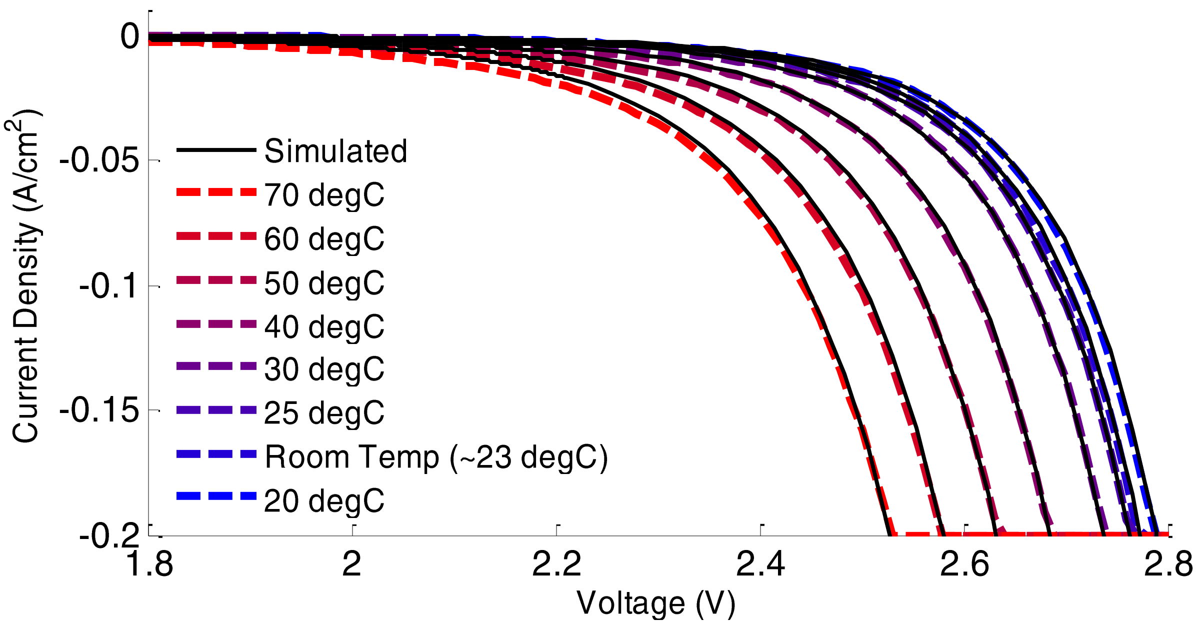

Figure 4-17: Calibration over temperature. The black solid lines are simulated curves. These curves overlay the measured curves which are plotted with dashed lines. The measured data represent the dark IV curves of a chip-on-carrier. The triple junction III-V semiconductor solar cell (Cyrium 2244C-3c) was measured in the SUNLab on a temperature controlled test stage.

The last part of the calibration that needs to be discussed is the determination of the series and shunt resistance. As a first approximation the effects of series resistance have been neglected. While the system model is capable of simulating series and shunt resistances for each subcell the experimental work necessary to determine these values is left for future work at this time. Both series and shunt resistance should be determined by fitting the subcell IV-curves to measured subcell IV curves. Unfortunately, isotypes of cells similar to those in the SUNRISE demonstrator were not available and determining the series and shunt resistance of cells from another manufacturer would not necessarily have been particularly representative.

The isotypes used for the temperature dependant calibration were manufactured by Spectrolab and provided an estimate of the parameters necessary for calibration to the Cyrium cells in the demonstrator. The parameters determined with the Spectrolab isotypes were the saturation currents (I_s), the recombination currents (I_r), and the temperature exponents (X) of the three subcells. The values determined for the Spectrolab isotypes were then adjusted slightly in order to fit triple junction IV curves of Cyrium solar cells (measured in the SUNLab and shown in Figure 4-15 and Figure 4-17) that are representative of the IV curves of cells used in the SUNRISE demonstrator.

4.3 Modeling the SUNRISE Demonstrator

Now that all of the components of the system model have been described it is time to analyze the performance of the SUNRISE demonstrator. We will start with the same Cyrium solar cell EQE that has been used so far but this time instead of using SMARTS2 simulated spectra we will use measured spectra and model the performance of the demonstrator on June 18th, 2011. Simply replacing the SMARTS2 spectra with measured data makes quite a difference as one can tell by comparing Figure 4-18 with Figure 4-7.

The optimum air mass values (indicated by the intersection of the top and middle subcell short circuit currents and the dips in the fill factor plot over a day) for instance have shifted from ~1.4 to ~1.5. Since the cells were designed by Cyrium Technologies for optimal performance under the AM1.5D spectrum this suggests that the input file used in the generation of SMARTS2 spectra for Ottawa was not as accurate as it could have been. Our measured spectra, however, give us much closer to what we expect. The peak system efficiency is now at an air mass of just over 1.5 as indicated by the dips in fill factor shown in Figure 4-19.

The concentration ratio specified is now calculated based on the dimensions of the optical aperture and not the quoted concentration ratio of 550x for the module. Thus since the optical aperture is 607.5cm^2 and the solar cell is 1cm^2 the concentration ratio used will be 607.5 times. If all of the light that strikes the optical aperture is not concentrated on the solar cell then this will be reflected by a decrease in system current and a corresponding decrease in system efficiency because the optical aperture of the concentrating optics is the area used to calculate the measured system efficiency of the SUNRISE demonstrator as presented in Figure 4-18.

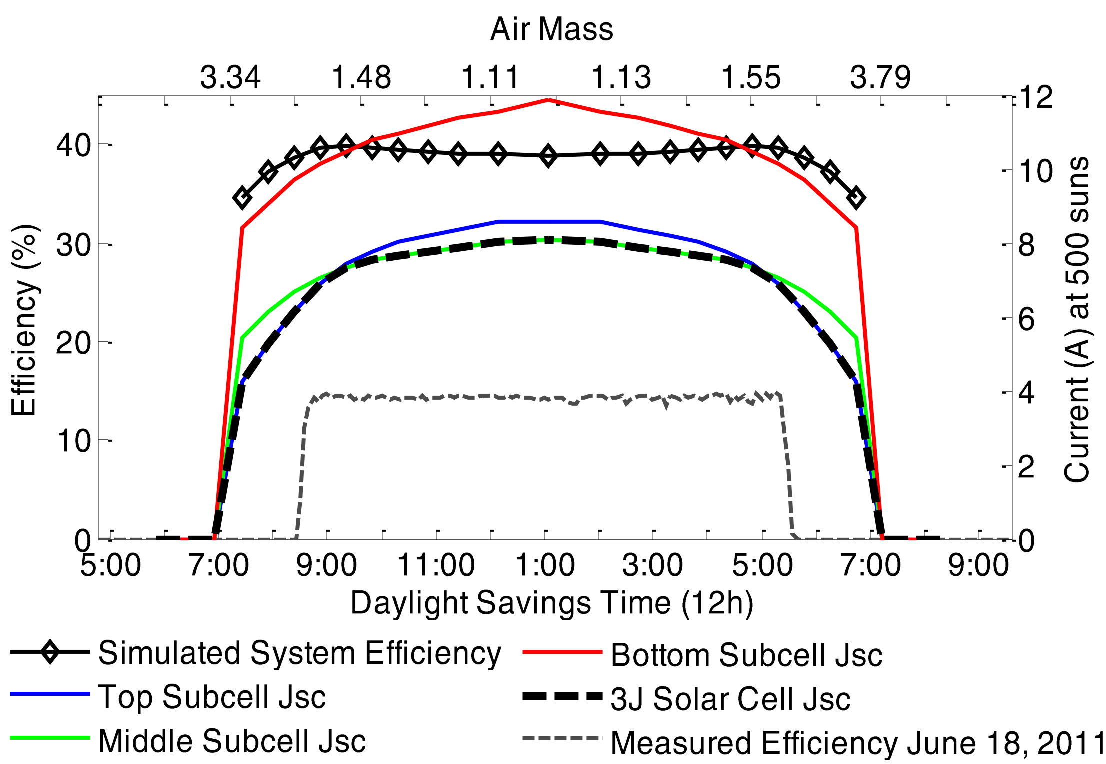

Figure 4-18: System efficiency and subcell short circuit currents simulated for a perfect OTF and an operating temperature of 25°C.

Another observation is that the short circuit currents predicted are much higher than the max power currents measured on the demonstrator which are shown throughout the year in Figure 3-20 and Figure 3-21. We will look at the maximum power currents and voltages calculated in the simulation once all of the system components are included to see if it is a reduction in the current or a reduction in the voltage or some combination of the two that accounts for the system efficiency exhibited by the SUNRISE demonstrator.

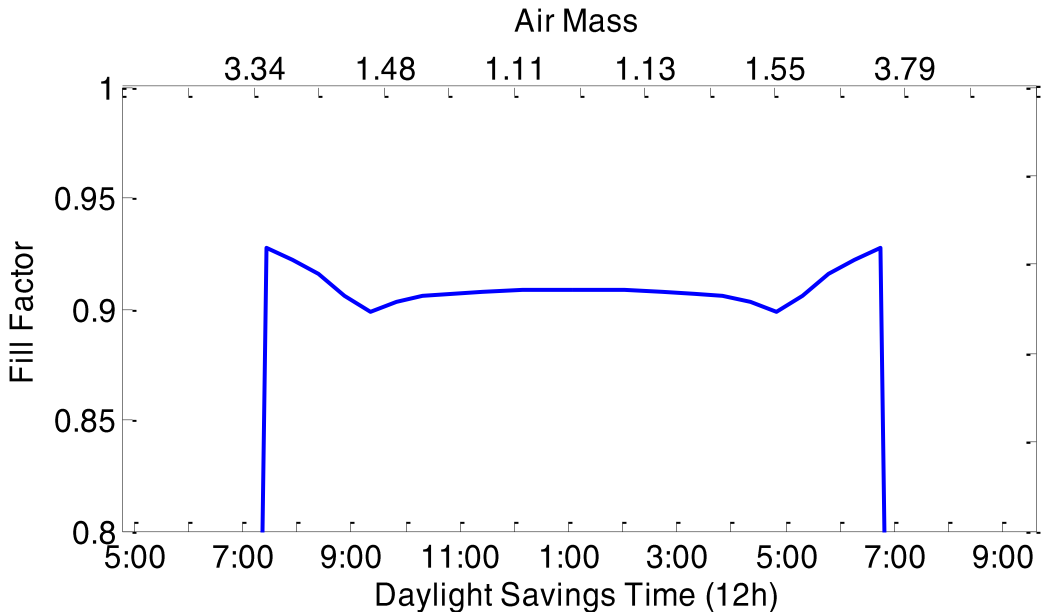

Figure 4-19: Fill factor of solar cell IV curves plotted over a single day. Simulated with measured spectra, a perfect OTF and an operating temperature of 25°C.

The next step is to add in the optical transfer function of the concentrating optics. Figure 4-20 shows the effect of the OTF on the system efficiency. The OTF has the largest effect on the bottom cell short circuit current but since the bottom cell is never current limiting, this has little effect on the overall system performance. The OTF also reduces the short circuit current of the top subcell which does have an effect. As the top subcell short circuit current plot shifts downward in Figure 4-20 with respect to the middle subcell curve, the intersection points move inward toward lower air mass values. As confirmed in Figure 4-21, the optimal air mass for the system is now 1.4.

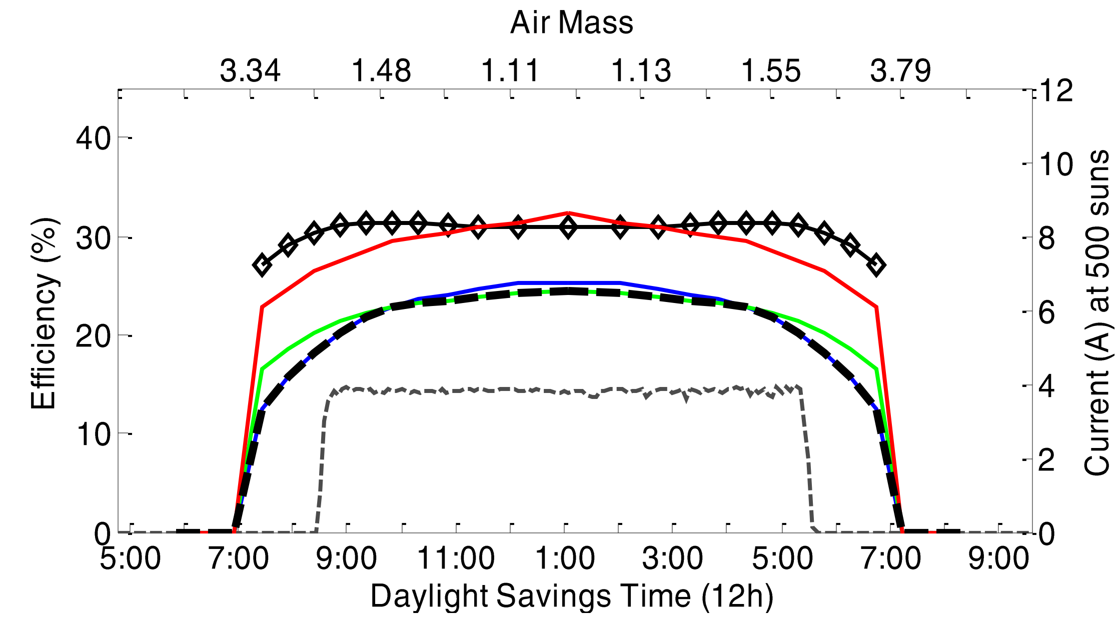

Figure 4-20: System efficiency and subcell short circuit currents simulated for a ZEMAX simulated OTF and an operating temperature of 25°C.

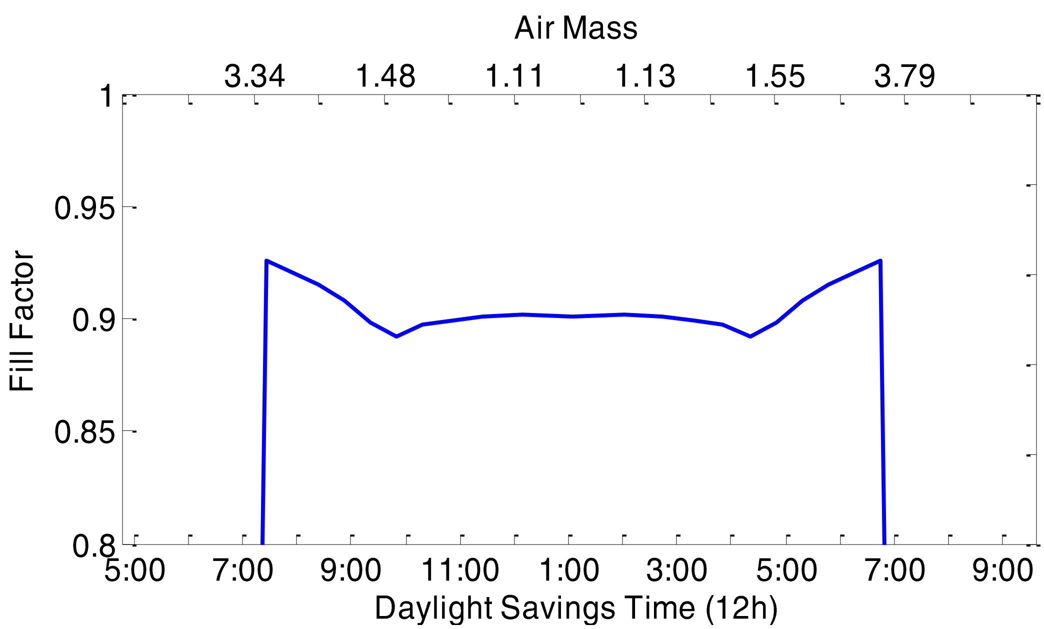

Figure 4-21: Fill factor of solar cell IV curves plotted over a single day. Simulated with measured spectra, ZEMAX simulated OTF, and an operating temperature of 25°C.

To this point it has been assumed that the cell temperature has been constant at 25°C which is a severe approximation. On June 6th, the temperature in Ottawa ranged from 16°C at 7:00am to 27°C in the early afternoon. First, we will assume that the modules are operating at a temperature of ambient plus 40°C to try and simulate practical operating conditions. The results are presented in Figure 4-22.

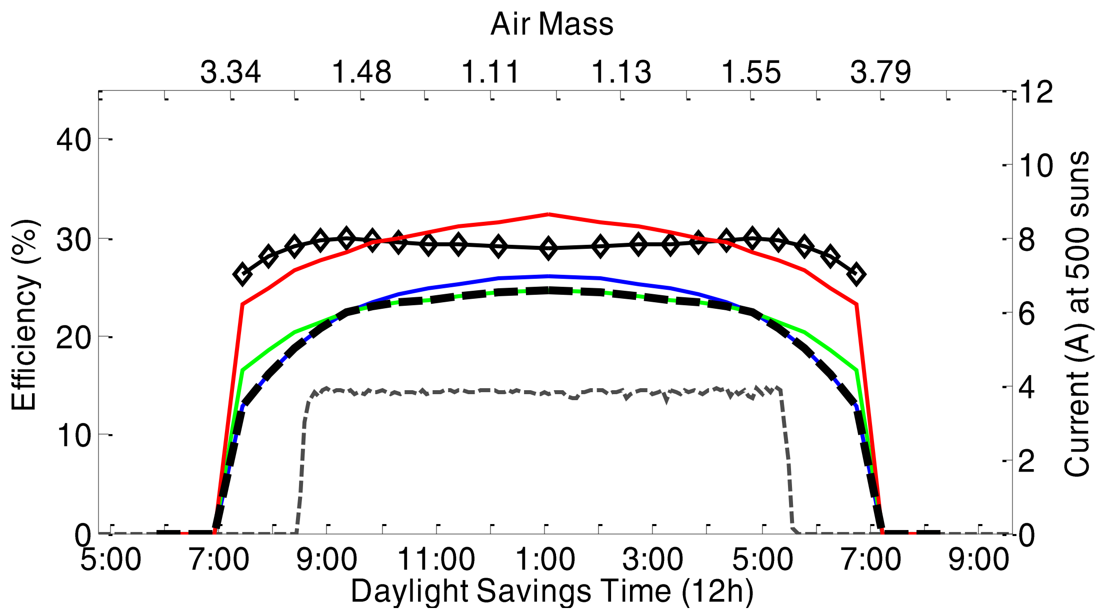

Figure 4-22: System efficiency and subcell short circuit currents simulated for a ZEMAX simulated OTF and an operating temperature of ambient plus 40°C on June 18th, 2011.

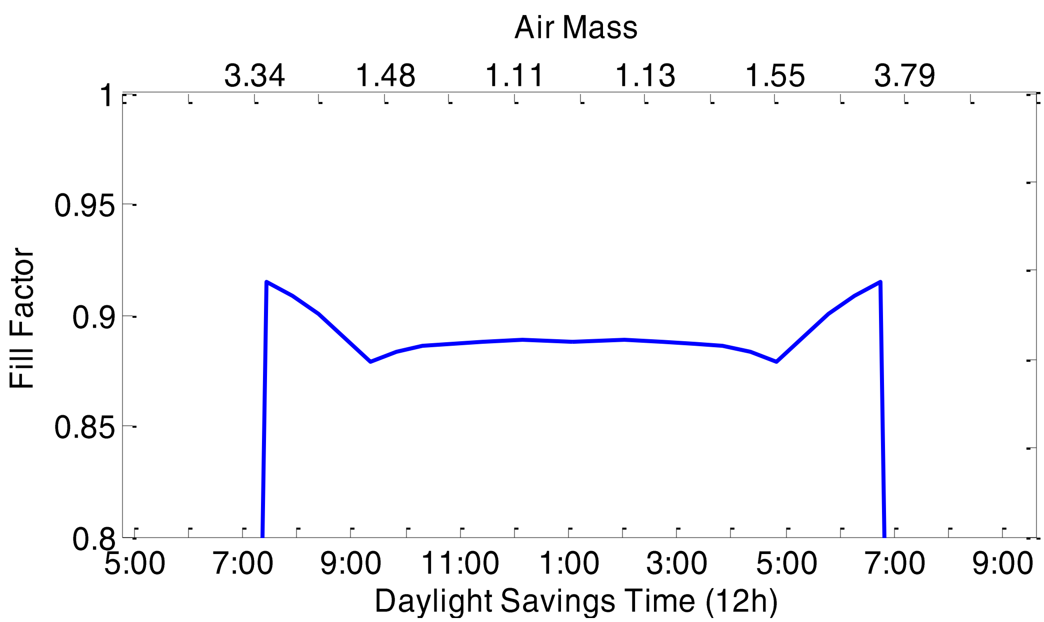

Figure 4-23: Fill factor of solar cell IV curves plotted over a single day. Simulated with measured spectra, ZEMAX simulated OTF, and an operating temperature of ambient plus 40°C on June 18th, 2011.

At this temperature the peak simulated system efficiency is sitting at 29.6%. Another observation can be made as well. The increased operating temperature has caused enough of a shift in the semiconductor band edges to change the current balance in the solar cell an appreciable amount. The optimal system air mass is now back at approximately 1.5 (confirmed in Figure 4-23) as it was before the OTF was considered because the increased temperature acted to reduce the semiconductor bandgap energies increasing the number of photons that could be captured by the top subcell, and shifting the absorption windows of the middle and bottom subcells to higher wavelengths. The effect is that the current produced in the top subcell has increased relative to the current in the middle subcell moving optimal performance towards a higher air mass value.

Finally, it is possible to try and determine how much of the degradation of the demonstrator's efficiency is due to heating of the cells. If we simulate the system efficiency at a temperature that results in the same average voltage (voltage at maximum power) per cell as the demonstrator had on June 18th then we will be able to determine the maximum amount of the efficiency degradation that could be due to a temperature induced decrease in system voltage.

The average cell voltages at the maximum power point in October, 2010 and September, 2011 were 2.45 V and 1.92 V respectively, calculated by dividing the sum of the string voltages presented in Figure 3-17 and Figure 3-18 by the total number of cells on the demonstrator. The maximum power point voltage at the hottest temperature in the last simulation (ambient + 40°C = 67°C) was 2.62V, and we find according to Figure 4-24 that a junction temperature of 85°C results in a maximum power point voltage of just under 2.45V in the middle of the day.

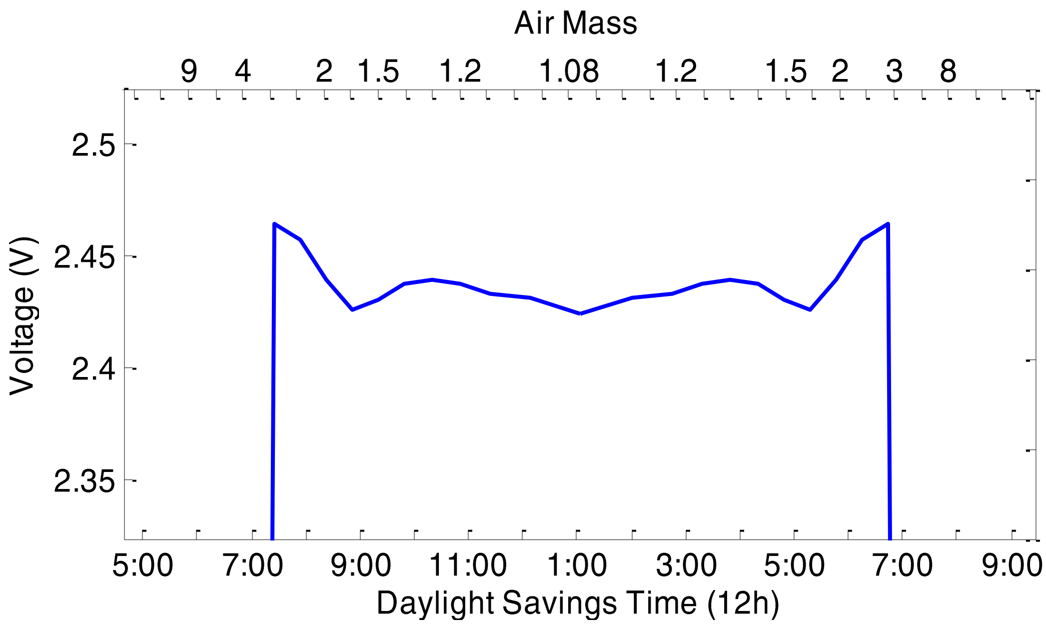

Figure 4-24: Cell voltage at the maximum power point simulated for an operating temperature of 85°C on June 18th, 2011.

However, as shown in Figure 4-25 the maximum system efficiency remains at almost 30%. The 45°C increase in temperature caused a 170 mV decrease in the voltage at the maximum power point but only a 1.8% (absolute) decrease in the efficiency. We will come back to the effect of temperature on the system voltage in a moment but first it seems appropriate to look at the current. It is clear that the low system current in the SUNRISE demonstrator shown over the year in Figure 3-20 and Figure 3-21 is much lower than the short circuit currents shown in Figure 4-22 and Figure 4-25. The maximum power point currents in the last two simulations were 6.4 A/cm^2 and 6.5 A/cm^2 respectively, the current actually increasing slightly when the temperature increased.

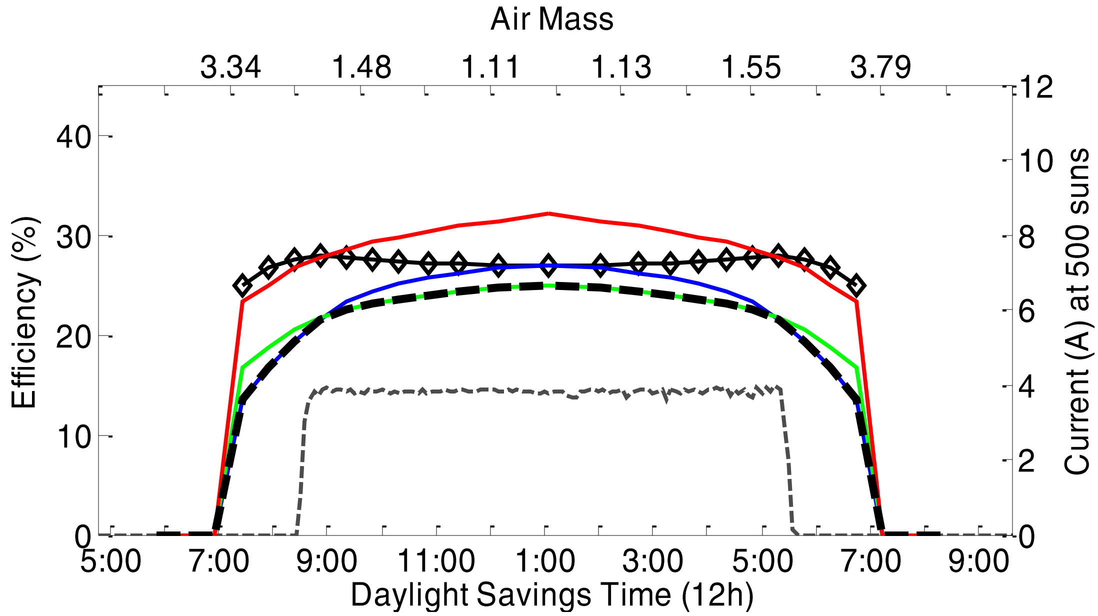

Figure 4-25: System efficiency and subcell short circuit currents simulated for an operating temperature of ambient plus 85°C on June 18th, 2011.

The system current is a function of the incident light and the absorption properties of the solar cell so we will consider these. If the quantum efficiency of the cells changed over time in the system this could result in a reduction in current. Any loss of light as it passes through the concentrating optics in front of the cell would also result in current loss. Since the optical transfer function is simulated and has not been measured to this point as the EQE has, this seems to be the most reasonable place to start looking for lost current. Misalignment of components in the optical train as well as tracking error would also result in light missing the solar cell which would means system current would be lower than expected. Detailed analysis of these issues is left for future work but for now it is possible to determine what the precise effect of lost light would be on the overall system performance. Figure 4-26 shows the effect of a 50% transmission spectrally flat filter (across all wavelengths) on the system performance.

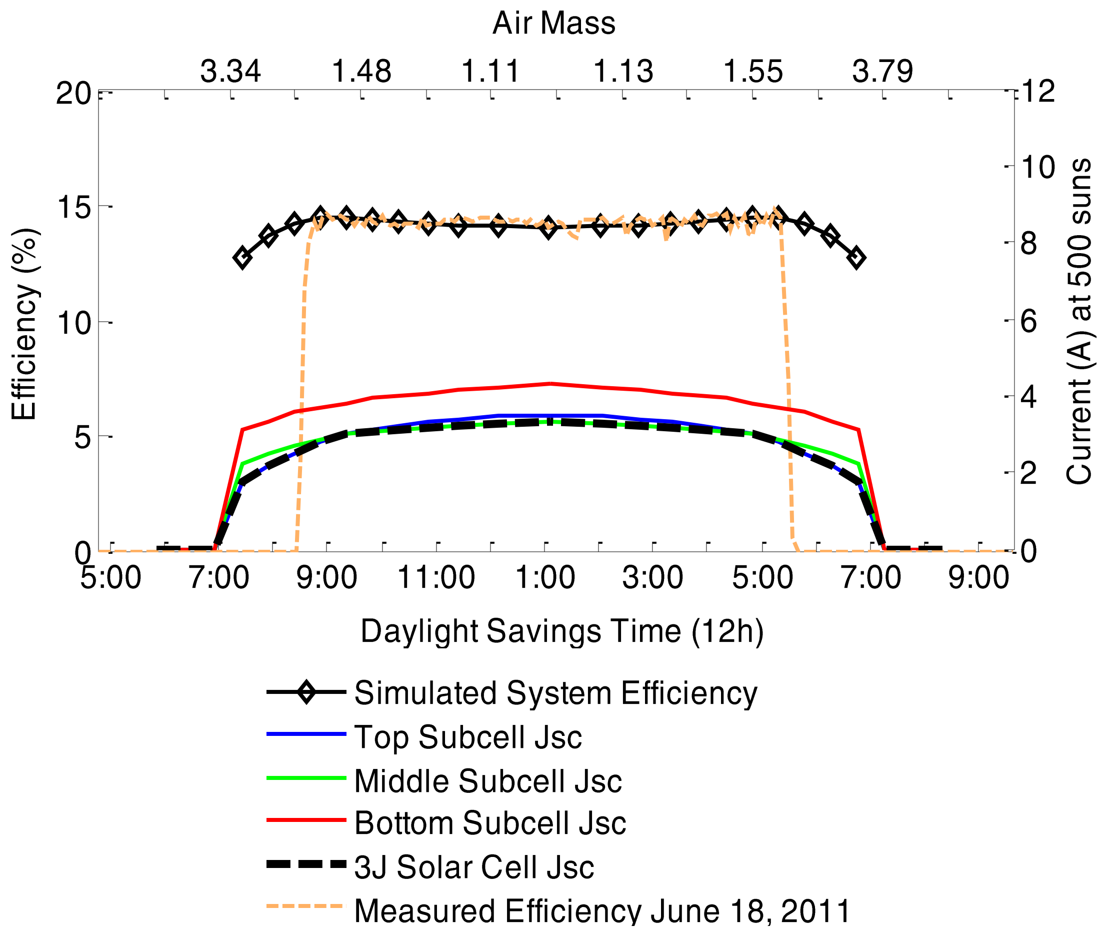

Figure 4-26: System efficiency and subcell short circuit currents simulated for an operating temperature of ambient plus 40°C and a flat 50% optical filter on June 18th, 2011.

This results in an efficiency that is approximately what we measure on June 18th, 2011 but the maximum power voltage in the middle of the day is 2.57 V which is still significantly higher than the average cell voltage at the demonstrator on the same day (~1.97 V). The shape of the simulated efficiency curve matches the measured curve within the noise of the efficiency measurement as one can see more clearly in Figure 4-27. Also the simulated cell current (3.4 A in the middle of the day) is ~1 Amp less than that measured on the demonstrator on June 18th which was about 4.2 A in the middle of the day.

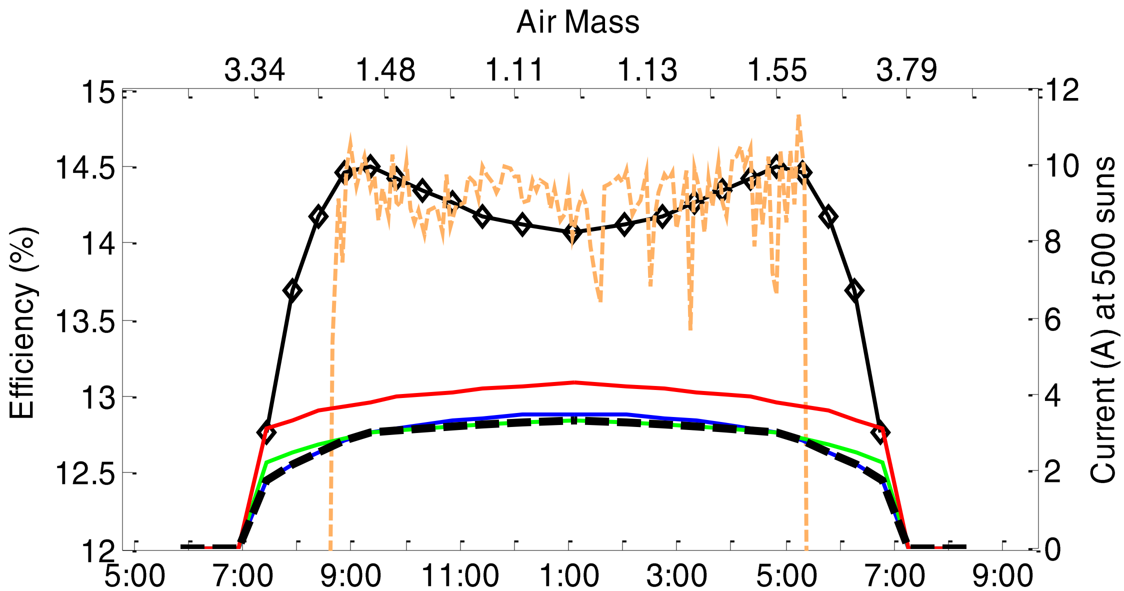

Figure 4-27: A closer look at the measured and simulated system efficiency curves. Subcell short circuit currents are also shown for the simulation of an operating temperature of ambient plus 40°C and a flat 50% optical filter on June 18th, 2011.

Perhaps a combination of increased cell temperature and light loss can explain the demonstrators performance the best. Figure 4-28 shows the results of a simulation that attempts to achieve this. The current and voltage at the maximum power point in the simulation are the same as the average current and cell voltage measured on the demonstrator on June 18th. To achieve this, the cell temperature was simulated at 167°C above ambient and a flat filter transmitting only 64% across all wavelengths was applied.

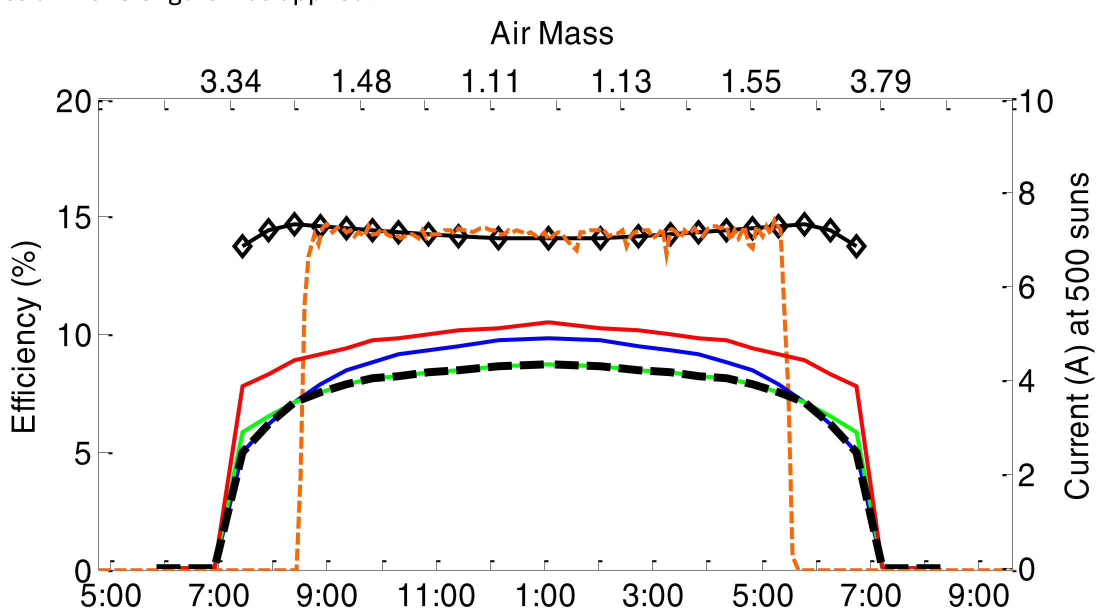

Figure 4-28: System efficiency and subcell short circuit currents simulated for an operating temperature of ambient plus 167°C and a flat 64% transmission optical filter on June 18th, 2011.

The efficiency of the simulated curve matches that of the measured curve for June 18th, 2011 over the portion of the day that the demonstrator was pointed at the sun. Recall, however, that due to restrictions on the azimuthal range of the tracker it was not pointed at the sun when the sun was more than 90° from due south. The shape of the efficiency curve could be matched much more closely if the modules were on sun when the efficiency of the modules peaked. This was the case on October 9th 2010 as shown in Figure 3-25 but not for June 18th 2011.

It should be noted that this analysis assumes the cells are all approximately the same and that none of them have been damaged. There is however evidence to the contrary concidering the decrease in voltage shown in Figure 3-17 and Figure 3-18 which indicates that some cells are no longer contributing to the total voltage of the system but rather are being bypassed.

More investigation is required to determine exactly what is causing the apparent loss of light in the system. Measuring the optical transfer function of the concentrating optics for example would help to resolve this issue. Alignment issues in the optical path to the solar cell and tracking error could also be partly to blame. It should also be noted that a spectrally selective filter reducing only the portion of the spectrum harvested by either the middle subcell or bottom subcell will produce the same net effect as the flat filter applied in the simulation shown in Figure 4-28. Also the temperature of the cell should also be a function of the DNI rather than a constant offset relative to ambient.

Despite these reservations, it is clear that the top subcell is not limiting during the dip in the efficiency during the middle of the day. The fact that the blue end of the solar spectrum is scattered so much stronger than the red end means that as air mass fluctuates the current produced in the top subcell fluctuates more quickly than the currents produced in the middle and bottom subcells. For this reason there is an AM value for which the cell current switches from top cell limited to middle or bottom cell limited. If this transition did not occur we would not see peaks in the system efficiency curve as we do on October 9th 2011.

5 Conclusions

A brief history of the photovoltaic (PV) industry and a discussion about the fundamental benefits of learning how to harvest the solar resource was presented in order to bring into focus a broader perspective on the motivation for the current research. The physical limits of photovoltaic conversion efficiency and the obstacles that must be addressed by engineers were explained.

The economics involved in converting solar energy into electricity, and the current state of the photovoltaic industry worldwide were discussed to point out the challenges that need to be overcome over the next 5 years as the cost of photovoltaic electricity reaches grid parity.

The concentrating photovoltaic (CPV) strategy was rationalized among the various other physical alternatives, and some of the engineering solutions that are currently on the market were reviewed.

The characteristic current versus voltage (IV) curve of a single junction solar cell, the various interesting points on the curve, and the terminology used to describe the IV curve of a solar cell were presented as a foundation for an equivalent circuit analysis of a solar cell. The equivalent circuit of a triple junction solar cell was presented and compared to the physical architecture of a generic triple junction solar cell. Also, the inner workings of a high efficiency triple junction solar cell were explained via a band diagram analysis of simulated solar cell characteristics. This visual explanation provides the basis upon which variations in cell and system performance can be easily understood and explained.

5.1 The SUNRISE Demonstrator, Performance Review

The SUNRISE demonstrator recorded a maximum efficiency of 21.6% (DC efficiency calculated using the optical aperture of the lens within the module) in October 2010. Over the first year of the demonstrator's life the efficiency dropped to an average of about 13% by September 2011.

On its best day (October 9th, 2010) the demonstrator produced 19.2 kWh of the systems total cumulative output to date of 1.8 MWh AC electrical power. This was achieved when the ambient high for the day was 12°C, the peak direct normal insolation (DNI) reached 897 W/m^2 and the humidity was well below the seasonal average.

The low efficiency was a combined effect of both the system current and the system voltage being lower than expected based on laboratory testing of the cells in the demonstrator. In October 2010 the string currents and average cell voltages at the maximum power point were 4.7 A and 2.45 V respectively. By September, 2011 these values had decreased through the sunniest months of the year and were 4.1 A and 1.92 V respectively.

This reduction in system current occurred despite a 15% increase in the maximum DNI on sunny days between the winter solstice on December 21st, 2010 and the spring and summer months (March – September). The decrease in average cell voltage over the course of the year does not seem to scale with the average ambient temperature or the maximum daily DNI during the year although another year worth or data would confirm or deny any such correlation based on annual cycles. This data continues to be collected.

A tracking issue that became evident as of the spring equinox was also analyzed. It was determined that the demonstrator's lack of power production in the morning and evening in the summer months was due to limits on the azimuthal range of the tracker. The limits were defined in the trackers software control system to allow for only 90° of variation on either side of due south. The mechanical limits of the tracker were found to be 104° of variation on either side of due south so that even if a software correction was made to allow for the maximum mechanical azimuthal range, there is still no location around the earth where the tracker would be able to track the sun from sunrise to sunset on the summer solstice.

The accuracy of the DNI measurements made with the pyrheliometer on the SUNRISE demonstrator were analyzed via a comparison to measurements made with a similar instrument on another demonstrator system operated by the SUNLab in Ottawa. The calibrations were compared throughout the year on sunny days when it can be assumed that the difference in insolation between the test sites (which are ~5km apart) is negligible. The calibrations were also compared before and after cleaning which showed that the calibrations compared very well when both pyrheliometers were clean and that soiling of the quartz windows on the pyrheliometers could be responsible for 3-5% reductions in the DNI measurements. Calibration comparisons in the spring seemed to show the most difference between the DNI measurements of the two pyrheliometers which could be due to the presence of pollen and other airborne contaminants that are more prevalent during the spring months. A biweekly cleaning schedule is proposed to keep the pyrheliometers reading within 2% of each other.

The measured daily efficiency curves for the demonstrator were analysed and various artifacts were explained. The effect of tracking issues some mornings on the system efficiency was considered. A comparison between the effects of tracking error and shading in terms of their respective effect on system efficiency was discussed.

The collection of spectra using the spectroradiometer was discussed. Measured spectra were compared to SMARTS2 simulated spectra generated with an input file that included atmospheric data for the Ottawa area. It was discovered that atmospheric data necessary to produce an accurate SMARTS2 input file is difficult to find. The measured spectra calibrated to the total power measured with the pyrheliometer resulted in spectra that had higher total power and were blue shifted relative to the SMARTS2 simulated spectra. The generic input file that is based on average atmospheric measurements over the continental United States used to generate the ASTM standard spectra is a sufficient starting point to demonstrate the spectral variations due to changing air mass that occur during a day.

The equipment in the SUNLab used to measure solar cell optical and electrical characteristics indoors under controlled conditions were described. The necessity for indoor solar simulators was introduced and the capabilities of the artificial suns in the SUNLab were explained. Current – voltage measurements made using these solar simulators as well external quantum efficiency (EQE) measurements made in the SUNLab were used as input to the system model introduced in Chapter 4

A CPV system model was presented as a means of analyzing the performance of the SUNRISE demonstrator and determining the relative impact of system issues on the performance of the system as a whole. The model is based on an equivalent circuit analysis of a triple junction solar cell in which the IV characteristics of each subcell are simulated using a temperature calibrated, two diode single junction cell model. The system model uses temperature dependant EQE based on the EQE of a representative solar cell, the optical transfer function of the concentrating optics, and a set of calibrated spectra that quantify the varying daily insolation as input to calculate the performance of the system over a day.

Simulations calibrated over temperature and intensity, that assume the cells are more or less all behaving the same, suggest that to achieve the currents and voltages measured at the demonstrator, only about 65% of the insolation is actually making it to the solar cells, and the cells are running extremely hot, at temperatures on the order of 170°C above ambient. This does not rule out the possibility that some cells have failed completely and are simply being bypassed. If this is the case a visual check inside a few of the old modules might be informative. This would also mean that the decrease in voltage could be blamed on a few bad cells and that the temperatures of the cells that are still operating might be more reasonable. Regardless, a voltage drop of 25%, and a current drop of 15% over the first year of operation is far greater than what is allowable in a system that needs to operate uninterrupted for 20 to 25 years in order to reach grid parity in the sunniest areas around the world.

The results mentioned above define a clear way forward to determine how exactly to make the most profitable system improvements.

5.2 Future Work

First, a look inside one or a few of the modules that have been on-sun on the SUNRISE demonstrator for the past year is necessary. This will provide information with regard to any catastrophic failures that may have occurred with respect to the cell or module assembly.

Second, the reason for the initially low current output of the SUNRISE demonstrator must be determined. Subsequently, the decrease in current over the past year should be explained. Effects that contribute to the current produced by a cell include the following:

- The optical transfer function of the concentrating optics.
- The alignment of the various components in the optical train
- The tracking accuracy
- The absorption properties and EQE of the solar cell

To address these potential sources of loss the optical transfer function of the concentrating optics should be measured and compared to the simulated transfer function currently being used in the system model. This should include ellipsometry measurements of the material used for the Fresnel lens and the secondary optic for samples that are fresh off the production line as well as for samples that have been on sun on the SUNRISE demonstrator for the past year. Measurements quantifying the sensitivity of the optical transfer function to misalignments of the primary and secondary optics should also be performed. A study of the effect of tracking error should also be conducted to determine if a sufficient acceptance angle exists when the entire system is on-sun.

A number of improvements should also be made to the system model. The incorporation of the effects of parasitic resistance should be included. This will require calibration of the simulated IV curves to measured IV curves measured at concentrations of 500x or more. Alternatively, the series resistance could also be determined by analyzing the simulated and measured efficiencies as a function of concentration. This is useful because the series resistance causes the efficiency curve to peak when the cell current gets to a certain level. The simulated peak in the efficiency curve should match the measurement and should also be at the same concentration if the series resistance is specified correctly. The two diode model of each subcell should also be revisited. To this point the calibration was done using data measured for isotypes manufactured by a different company than the cells in the SUNRISE demonstrator. The temperature calibration should also be confirmed over a wider range of temperatures and the temperature coefficients for efficiency and open circuit voltage predicted by the system model should be compared to measured values over a range of intensities.

6 Appendix A

A crude calculation of the available solar resource on the earth is possible by treating the sun as a perfect black body as described in Section 0. Table 5 shows all the steps in the calculation of the Steffan-Boltzmann Law calculation of the power from the sun (3.85e26 W) and the resulting average insolation on the earth's surface (342 W/m^2).

Table 5: Black body analysis of the sun and the resulting solar irradiance that reaches the surface of the earth.

Black Body Analysis

The Sun	**Value**	**Units**
Surface Temperature	5780	K
Radius	6.96E+08	m
Surface Area	6.08E+18	m^2
Steffan-Boltzmann Constant	5.67E-08	J/s/m^2/K^4
Emissivity	1.00E+00	
Steffan-Boltzmann Law	3.85E+26	J/s
Power from Sun	3.85E+26	W
Earth		
Average Distance from Sun	1.50E+11	m
Power per unit area at the Earth	**1368**	**W/m^2**
Radius of the Earth	6.37E+06	m
Cross Sectional Area of the Earth	1.28E+14	m^2
Total Insolation on the Earth	1.74E+17	W
	1.74E+05	**TW**
Average Insolation on the Earths Surface	**342**	**W/m^2**
Planks Constant (h)	6.63E-34	Js
Boltzman Constant	1.38E-23	J/K
Speed of Light (c)	3.00E+08	m/s

Figure 6-1 shows the result of plotting the radiation from perfect black bodies with various surface temperatures. The spectrum for a surface temperature of 5780 K is also plotted in Figure 1-12 where it is compared to the AM0 spectrum of the sun.

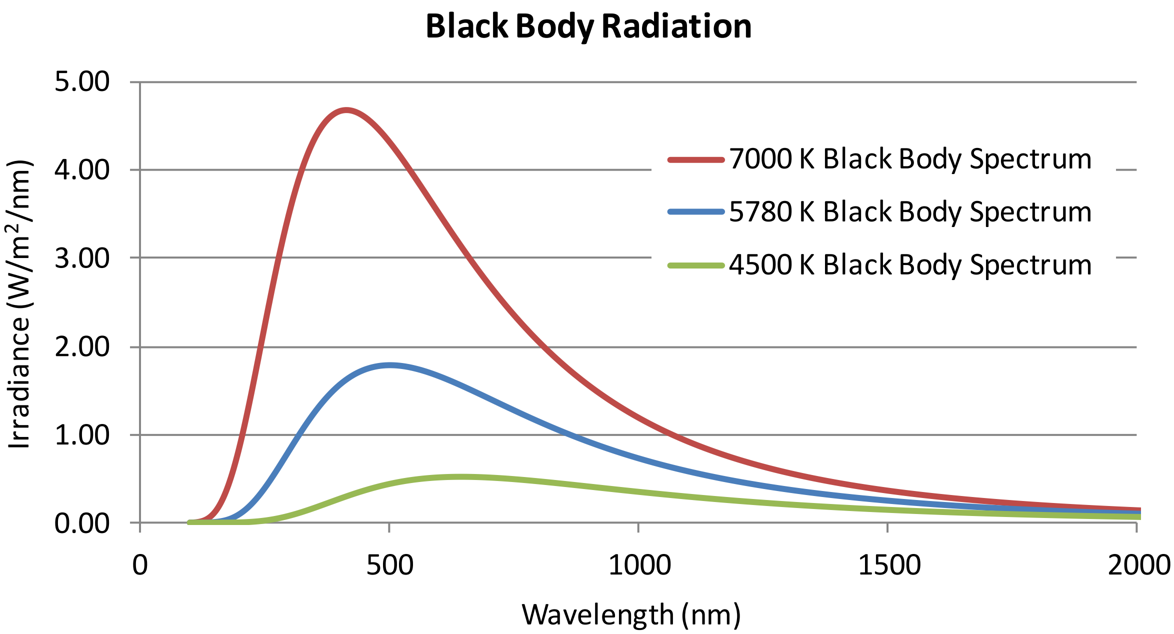

Figure 6-1: Solar Irradiance curves for three different temperatures. The blue curve represents the incident power we would expect to be incident on the earth if the sun was a perfect black body.

7 Appendix B

External quantum efficiency (EQE) is defined as the is the ratio of the number of charge carriers collected by the solar cell to the number of photons of a given wavelength shining on the solar cell from outside (incident photons). An important distinction should be made between the internal quantum efficiency or (IQE) and the EQE just defined. The IQE describes the ratio of the number of charge carriers collected by the solar cell to the number of photons of a given energy that shine on the solar cell from outside *and* are absorbed by the cell.

While the details of external quantum efficiency (EQE) measurements are not the focus of this work, they highlight the necessity for understanding the electrical interaction between subcells and are thus interesting and important to understand.

The EQE of a single junction cell is measured by biasing the solar cell to its short circuit condition and then measuring the current it outputs as the wavelength of incident monochromatic light is varied. The EQE measurement of a triple junction cell is complicated due to the necessity for light biasing of the two subcells that are not being measured.

The bottom subcell is particularly difficult to measure because of its relatively low shunt resistance and poor ideality factor which results in a relatively high slope of its IV curve near the short circuit condition. Figure 7-1 shows the result of biasing error during the measurement of the bottom subcell EQE.

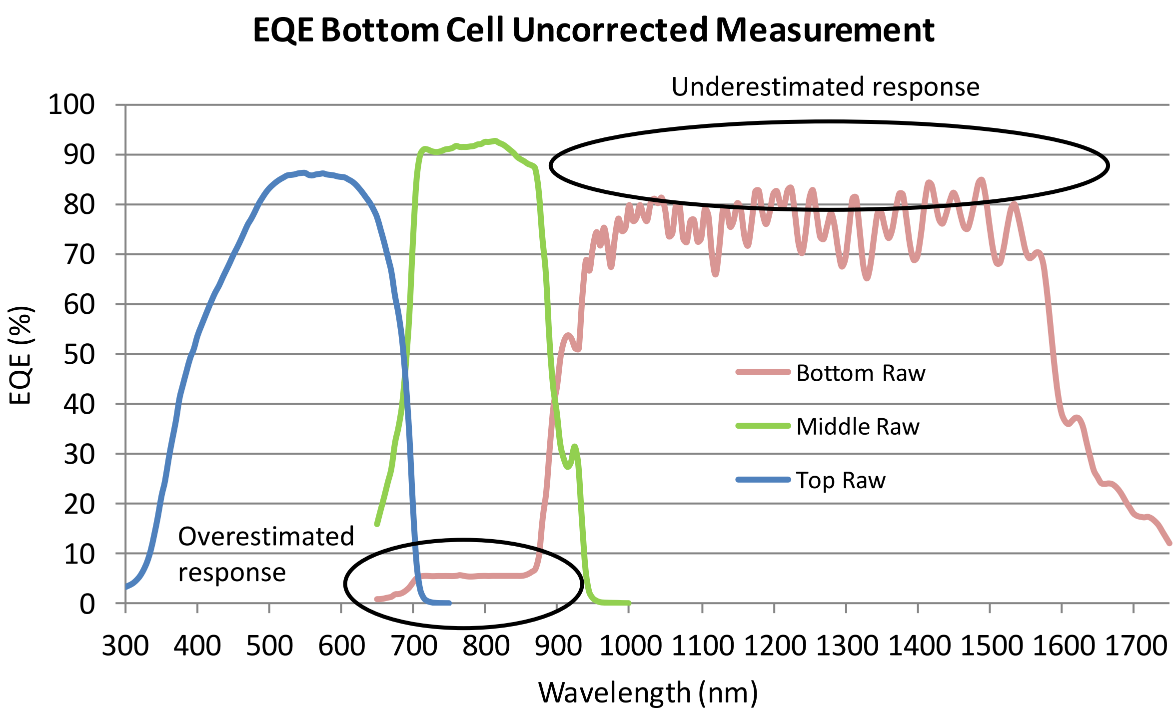

Figure 7-1: EQE measurement of a triple junction solar cell before correction is applied for biasing errors that occur during the measurement of the bottom subcell.

Unfortunately the issue is not easy to avoid if a chopped monochromatic signal is necessary in order to extract the cell response from the noise or background light. To understand the issue we must first understand the normal biasing conditions and then look at how chopping the monochromatic light perturbs this condition.

In order to probe the bottom cell under short circuit conditions when the top two cells are light biased the cell must be forward biased so that the bias points on the three subcell IV curves are A, B, and C as shown in Figure 7-2. If the bias on the triple junction cell was set to zero volts as in the case for a single junction cell then the bias points would be D, E, and F because the subcells are connected in series. Since point D is not the short circuit condition for the bottom subcell this is clearly not the correct biasing condition. When the chopped monochromatic light incident on the cell is at a wavelength that stimulates the bottom cell the bottom cell IV curve shifts up and down with the chopped signal. This variation is represented by the second red IV curve in Figure 7-2.

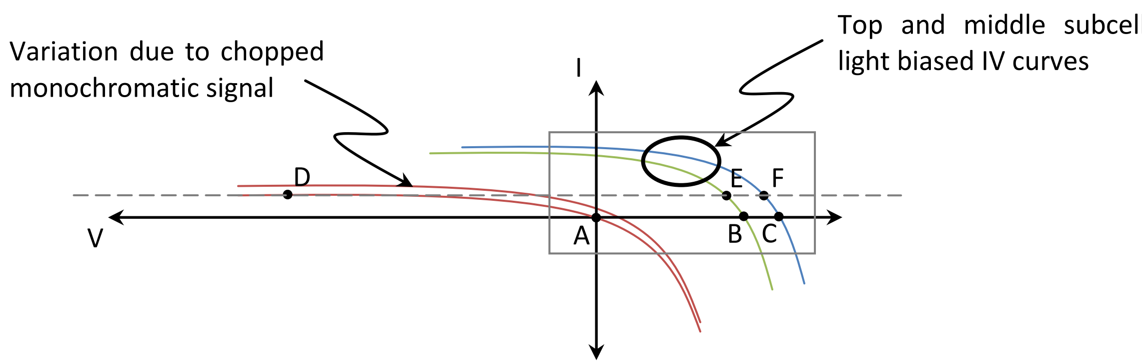

Figure 7-2: Biasing conditions for the EQE measurement of the bottom subcell in a triple junction solar cell. The blue green and red lines are sketches of the top, middle, and bottom IV curves respectively. They are not to scale.

The problem becomes clear if we look at the effect this shift in the bottom subcell IV curve has on the relative biasing of the three subcells. As shown by points A_2, B_2, and C_2 in the magnified view shown in Figure 7-3 the same cell bias no longer achieves the short circuit condition of the bottom subcell. In fact due to the slope of the bottom subcell IV curve near the short circuit condition, there is a measurable underestimation of the short circuit current. Unfortunately, without detailed knowledge of each subcell IV curve the exact bias correction required to measure at the short circuit point (horizontal dashed line) is almost impossible to determine prior to the EQE measurement.

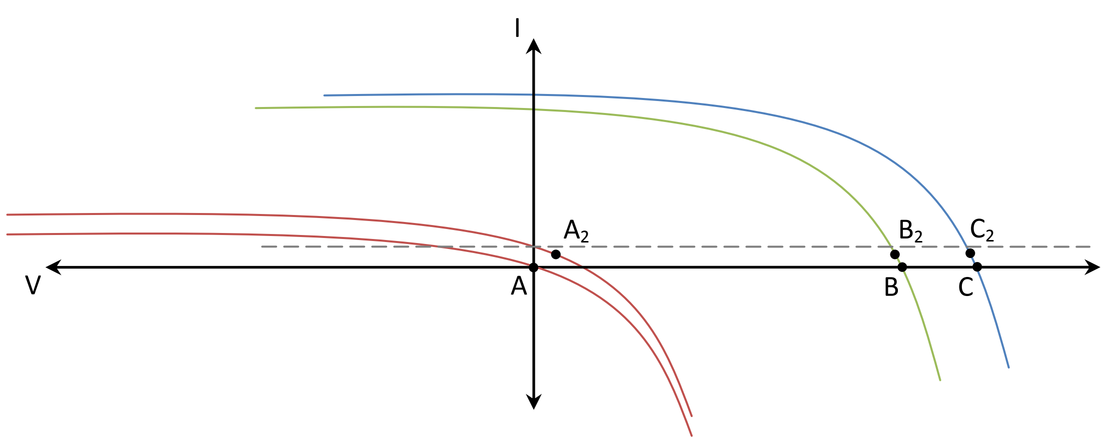

Figure 7-3: Biasing error due to the shifting of the bottom cell IV curve under chopped monochromatic signal.

The same effect occurs when the monochromatic signal reaches a wavelength that the middle cell responds to. In this case however it is the middle subcell IV curve that shifts up and down causing a bias error which results in an artificially inflated response during the measurement of the bottom subcell EQE as is apparent in Figure 7-1.

So what is the solution? Increasing the light biasing of the top and middle subcells will increase the slope of their IV curves at points B and C which will act to mitigate this issue. Note that the steep slope of the top subcell IV curve around point C (not clear in these sketches) means that in general the top subcell does not affect the other subcell EQE measurements significantly in the first place.

A post processing solution is also available and was the strategy used when preparing the EQE measurements for input into the system model presented in Chapter 4 [58]. As described in [58] the overestimation of the bottom subcell response in the middle subcell response region is proportional to the shape of the middle subcell EQE. Thus the middle subcell EQE can be scaled to match the height of the response in the bottom cell EQE and simply subtracted from the bottom subcell EQE. The scaling factor determined in this first part of the correction can then be used to correct for the underestimation in the bottom subcell response region as shown in Figure 7-4 and Figure 7-5.

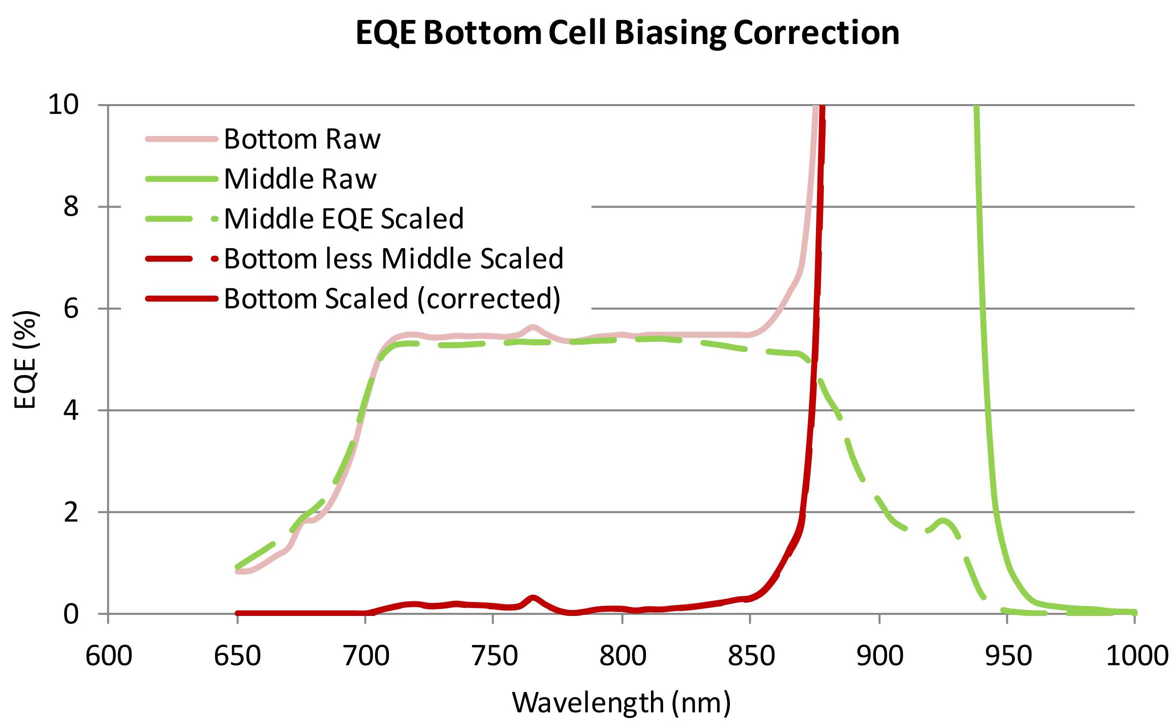

Figure 7-4: Post processing correction of the overestimation of the bottom subcell response in the middle subcell response region.

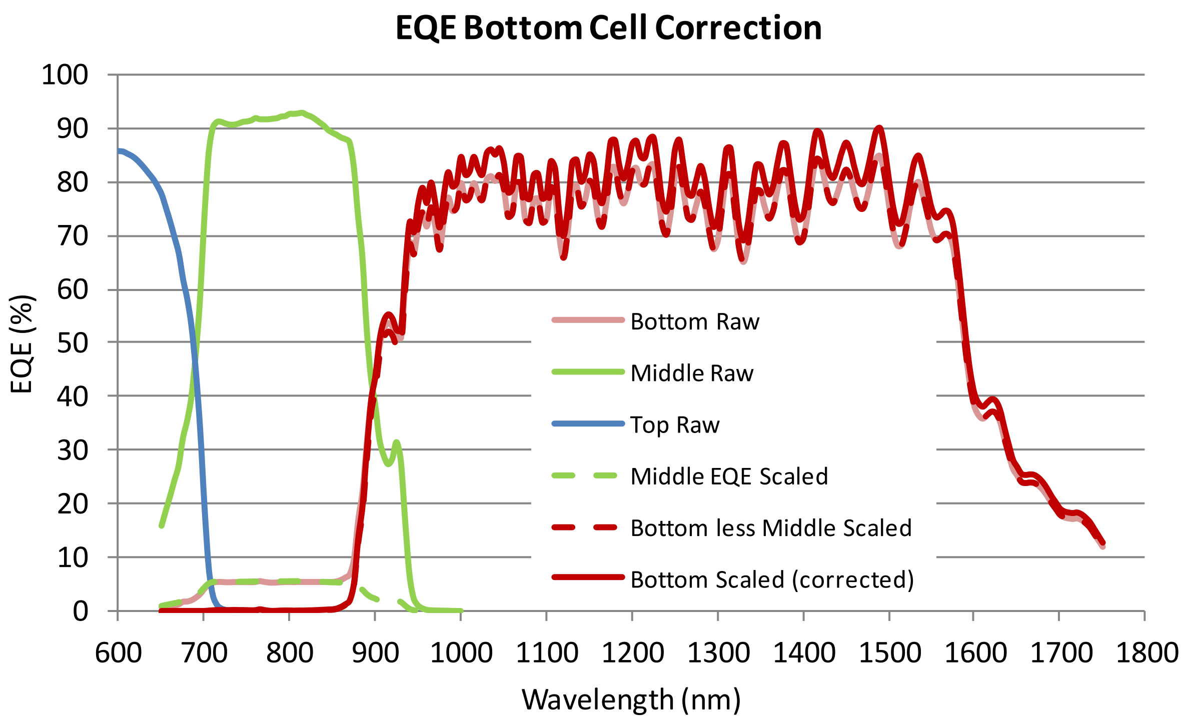

Figure 7-5: Post processing correction of the underestimation of the bottom subcell response in the bottom subcell response region.

8 References

[1] L. Kazmerski, “Best Research Cell Efficiencies,” *National Renewable Energy Laboratory information database*, 2011.

[2] E. Becqurel, “Recherges sur les effets de la radiation chimique de la lumiere solaire au moyen des courants electriques produits sous l’influence des rayons solaires.,” *Comptes Rendus L’Acad Sci*, vol. 9, no. 145-9, pp. 561-7, 1839.

[3] W. Shockley, “The theory of pn junctions in semiconductors and pn junction transistors,” *Bell Syst. Tech. J*, 1949.

[4] W. Shockley, “Holes and electrons in semiconductors,” New York: Van Nostrand, 1950.

[5] J. Chelikowski, “Silicon in all its Forms,” in *Silicon: Evolution and future of a technology*, P. Siffert and E. Krimmel, Eds. Springer Verlag, 2004, p. 1.

[6] T. Markvart and L. Castaner, *Practical handbook of photovoltaics: fundamentals and applications*. Elsevier Science, 2003.

[7] C. A. Wolden, “The Present and Future of Photovoltaic Manufacturing,” *Presentation at University College Dublin*, 2010.

[8] D. Martin, “A Steeper Learning Curve for PV,” 2010. [Online]. Available: http://www.exposolar.org/2011/eng/center/contents.asp?idx=94&page=4&search=&searchstring=&exposolar=C. [Accessed: 09-Sep-2011].

[9] A. Luque and S. Hegedus, *Handbook of photovoltaic science and engineering*. John Wiley & Sons Inc, 2003.

[10] G. Conibeer, “Third-generation photovoltaics,” *Materials Today*, vol. 10, no. 11, pp. 42–50, 2007.

[11] R. R. King, “Raising the Efficiency Ceiling in Multijunction Solar Cells,” in *Quarterly Journal In Modern Foreign Literatures*, 2009, pp. 14-16.

[12] O. D. Miller and E. Yablonovitch, “The Physics Required To Approach The Shockley-Queisser Limit,” in *PVSC35*, pp. 8-10.

[13] P. Hearps, D. Mcconnell, and M. Sandiford, “Renewable Energy Technology Cost Review,” *Melbourne Energy Institute Technical Paper Series*, no. March, 2011.

[14] M. Woodhouse, T. James, R. Margolis, and D. Feldman, “An Economic Analysis of Photovoltaics Versus Traditional Energy Sources: Where Are We Now and Where Might We Be in the Near Future?,” *System*, pp. 2-4, 2011.

[15] A. C. Goodrich, M. Woodhouse, and T. James, “Solar PV Manufacturing Cost Model Group: Installed Solar PV System Prices,” *Energy*. 2011.

[16] N. Monosoff, H. Hardie-hill, and A. Maule, “An Innovative Approach For Determining Pv Cost Convergence In The 25 Solar America Cities,” *Cities*, 2010.

[17] S. O’Rourke, P. Kim, and H. Polavarapu, “Solar photovoltaic industry: looking through the storm,” *Global Markets Research*, no. 2009, 2009.

[18] B. Vanderzwaan and a Rabl, “Prospects for PV: a learning curve analysis,” *Solar Energy*, vol. 74, no. 1, pp. 19-31, Jan. 2003.

[19] European Photovoltaic Industry Association, *Global Market Outlook For Photovoltaics Until 2015*. 2011.

[20] L. Yiyu, “Polysilicon Prices Look Set For Rebound,” *China Daily*, 2011. [Online]. Available: http://www.chinadaily.com.cn/cndy/2011-07/08/content_12859513.htm. [Accessed: 09-Sep-2011].

[21] T. Surek, “Crystal growth and materials research in photovoltaics: progress and challenges,” *Journal of Crystal Growth*, vol. 275, no. 1-2, pp. 292-304, Feb. 2005.

[22] G. Elert, “Chemical Potential Energy,” 2011. [Online]. Available: http://physics.info/energy-chemical/. [Accessed: 09-Aug-2011].

[23] Land Art Generator Initiative, “Total Surface Area Required to Fuel the World With Solar,” *Land Art Generator Initiative*, 2009. [Online]. Available: http://www.landartgenerator.org/blagi/archives/127. [Accessed: 09-Sep-2011].

[24] K. Emery, D. Myers, and S. Kurtz, “What is the appropriate reference spectrum for characterizing concentrator cells?,” *Record of the Twenty-Ninth IEEE Photovoltaics Specialists Conference*, no. May 19 - 24, pp. 840 - 843, 2002.

[25] K. Emery and D. Myers, “Reference Solar Spectral Irradiance: Air Mass 1.5,” 2011. [Online]. Available: http://rredc.nrel.gov/solar/spectra/am1.5/. [Accessed: 10-Sep-2011].

[26] C. Gueymard, “SMARTS2 , A Simple Model of the Atmospheric Radiative Transfer of Sunshine : Algorithms and performance assessment,” *Professional Paper FSEC-PF-270-95. Florida Solar Energy Center*, vol. 1679, 1995.

[27] P. Verlinden and J. Lasich, “Energy rating of Concentrator PV systems using multi-junction III–V solar cells,” in *Photovoltaic Specialists Conference, 2008. PVSC’08. 33rd IEEE*, 2008, pp. 1–6.

[28] H. Mousazadeh, A. Keyhani, A. Javadi, H. Mobli, K. Abrinia, and A. Sharifi, "A review of principle and sun-tracking methods for maximizing solar systems output," *Renewable and Sustainable Energy Reviews*, vol. 13, no. 8, pp. 1800-1818, Oct. 2009.

[29] P. J. Verlinden et al., "Update on two-year performance of 120 kWp concentrator PV systems using multi-junction III–V solar cells and parabolic dish reflective optics," *2008 33rd IEEE Photovolatic Specialists Conference*, pp. 1-6, May. 2008.

[30] SolFocus Inc., "SolFocus Concentrator Photovoltaic (CPV) Systems An Environmentally Balanced Harvest of the Sun," *Energy*. 2010.

[31] SolFocus Inc., "Featured SolFocus Deployments," 2011. [Online]. Available: http://www.solfocus.com/en/installations/. [Accessed: 12-Sep-2011].

[32] Amonix, "Amonix: Powering the Future," 2011. [Online]. Available: http://amonix.com/content/amonix7700. [Accessed: 12-Sep-2011].

[33] G. S. Kinsey, "Building for 25-year Durability in Amonix Solar Power Plants," in *PVMRW*, 2011.

[34] G. S. Kinsey, K. Stone, and J. Brown, "Energy prediction of Amonix CPV solar power plants," *Progress in Photovoltaics: Research and Applications, 25th EU PVSEC WCPEC-5, Valencia, Spain, 2010*, vol. 19, no. 7, pp. 794–796, 2011.

[35] J. Jaus et al., "Development of FLATCON® modules using secondary optics," in *Photovoltaic Specialists Conference (PVSC), 2009 34th IEEE*, 2009, pp. 001931–001936.

[36] P. Mints, "Solar electricity: 2009 surprise success," *Renewable Energy Focus*, vol. 11, no. 3, pp. 42-47, May. 2010.

[37] Emcore, "Utility-Scale Concentrator Photovoltaic (CPV) System," 2011. [Online]. Available: http://www.emcore.com/assets/photovoltaics/Gen III_2011.pdf. [Accessed: 13-Sep-2011].

[38] J. Foresi, L. Yang, and P. Blumenfeld, "EMCORE receivers for CPV system development," *Photovoltaic Specialists Conference (PVSC), 2010 35th IEEE*, pp. 209-212, 2010.

[39] Daido Steel, "Technology of Daido Steel," 2011. [Online]. Available: http://www.daido.co.jp/en/products/cpv/technology.html. [Accessed: 12-Sep-2011].

[40] Emcore, "G3-1090X Concentrator Photovoltaic Module," 2011. [Online]. Available: http://www.emcore.com/assets/photovoltaics/G31090X Module_2011.pdf. [Accessed: 13-Sep-2011].

[41] O. Arenas, L. Collin, and S. Chow, “Comparative thermal analysis of solar cells mounted on ceramic and metallic carriers and their optimization for CPV applications,” *(PVSC), 2010 35th*, pp. 2998-3002, 2010.

[42] C. E. Valdivia et al., “Measurement of high efficiency 1 cm2 AlGaInP/InGaAs/Ge solar cells with embedded InAs quantum dots at up to 1000 suns continuous concentration,” in *Photovoltaic Specialists Conference (PVSC), 2010 35th IEEE*, pp. 001253–001258.

[43] S. Chow, “Integration of High Efficiency Solar Cells on Carriers for Concentrating System Applications,” University of Ottawa, 2011.

[44] S. M. Sze and K. K. Ng, *Physics of semiconductor devices*. Wiley-Blackwell, 2007.

[45] C. Honsberg and S. Bowden, “PVCDROM,” 2010. [Online]. Available: http://pveducation.org/pvcdrom. [Accessed: 13-Sep-2011].

[46] J. Nelson, “The physics of solar cells,” Imperial College Press London, 2003.

[47] T. Kirchartz, “Generalized detailed balance theory of solar cells,” Forschungszentrum, 2009.

[48] A. Walker, “Calculations of material parameters including diffusion length performed for various recombination models.” 2011.

[49] W. Shockley and H. J. Queisser, “Detailed Balance Limit of Efficiency of p-n Junction Solar Cells,” *Journal of Applied Physics*, vol. 32, no. 3, p. 510, 1961.

[50] B. Streetman, “Solid state electronic devices,” 1990.

[51] Y. Varshni, “Temperature dependence of the energy gap in semiconductors,” *Physica*, vol. 92, no. 19, p. 196403, May. 1967.

[52] A. W. Walker, J. F. Wheeldon, O. Thériault, M. D. Yandt, and K. Hinzer, “Temperature Dependent External Quantum Efficiency Simulations and Experimental Measurement of Lattice Matched Quantum Dot Enhanced Multi-Junction Solar Cells,” in *Photovoltaic Specialists Conference (PVSC), 2011 37th IEEE*, 2011, no. 25.

[53] M. Yandt, A. Johnson, C. Valdivia, and K. Hinzer, “Remote Data Acquisition System for the SUNRISE Solar Demonstrator,” in *TEXPO*, 2010.

[54] J. D. Haigh, A. R. Winning, R. Toumi, and J. W. Harder, “An influence of solar spectral variations on radiative forcing of climate.,” *Nature*, vol. 467, no. 7316, pp. 696-9, Oct. 2010.

[55] O. Thériault et al., “Temperature-Dependent Quantum Efficiency of Quantum Dot Enhanced Multi-Junction Solar Cells,” *System*, vol. 34, no. 2009, pp. 1-4, 2011.

[56] S. Adachi, “Handbook on physical properties of semiconductors,” vol. 2, 2004.

[57] Y. Sakurada, Y. Ota, and K. Nishioka, “Simulation of Temperature Characteristics of InGaP/InGaAs/Ge Triple-Junction Solar Cell under Concentrated Light,” *Japanese Journal of Applied Physics*, vol. 50, no. 4, p. 04DP13, Apr. 2011.

[58] G. Siefer, C. Baur, and A. W. Bett, “External quantum efficiency measurements of Germanium bottom subcells: Measurement artifacts and correction procedures,” in *Photovoltaic Specialists Conference (PVSC), 2010 35th IEEE*, 2010, pp. 000704–000707.